

# Optical performance and drilling forces of an orthopaedic DRS drill with a stagnant optical probe

A thesis submitted in fulfilment of the requirements for a degree in Master of Science in Biomedical Engineering at the Delft University of Technology

By M. P. Kan

4141822

Medical Instruments and Medical Safety

Supervisors:

Prof. Dr. B.H.W. Hendriks

Prof. Dr. J. Dankelman

PhD Candidate MSc. A. Swamy

Delft University of Technology/ Philips Research

Delft University of Technology

Delft University of Technology/ Philips Research

*Figure 1.* Cover photo: Stefan Irvine/LightRocket via Getty Images [1]



“It will reward enough for me if, by the publication of the present experiment, I have directed the attention of investigators to this subject, which still promises much for physical optics and appears to open a new field.”

— *Joseph Von Fraunhofer, (1787 – 1826)*



Thanks to:

My Parents, Prof. dr. Benno Hendriks, Prof. dr. Jenny Dankelman, Akash Swamy MSc., Sara Azizian Amiri MSc., Merle Losch MSc., Prof. dr. Jan Verhaar, Prof. dr. Maarten van der Elst, Drs. Agnita Stadhouder, Dr. Joost Rutges, Erna ten Hove, Bert Bakker, Philine Luik, Dieuwertje Drexhage, Floris van Drunen and the thousands of people that made my education and student life possible, from lecturers to cleaning personnel and all the dear friends I had the pleasure of spending my time in Delft with.

# Abstract

**Introduction.** In spinal surgery, the misplacement of spinal screws is a problem that causes (severe) pain, bleedings or even paralysis [2]. Screw misplacements are common as navigating in the spine is difficult due to the small vertebral dimensions and a lack of anatomical landmarks [3] [4]. In order to improve the navigational support of spine surgeons, this research focuses on the development of an optical sensing diffuse reflectance spectroscopy (DRS) surgical drill that identifies bone tissue boundaries. The developed drill concept introduces a stagnant optical fiber-equipped probe into a cannulated orthopaedic drill. To verify the clinical applicability of the developed system, the accuracy of the optical tissue boundary detection has been analysed under different tissue penetration speeds, as well as the axial drilling force increases due to the introduction of a stagnant probe into a drill.

**Results.** When increasing the drilling feed rate in the optical phantom, the drill overshoot (the difference between the DRS-derived tissue boundary location identification and the actual location of the phantom boundary) shows a larger spread. The maximum feed rate at which no overshoot takes place is 0,5mm/s. Increasing the sampling frequency –especially decreasing the inactive period between the measurements– can improve this.

None of the K-wire equipped drills can penetrate the used Sawbones® cortical bone phantom. The axial peak feed forces occurring in the Sawbones® cancellous bone phantom while using a regular 2,7mmØ orthopaedic drill is 38,2N. When using the 2,7mmØ orthopaedic drill with a 1,6mmØ K-wire, a peak of 57,6N is observed. Because the data from drilling in the Sawbones® cancellous bone is not normally distributed, a benchmark experiment on cheese is analysed. On average, the introduction of a K-wire increases the required drilling forces by a 296% (roughly a factor 3). Among the different feed rates and drill types, the force increase of introducing a stagnant K-wire varies between 16% and 575%.

**Conclusion.** To prevent orthopaedic screws from breaching the bone surface (an overshoot of 0mm) in spinal surgery, the established feed rate speed limit of 0,5mm/s is too low. To meet the observed feed rates applied by surgeons of up to 5mm/s, it is of interest to reduce the DRS sampling time – the inactive period between two measurements in particular. The feed force increase of approximately a factor 3 can be regarded as a challenge for surgeons, who indicated that they preferred feed forces to be kept low. Further testing on real (cadaveric) vertebrae can more give information about the DRS drill's optical performance in pedicles, and whether the identified feed force increase proves to be problematic for clinical applications.



# Content

Abstract

Content

.....	0
List of figures .....	2
List of tables.....	3
List of equations .....	3
List of abbreviations.....	3
<b>1. Introduction.....</b>	<b>4</b>
1.1. Spinal Screw Placement (SSP) .....	7
1.1.1. Vertebral dimensions .....	10
1.1.2. Thermal osteonecrosis.....	13
1.2. Diffuse Reflectance Spectroscopy (DRS) .....	16
1.2.1. DRS Principles.....	16
1.2.2. DRS-based fat fraction in bone.....	17
1.2.3. State of the art.....	17
1.3. DRS drill concepts .....	19
1.3.1. Fiber integration and connection.....	19
1.3.2. Concept selection.....	20
1.4. Research questions and hypotheses.....	22
1.4.1. Feed rate speed limit .....	22
1.4.2. Axial forces.....	23
<b>2. Methods .....</b>	<b>25</b>
2.1. Experiments .....	27
2.1.1. Optical experiment.....	27
2.1.2. Mechanical experiment .....	28
2.2. Drilling setup.....	29
2.2.1. Mount.....	29
2.2.2. Stepper motor.....	30
2.2.3. Linear stage and load cell .....	31
2.2.4. Drilling parts .....	31
2.2.5. DRS equipment.....	32
2.2.6. Electrical circuit.....	35
2.3. Bone phantom tissue .....	36
2.3.1. Optical bone phantom.....	36
2.3.2. Mechanical bone phantom .....	37
2.3.3. Benchmark phantom.....	37
2.4. Statistical analyses.....	38
2.4.1. Optical data processing.....	38
2.4.2. Mechanical data processing.....	38
<b>3. Results.....</b>	<b>39</b>
3.1. Optical experiment.....	40
3.1.1. Sampling frequency .....	41
3.1.2. Individual spectra .....	42
3.1.3. Tissue boundary detection.....	43
3.2. Mechanical experiment.....	46
3.2.1. Axial drilling forces .....	46

3.2.2.	Rotational speed.....	52
<b>4.</b>	<b>Discussion .....</b>	<b>53</b>
4.1.	DRS drill performance .....	54
4.1.1.	Optical bone phantom .....	55
4.1.2.	Mechanical bone phantom .....	57
4.2.	Optical measurement improvements .....	59
4.2.1.	Sampling time .....	59
4.2.2.	Signal intensity .....	60
4.2.3.	More measurements .....	61
4.3.	Follow up research .....	62
4.3.1.	Drilling at an angle .....	62
4.3.2.	Cadaveric testing.....	62
4.3.3.	Clinical trials .....	62
4.4.	DRS drill concept development.....	63
4.4.1.	DRS drilling probe .....	63
4.4.2.	One fiber.....	64
4.4.3.	Directional feedback.....	64
4.5.	Applicability of a DRS drill.....	65
4.5.1.	DRS drill users.....	65
4.5.2.	Thermal osteonecrosis.....	66
4.5.3.	Osteoporosis .....	66
4.5.4.	User interaction design .....	66
<b>5.</b>	<b>Conclusions .....</b>	<b>67</b>
5.1.	Optical experiment .....	69
5.1.1.	Feed rate speed limit .....	69
5.2.	Mechanical experiment.....	70
5.2.1.	Axial drilling force increases.....	70
<b>6.</b>	<b>References .....</b>	<b>71</b>
<b>7.</b>	<b>Appendix.....</b>	<b>78</b>
7.1.1.	Visited surgery notes.....	79
7.2.1.	Optical drilling setup .....	81
7.2.2.1.	Technical drawings mount components.....	82
7.2.2.2.	Stepper motor specifications, torque curve and Arduino® script .....	84
7.2.2.3.	Aerotech PRO115SL and FUTEK load cell specifications and dimensions .....	86
7.2.2.4.	Drilling parts.....	91
7.2.3.	Bone phantom tissue.....	93
7.3.1.	Optical measurement plots .....	95
7.3.2.	Mechanical measurement cheese.....	97

# List of figures

Figure 1. Cover photo: Stefan Irvine/LightRocket via Getty Images [1]	1
Figure 2. Surgical fusion of the spine (the L1 vertebra and the sacrum) [10]	5
Figure 3. Vertebrae with a well-placed (left) and a misplaced (right) pedicle screw [15]	7
Figure 4. A cannulated orthopaedic drill bit (left) and a K-wire (right) [17] [18]	9
Figure 5. An Orthopaedic drill by OrthoProMed [20]	9
Figure 6. Boxplots of the Pedicle Outer Width (POW) of the cervical vertebrae	10
Figure 7. Radiographs of the left and right cervical pedicle in the coronal plane [35]	12
Figure 8. Cortical thickness (COT) in the pedicles of the cervical vertebrae C3–C7 [22]	12
Figure 9. Schematic view of bone drilling with heat development in marked areas '1' and '2'	13
Figure 10. DRS scattering and absorption	16
Figure 11. Light distribution and the LAD of DRS	16
Figure 12. DRS drill concepts: rotating fibers (left) and a stagnant fiber-equipped probe (right)	19
Figure 13. A rotating DRS fiber-equipped drill developed by Duperron <i>et al.</i> [35]	20
Figure 14. Picture of the (optical) experimental setup used in this research	27
Figure 15. Schematic view of the experimental setup used in this research	27
Figure 16. The DRS-drilling unit	29
Figure 17. Drill bits used	31
Figure 18. The tip of the optical fiber-equipped probe (left) and a trocar-tip K-wire (right)	32
Figure 19. A spectrum of gelatin lipid phantom tissue	34
Figure 20. The measurement components and electrical circuit of the drill	35
Figure 21. Bone phantom tissue boundary drilling deformity reduction	36
Figure 22. A Sawbones® 15 PCF cellular foam block with a thickness of 40mm	37
Figure 23. Spectra of lipid bone phantom (left) and the agar bone phantom (right)	42
Figure 24. A spectrum of agar phantom resulting in an inaccurate fat fraction identification	43
Figure 25. Fat fractions versus location at a 0,5mm/s feed rate	44
Figure 26. Fat fractions versus location at feed rates of 0,5mm/s and 2,5mm/s	44
Figure 27. Scatterplot of the feed rate and overshoot of the DRS drilling setup	45
Figure 28. Axial drilling forces of a 2,7mmØ orthopaedic drill in Sawbones® phantom, 2mm/s	46
Figure 29. The physical structure of the mechanical Sawbones® phantom	47
Figure 30. Single and average force measurements of a 2,7mmØ drill in Sawbones® at 2mm/s	47
Figure 31. Average force measurements of a 2,7mmØ drill in Sawbones® at varying feed rates	48
Figure 32. Average axial drilling forces of three drill types in Sawbones® phantom at 2mm/s	48
Figure 33. Histograms of axial forces in Sawbones® cellular foam phantom at 2mm/s	50
Figure 34. Histograms of axial forces in cheese at 2mm/s	50
Figure 35. Boxplot of axial forces on varying drill types in cheese	51
Figure 36. Spectra and fit functions with (left) and without (right) taking collagen into account	56
Figure 37. The preservation of etendue in a perfect optical system	60
Figure 38. Approaching a cortical bone boundary at angle $\alpha$ in a pedicle	62
Figure 39. Probe tip variables and a cross section of a possible probe design	63
Figure 40. The one-fiber (left) and the directional feedback (right) DRS drill concepts	64
Figure 41. A fluoroscopic image of a jaw with the alveolar nerve marked in red [85]	65

## List of tables

Table 1. An overview of studies reporting cortical breaches by pedicle screws [3].....	8
Table 2. Sampling frequencies under varying integration times.....	41
Table 3. Sampling distances under varying feed rate.....	41
Table 4. Drilling overshoots at varying feed rates.....	45
Table 5. Axial forces of different drills and feed rates in Sawbones® foam phantom.....	49
Table 6. Axial forces of different drills and feed rates in cheese.....	51
Table 7. ANCOVA tests of between subject effects.....	51

## List of equations

Equation 1. Heat production during drilling.....	13
Equation 2. The behaviour of light in tissue.....	16
Equation 3. The fat fraction change per second, causing a wavelength ratio drop in a.u./s.....	18
Equation 4. Hypothetical drilling overshoot determination.....	22
Equation 5. Axial force estimation in bone drilling.....	23
Equation 6. The bone-machining surface ratio.....	24
Equation 7. DRS sampling frequency determination.....	33
Equation 8. The water- and lipid-based absorption coefficient.....	34

## List of abbreviations

a.u.	arbitrary units
DRS	Diffuse Reflectance Spectroscopy
IHME	Institute for Health Metrics and Evaluation
K-wire	Kirschner wire
LAD	Look Ahead Distance
NIR	Near-InfraRed (wavelength region)
OR	Operation Room
PIW	Pedicle Inner (cortical) Width
POW	Pedicle Outer Width
SD	Standard Deviation
SFS	Spinal Fusion Surgery
SNR	Signal to Noise Ratio
SSP	Spinal Screw Placement
VIS	Visible (wavelength region)
YLDs	Years Lived with Disability

# 1. Introduction

Spine surgeries are common surgical procedures, used to relieve some of the most pressing physical health issues today [5]. Recent publications however, argue that overall, there is insufficient evidence that spinal fusion surgery improves patient outcomes [7] [9].

This can be changed if surgical equipment offers better support to surgeons to minimize medical complications. In spine surgery, a sensing surgical drill provides an opportunity to mitigate screw misplacement rates. This would prevent pain, damage to vital structures and –in severe cases– paralysis and arterial bleedings.

Orthopaedic drills are commonly used surgical instruments for placing bone screws, implants, Kirschner-wires (K-wires), rods and plates onto bones. Surgeries that include these handlings are used to restrain some of the most pressing physical health issues today. Low back pain for instance, has been the worldwide leading cause of disability for the past 30 years according to the Institute for Health Metrics and Evaluation (IHME) [5]. Between 1990 and 2015, years lived with disability (YLDs) caused by low back pain increased by 54%, and this growth is not expected to halt in the coming decades [6]. According to *The Economist*, there were approximately 85.000 spinal fusion surgeries in the USA in 2015 [7].

The purpose of surgical treatments in this field, is to eliminate pain by decompressing the spine –either by removing superfluous bone tissue or by eliminating relative movement of the vertebrae shown in *Fig. 2* [8].

Yet, the pain mechanism of the human nervous system is more complex than this theoretical concept with a surgical ‘on/off switch’. Recent publications in academical and mainstream media such as *The Lancet* and *The Economist* argue that overall, there is insufficient evidence that spinal fusion surgery (SFS) improves patient outcomes [7] [9]. In a 2011 follow-up study, the American insurance company Cigna found that after two years, 87% of their customers who had undergone spinal fusion surgery were still in pain that required medical treatment and 15% required even more surgery [7].

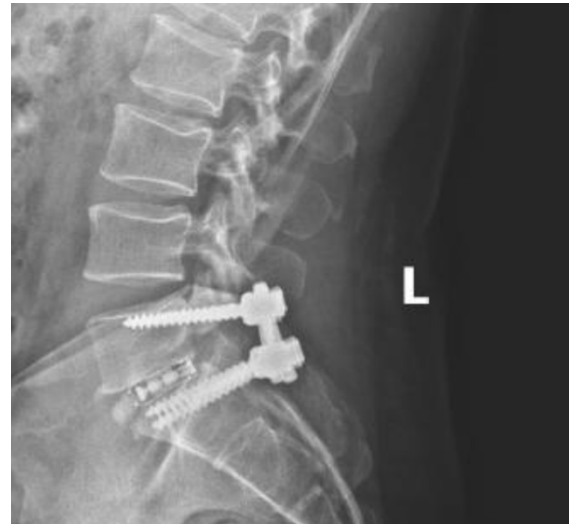


Figure 2. Surgical fusion of the spine (the L1 vertebra and the sacrum) [10]

Apart from the poor patient outcomes, this status quo imposes a heavy financial burden on health care systems. The costs of a back surgery vary from \$25.000 to \$100.000 [7]. These are expenses that should to be justified by the improvement of people’s lives, instead of leading to more pain and surgery. Researchers suggest to resect this systemic health care redundancy in two ways [9]:

1. Reduce the amount of spine surgeries by applying a stricter selection of patients, including only those who are likely to benefit from the procedure.
2. Reduce the risk of medical complications within the field of spine surgery.

This thesis will focus on the latter. Developing an optical sensing surgical drill could help a surgeon navigate in the spine and mitigate the risk of spinal screw misplacements. This way, these medical errors that can cause damage to vital structures and pain to patients could be restrained.

This chapter will briefly discuss challenges encountered during spinal surgery, a suggested solution for these issues –a sensing surgical drill– and the research questions that verify the current potential of this concept.

In Section 1.1., two challenges causing collateral damage in spinal surgery are identified: screw misplacement and thermal osteonecrosis. Thermal osteonecrosis can be reduced through measures that limit drilling heat development. Screw misplacements can potentially be mitigated through improved navigational support. The Section concludes with examples of orthopaedic drilling instruments, to provide a context of currently used equipment.

Section 1.2. briefly elaborates the principles of the optical tissue identification technique upon which the navigational support in this research relies, as well as the state of the art in its application to bone drilling.

Section 1.3. discusses design concepts to integrate optical fibers into a surgical drill are introduced, as well as the criteria on which one of these concepts is selected for this research.

The chapter finishes with the research questions and hypotheses around which this research evolves in Section 1.4.

## 1.1. Spinal Screw Placement (SSP)

### Screw placement principles

A wide variety of bone conditions require the placement of screws, pins and grafts to stabilize fractures, correct deformities, or to fixate bones [8]. Examples are unstable fractures through sudden impact, scoliosis, and back problems such as spinal disc herniation.

Posterior pedicle screw placement, shown in *Fig. 3*, is a popular surgical technique due to its superior pull-out strength and anatomical accessibility [11]. In this procedure, a screw is driven through the pedicle(s). The pedicle is the narrow pathway between the vertebral body and the vertebral processes. The vertebral foramen –through which the spinal cord passes– can be found in the centre, on the medial side of the pedicles. The vertebral arch consists of two pedicles and two laminae. Together with the body, the arch encloses the vertebral foramen.

Screw placement throughout the whole human body –from dental applications to long bones and irregular bones– commonly requires pilot hole drilling, pre-drilling, or vertebral cannulation by a handheld awl [12] [13]. During this phase

of surgery, accurate navigation is key to prevent potentially harmful screw misplacements.

### Challenges

Screw misplacements –in which the screw breaches the bone surface– cause serious risks during spinal screw placement (SSP). A 2018 study by Woo and DiCuccio showed that in 31 studies on pedicle screws, misplacement rates varied from 2% to 50% [3]. Their findings are summarized in *Table 1*. Although definitions vary, it can be concluded that it is challenging to accurately navigate during spine surgery, while risks include pain, bleedings or even paralysis [2].

These misplacement rates are not surprising. Vertebral bone drilling is considered difficult; it can be technically demanding and it carries considerable physical risks. In the spine –particularly in the cervical (neck) area–, drilling is technically demanding due to small pedicle dimensions, a lack of anatomical landmarks, and the transverse angle under which screws need to be placed [4]. Furthermore, it inherits high risks due to the relatively close presence of the spinal cord and vertebral artery [14].

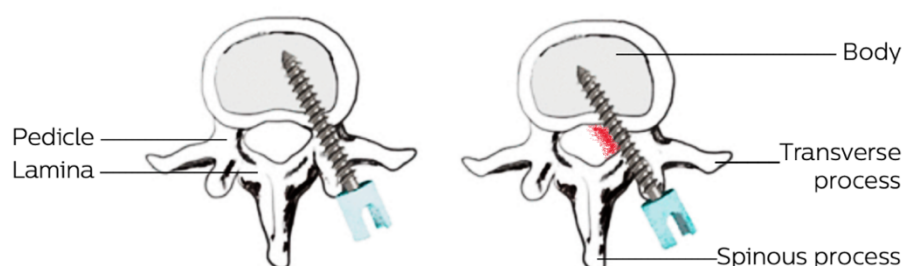


Figure 3. Vertebrae with a well-placed (left) and a misplaced (right) pedicle screw [15]



Authors	Definition or grading system of mediolateral breach	Pedicule screws			Patients		
		Total N	Breach n	% n/N	Total N	Breach n	% n/N
Schizas et al. [2]	Any encroachment; mediolateral and craniocaudal* breach: breach<3 mm; 3 mm≤breach≤6 mm; breach>6 mm	60	<sup>†</sup> 18	30%	15	12	80%
Su et al. [3]	Any breach>0, as measured in increments of 0.1 mm (100 μm)	338	33	10%	20	11	55%
Wiesner et al. [4]	Mediolateral breach: 0, 1, 2, 3, 4, 5, 7, or 8 mm; any craniocaudal breach*	408	27	7%	51	23	45%
Ringel et al. [5]	<2 mm acceptable; 2 mm≤breach<4 mm; 4 mm≤breach<6 mm; breach≥6 mm	298	33	11%	30	<sup>‡</sup> 13	43%
Amiot et al. [6]	Breach: 0.1–2 mm; 2.1–4 mm; 4.1–6 mm; >6 mm	828	99	12%	150	62	41%
Raley and Mobbs [7]	Breach≤2 mm; breach>2 mm and/or presence of complications	424	41	10%	88	29	33%
Wu et al. [8]	Medial: ≤2 mm acceptable; breach >2 mm; lateral: ≤4 mm acceptable; breach >4 mm; any anterior breach*	677	70	10%	62	20	32%
Amato et al. [9]	Any encroachment; breach 0–2 mm; 2.1–4 mm; >4 mm	424	33	8%	102	27	26%
Laine et al. [10]	Breach: 0–2 mm <sup>‡</sup> ; 2–4 mm; 4–6 mm	496	47	9%	91	<sup>‡</sup> 21	23%
Smith et al. [11]	Breach: 0–2 mm <sup>‡</sup> ; ≥3 mm	601	37	6%	151	31	21%
Gertzbein and Robbins [12]	Medial breach: 0–2 mm; 2.1–4 mm; 4.1–6 mm; 6.1–8 mm; lateral breach: boundaries not reported	167	47	28%	40	<sup>‡</sup> 8	20%
Koktekir et al. [13]	≤25% screw diameter acceptable; breach>25% of screw diameter out of pedicle	1218	27	2%	198	21	11%
Parker et al. [14]	≤25% screw diameter acceptable; breach>25% of screw diameter out of pedicle	6816	115	2%	964	87	9%
Castro et al. [15]	Mediolateral breach: 0–2 mm <sup>‡</sup> ; 2–4 mm; 4–6 mm; 6–8 mm; any anterior breach*	123	61	50%	30	Not reported	
John [16]	Breach: 0.1–2 mm; 2.1–4 mm; 4.1–6 mm; >6 mm	80	26	33%	20	Not reported	
Waschke et al. [17]	Breach: 0<breach<2 mm; 2 mm≤breach<4 mm; ≥4 mm	4424	1147	26%	1006	Not reported	
Merc et al. [18]	Breach<2 mm and <half screw diameter <sup>‡</sup> ; 2 mm<breach<4 mm <i>or</i> breach<screw diameter; breach>4 mm <i>or</i> whole screw out	108	27	25%	19	Not reported	
Nevzati et al. [19]	Breach: 0.1–2 mm; 2.1–4 mm; >4 mm	1236	247	20%	273	Not reported	
Kulik et al. [20]	Breach: <2 mm; ≥2 mm	204	40	20%	30	Not reported	
Ringstrom et al. [21]	Mediolateral breach: <2 mm; 2–3.99 mm; ≥4 mm; any anterior breach*	116	22	19%	25	Not reported	
Halm et al. [22]	Medial breach: <2 mm; ≥2 mm Lateral breach: <3 mm; ≥3 mm	104	19	18%	12	Not reported	
Fu et al. [23]	Breach<2 mm <sup>‡</sup> ; breach>2 mm	66	8	12%	12	Not reported	
Bai et al. [24]	Mediolateral: breach<2 mm; 2 mm≤breach≤4 mm; breach>4 mm; any anterior breach*	694	62	9%	42	Not reported	
Merloz et al. [25]	Breach: >1 mm medial, lateral, or caudal*	278	25	9%	52	Not reported	
Pithwa and Venkatesh [26]	Breach: 0–2 mm <sup>‡</sup> ; 2–4 mm; >4 mm	300	20	7%	59	Not reported	
Kim et al. [27]	Breach<2 mm; 2 mm≤breach<4 mm; 4 mm≤breach<6 mm; breach≥6 mm	160	11	7%	40	Not reported	
Lonstein et al. [28]	Breach not quantified; CT ordered only if patient had signs/symptoms; analysis included medial, lateral, anterior*, superior, and inferior breach	4790	242	5%	875	Not reported	
Yang et al. [29]	Breach<2 mm; 2 mm≤breach≤4 mm	<sup>‡</sup> 362	17	5%	<sup>‡</sup> 76	Not reported	
Zhang et al. [30]	Breach<2 mm; 2 mm≤breach≤4 mm; breach>4 mm	294	16	5%	66	Not reported	
Chaput et al. [31]	<2 mm acceptable; breach≥2 mm	78	2	3%	18	Not reported	
Van de Kelft et al. [32]	Medial: any breach; lateral: ≤half screw diameter acceptable; breach>half screw diameter	1881	47	2%	353	Not reported	

CT, computerized tomography.

\* Anterior breach (ie, screw tips encroaching upon or violating the presacral space) or craniocaudal malposition was also reported.

<sup>†</sup> Coronal studies revealed nine mediolateral perforations and nine craniocaudal breaches. Axial images revealed 14 mediolateral perforations.

<sup>‡</sup> Ringel et al. randomized 30 patients to robot-assisted screw placement and 30 to freehand technique. In the robot-assisted group, 13 patients had at least one screw with breach≥2 mm. For the freehand group, the number of patients with breach was not reported.

<sup>§</sup> The categories of cortical breach were ambiguous. For example, in the presence of overlapping values (eg, 0–2 and 2–4 mm) or values that were omitted (eg, <2 or >2 mm), one cannot distinguish which category was assigned for a breach of exactly 2 mm.

<sup>||</sup> The reported numbers of affected patients were limited to those patients with inferior or medial cortical breach.

<sup>¶</sup> The study only reported the number of patients affected by a breach≥4.1 mm.

<sup>‡</sup> Postoperative CT scans were available in only 75 patients (354 screws).

Table 1. An overview of studies reporting cortical breaches by pedicle screws [3]

(The references in this table do not correspond with the bibliography of this research)

## Drilling equipment

Examples of currently used orthopaedic drilling instruments are shown in *Fig. 4* and *Fig 5*. The drill in *Fig. 5* is an orthopaedic drill by OrthoProMed with a regular orthopaedic drill bit. Key differences between orthopaedic drills and regular drills include sterility, cannulation, and a dual trigger.

As surgical drills are used in the operation room (OR), they need to be sterilizable; the smooth surfaced components can be taken apart for sterilization. Furthermore, they feature no air vents that could possibly exchange biohazardous substances such as debris or pieces of drill components.

Orthopaedic drills feature a hollow channel along the axis of the drill bit, in order to use K-wires, which are steel pins shown in *Fig. 4*. As a K-wire can be up to 600mm in length, the cannulated drill can be placed over it in order to improve the surgeon's ability to aim the K-wire.



*Figure 4.* A cannulated orthopaedic drill bit (left) and a K-wire (right) [17] [18]

In some cases, cannulated orthopaedic screws are placed over K-wires that serve as a directional guide [19]. A cannulated drill tip, shown in *Fig. 5*, which rotates around the K-wire, can be used to drill the trajectory for the cannulated screw.

Lastly, dual trigger systems are often seen on orthopaedic drills. The separate triggers feature the different drilling rotation directions: one for tissue penetration and one for pulling the drill back.



*Figure 4.* An Orthopaedic drill by OrthoProMed [20]



Based on POW, the C3, C4 and C5 vertebrae are most challenging to perform SSP on. The dotted line at 4,5mm indicates the minimal POW suited for safe 3,5mm SSP, according to Westermann *et al.* [22]. 87% of the POW means are above this 4,5mm threshold, indicating that the vast majority of patients is eligible for cervical SSP.

### 3,5mm screw accommodation

The 3,5mm spinal screw is most often mentioned in studies on cervical SSP [28] [29] [30] [31] [32]. During the writing of this thesis, two surgeries were visited in which a total of 33 orthopaedic screws were placed; all of which were 3,5mm screws as well. Notes of the visited surgeries and the conversations with surgeons can be found in Appendix 7.1.1.

Three of the 59 studies on vertebral dimensions –retrieved for the literature research conducted prior to the writing of this thesis– specifically commented on screw accommodation [22] [33] [34]. All of these studies focused on the 3,5mm orthopaedic screw.

In this research, the 4,5mm POW threshold from Westermann *et al.* is used as an indicator for safe SSP, but it is important to note that there currently is no consensus on a specific definition of the minimal POW required for safe SSP [22]. Viswanathan *et al.* use a 3,5mm pedicle inner cortical width (PIW), which is similar to a 3,5mm cancellous bone width [33].

A study by Ludwig *et al.* chose a more elaborate approach [34]. Pedicles in which a 3,5mm screw had been inserted, have been measured and categorized based on size. Of the three groups

(<4,5mm; 4,5mm–5,0mm; >5,0mm) the share of accurate placements, noncritical breaches, and critical breaches has been reported. This took the concept of SSP safety into a scale variable dependent on pedicle width, instead of a binary ‘safe/not safe’ threshold variable.

In the POW group of under 4,5mm, only 35% (17/48) of the inserted screws were accurately placed. 31% of SSP’s showed noncritical breaches and 33% showed critical breaches. The group with a 4,5mm–5,0mm POW had no critical breaches; 55% (12/22) of the screws were accurately placed and 45% showed noncritical breaches. In pedicles with a POW of above 5mm, 79% (37/47) of the spinal screws showed no breaches [34]. One screw (2%), was critically misplaced.

It can be concluded from this study as well, that a POW of 4,5mm is large enough to minimize the risk of screw misplacements.

It should be noted that the share of breached screws is a result of small pedicle diameters and insufficient technical support –which a sensing surgical drill is supposed to improve. So, the percentage of patients that can tolerate a 3,5mm pedicle screw, could increase due to the development of a smart surgical drill.

Drill bits suited for 3,5mm screws usually have a diameter of 2,5mm to 2,7mm [21]. Without exception, a 2,7mmØ drill bit was used in all the surgeries visited for this thesis.

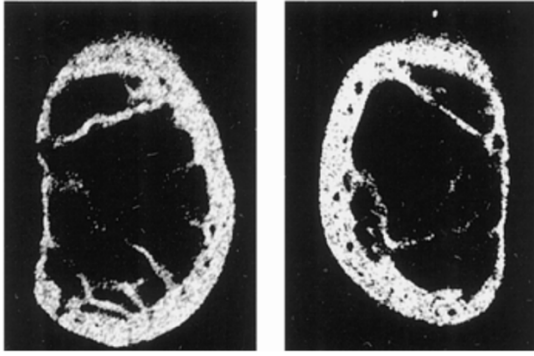


Figure 6. Radiographs of the left and right cervical pedicle in the coronal plane [35]

### Cortical Thickness (COT)

The literature research conducted prior to writing this thesis also collected data on the cortical thickness (COT) within the pedicle [21]. Analysing the COT is of importance because the sensing surgical drill developed for this thesis relies on tissue identification as a navigational guide. If a surgeon knows the drill tip is in a cortical bone layer, the tip is close to the bone surface and is therefore at risk of breaching it –causing the associated complications of pain, arterial bleeding or, in severe cases, paralysis [2].

If the system is based on cortical bone identification, the minimal COT is an indicator for how sensitive the system

should be; the drill should be accurate enough to identify tissue layers as thin as the COT. Furthermore, the sampling frequency of a sensing drill should be high enough to ensure that under a certain penetration velocity, the cortical bone layer cannot be passed by between two measurements.

Three studies reported on the COT, giving an overall average of 1,5mm [21] [22] [35] [36]. The COT however, varies widely within every single pedicle, as can be seen in Fig. 7. This corresponds with the findings on the cervical pedicle COT of Westermann *et al.*, shown in Fig. 8 [22]. While the superior, inferior and medial COT averages at approximately 2mm, the mean lateral COT is 0,90mm [21].

The different colours in Fig. 8 represent the different vertebrae, from C3 to C7. The smallest COT can be found in the light blue and the purple line. The light blue line represents the C7 vertebra and the purple line represents the C6. This could be considered surprising, because these vertebrae have a larger POW than the C3–C5 vertebrae, as the boxplots in Fig. 6 show.

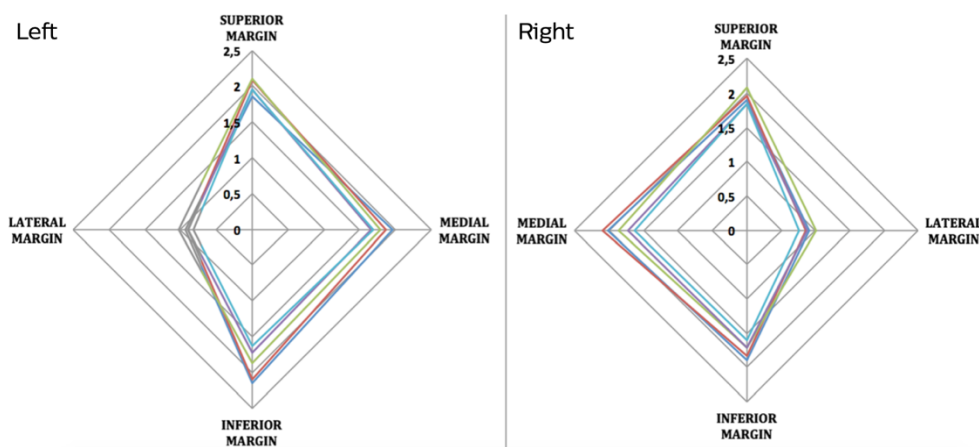


Figure 7. Cortical thickness (COT) in the pedicles of the cervical vertebrae C3–C7 [22]

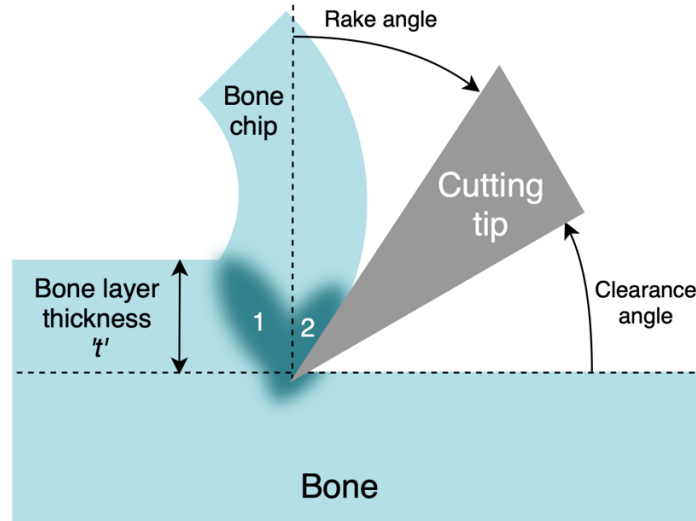


Figure 8. Schematic view of bone drilling with heat development in marked areas '1' and '2'

### 1.1.2. Thermal osteonecrosis

Mitigating collateral damage of bone drilling is not only a matter of minimizing orthopaedic screw misplacement rates. Bone drilling does not only crush the tissue it removes, but it also damages the tissue that remains through heat.

Rises in bone temperature can cause osteonecrosis: an irreversible death of bone cells (osteocytes), which can result in a longer recovery period and orthopaedic screw loosening [37]. Osteonecrosis is the result of depletion of osteocytes, reduction in blood flow and increased local osteoclastic activity [38].

Whether osteonecrosis takes place, depends on the tissue temperature and the duration of the exposure to this temperature [37]. It is found to occur when the bone is heated to 47°C for 1 minute, to 55°C for 30 seconds, or even immediately when the bone is heated to 70°C [37] [39] [40] [41] [42] [43] [44].

### Heat development

Essentially, a drill is a rotating chisel that removes material as shown in Fig. 9. A bone drill is pushed into bone tissue with a certain feed force, which determines the layer thickness ' $t$ '. The cutting tip removes tissue with a certain rotational speed, which is a result of the drilling machine's rotational force: the torque.

Heat production during drilling is described in the following equation, derived from a model by Heydari *et al.* [39]:

$$\dot{H}_t = \dot{H}_s + \dot{H}_f$$

Equation 1. Heat production during drilling

This differential equation shows that the total heat generated (in °C) is a summation of the heat caused by shear deformation  $\dot{H}_s$  and friction  $\dot{H}_f$ . In Fig. 9, shear deformation takes place in area 1 and friction takes place in area 2. In a third area, along the shaft of the drill (not shown in Fig 9), friction takes place as well. The heat development due to friction along the shaft of the drill differs



from the area 1 and 2, because its surface –the contact surface between the drill and the bone– increases as the drill penetrates the tissue. Since no bone tissue is removed along the shaft of the drill, this friction causes a heat increase without removing any tissue.

Various studies have shown that completely eliminating thermal osteonecrosis (without the use of cooling fluid) is not realistic [21]. Palmisano *et al.* found that when using several medical drills and K-wires on human cadaveric bone, a temperature increase high enough to cause instant osteonecrosis always takes place [38].

Studies that did not find such dramatic heat developments, usually measured tissue temperature through a thermocouple, placed at a (minimal) distance from the drilling surface. Hillery and Shuaib and Manoogian *et al.* however, integrated a thermocouple into a steel fixation pin or a drill bit. They measured temperatures as high as 115°C, while studies under comparable circumstances with thermocouples in bone reported temperatures of less than 40°C [39] [41] [42] [45].

Hillery and Shuaib suspected this was due to the insulation characteristics of bone, and they concluded that placing thermocouples within bone is not a suited way to measure bone temperature [45].

Therefore, it is not possible to know whether osteonecrosis has actually not taken place, when measurements derived from such methods show only a limited temperature increase. This is why it is expected that certain thermal

damage will always be caused during bone drilling.

Nonetheless, because the severity of thermal osteonecrosis depends on the height of the tissue temperature, and the exposure time, it can still be mitigated. An investigation on how to do so, has been done in the literature study conducted prior to writing this thesis [21].

### **Variables of bone drilling temperatures**

The dependent variable bone tissue temperature is influenced by numerous factors, which can be divided in independent and fixed variables.

The feed force, feed rate and the rotational speed are identified as independent variables; they can be manipulated by the surgeon during surgery. These variables influence each other as well [21]. E.g.: increasing the rotational speed of a drill increases the feed rate or decreases the required feed force. This can influence the total drilling time as well, resulting in both a shorter heat development time, as well as a shorter heat exposure time.

The fixed variables are variables that are essential to heat development, but cannot be manipulated by the surgeon – either because they are given circumstances, or because they are properties of the medical equipment. These variables are the tool sharpness (influencing the cutting tip sharpness, the rake angle and the clearance angle in *Fig. 9*), bone density, drilling depth and drilling diameter [21].

## Heat limiting measures

Limiting the drilling time has the largest effect on tissue temperature rises [46] [47]. Increasing the feed rate or decreasing the drilling depth could in theory be effective measures to do so.

However, a surgeon needs to carefully drill holes of a given depth that corresponds to the vertebral dimensions and the lengths of specifically selected orthopaedic screws. The pedicle axis length (PAL) goes up to 35mm [48]. Therefore, changing the drilling depth is deemed impossible. When manually drilling holes, (although it would be possible) applying a higher feed rate comes with a loss of drilling accuracy. Thus, increasing the drilling feed rate is considered as not desirable.

When using a specific (maximum) feed rate and a fixed drilling depth, mitigating thermal tissue damage, can be done by applying a low rotational speed and a high feed force [39] [41] [49].

The surgeon could use a relatively low rotational speed of approximately 500rpm, to limit total movement of the drill. Certain drill rotations will always be needed for tissue removal, but in this way, especially the friction along the drill shaft –which does not directly contribute to bone tissue machining– is reduced.

As the drill needs to cover a specific PAL or remove a specific amount of bone tissue, applying a lower rotational speed means that a higher amount of bone will have to be removed per rotation. In other words, a lower rotational speed would have to be combined with an increased bone layer thickness ' $t$ ', shown in *Fig. 9*. This requires a higher feed force.

How high this force exactly needs to be, depends on the tool sharpness, bone density etc., but the most common upper limit in bone drilling studies is approximately 40N [37] [43] [46] [47] [49].

Apart from using sharp tools and applying high feed forces with low rotational speeds, (concepts of) irrigated drills exist as well [50]. These drills use open or closed loop channels through which cooling water flows, to keep the temperature increase of the drill and the surrounding tissue to a minimum.

Although companies like Medtronic offer water cooled drills, most surgical equipment manufacturers do not, and these drills certainly cannot be considered as a standard in the current medical praxis [51] [52].



## 1.2. Diffuse Reflectance Spectroscopy (DRS)

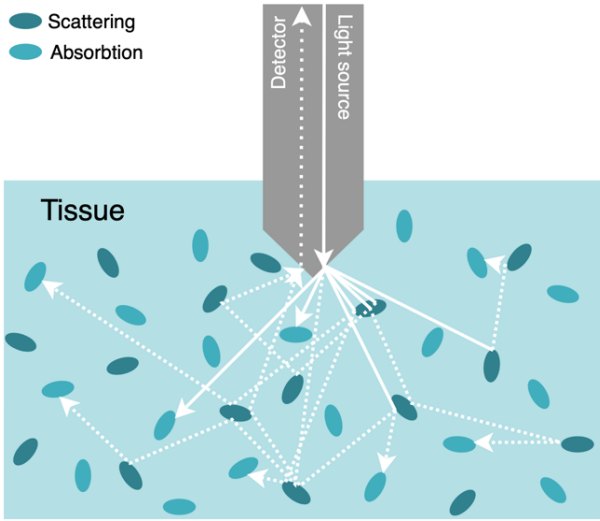


Figure 9. DRS scattering and absorption

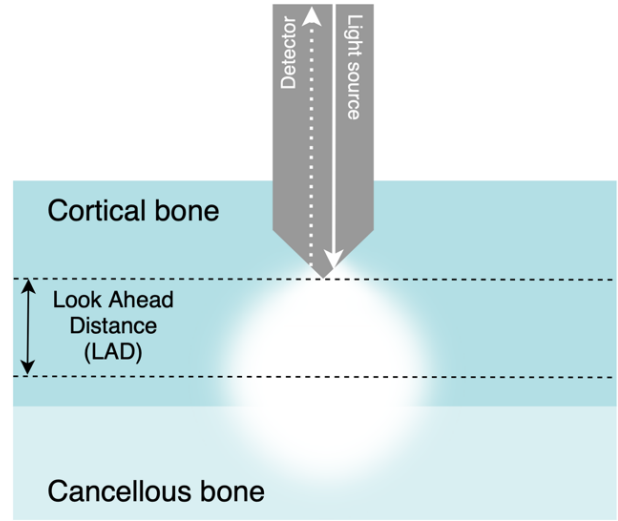


Figure 10. Light distribution and the LAD of DRS

Diffuse reflectance spectroscopy (DRS) is a technique that can be used to distinguish different tissue types, based on physiological composition [53]. Applications vary from tumorous tissue identification (malignant tissue formed through breast cancer for instance) to measuring the oxygenation of blood to examine lung performance or blood composition.

As light penetrates tissue, it interacts with chromophores, which can be categorized as the part of a molecule that is responsible for its colour (in the VIS spectrum). When the incident light  $I_o(\lambda)$  interacts with different molecules, it is either reflected, transmitted or absorbed, as described in Equation 2 and shown in Fig. 10 [56].

$$I_o(\lambda) = I_{reflected}(\lambda) + I_{transmitted}(\lambda) + I_{absorbed}(\lambda)$$

Equation 2. The behaviour of light in tissue

### 1.2.1. DRS Principles

When illuminating tissue with a selected spectrum of wavelengths, DRS measures the intrinsic light absorption and scattering in the near-infrared (NIR) and in the visible (VIS) spectrum [54]. These absorption and scattering properties produce a function of the reflected wavelengths that can be regarded as a 'signature' of a tissue type, also referred to as a tissue's 'optical fingerprint' [55].

The emitted light reaches a certain depth into the tissue; the longest distance travelled by any photon is called the penetration depth [57]. The detection or sampling depth however, is the depth reached by 50% of the emitted photons [58] [59]. It is also called the look ahead distance (LAD), shown in Fig. 11, as it is the distance at which DRS identifies tissue.

The LAD depends on several factors including the optical properties of the tissue, the geometry of the DRS instrument (such as the fiber distance), and the selected wavelengths of the light [58].

### 1.2.2. DRS-based fat fraction in bone

In the case of bone drilling, it is important to keep the drilling equipment and implants within the boundaries of the cortical bone to prevent damage to the surrounding tissue and vital structures, as discussed in Section 1.1. It is therefore of interest to surgeons to receive live feedback on in which tissue type their surgical instruments are located.

When drilling through cancellous bone, the risk of breaching the bone surface is low. If the drill reaches the cortical bone however, it is approaching the bone-tissue boundary. When ensuring the drill will always stay within the cancellous bone, the cortical bone layer can act as a buffer, which is needed since a screw is wider and it travels deeper than the drill bit.

A DRS spectrum can be translated into several physical properties such as the absorption coefficient  $\mu_a(\lambda)$  or the reduced scattering coefficient  $\mu'_s(\lambda)$  expressed in  $\text{cm}^{-1}$  [60]. A differentiation of cortical and cancellous bone can be made, based on the DRS-derived fat (or lipid) fraction. Red bone marrow consists of lipids for 40% to 60% and yellow marrow is composed of lipids for 80%. Cortical bone however, mainly consists

of hydroxyapatites and mineral salts, also referred to as bone mineral [61] [62].

A fat fraction decrease indicates that the drill is leaving the cancellous bone and it is headed –via the cortical bone– towards the bone surface. The aim of this research to verify whether a DRS derived fat fraction decrease can ensure a timely halt of the drill, before a cortical breach occurs.

### 1.2.3. State of the art

The abovementioned theory of DRS bone identification during drilling or the placement of implants is confirmed as a proof of concept in research by, among others, Swamy *et al.* and Duperron *et al.* [57] [63] [64] [65].

Duperron *et al.* created a fiber-equipped surgical drill and observed the reflected wavelengths of 470nm and 780nm. A cancellous to cortical bone boundary was detected when the ratio between these two wavelengths dropped by 0,35 arbitrary units (a.u.) per second [57].

With the drill travelling at 1mm/s, an automated drill stop based on the 0,35 a.u./s threshold, ensured a timely halt of the drill in a mere 50% of the cases [57]. So, half of the cases showed the proof of concept of a promising technique, while the other half showed the necessity to improve its accuracy before it can be applied in the OR.

Instead of looking at a wavelength ratio drop in a.u./s, the preferred approach in this research is tissue identification based on fat fraction. The advantage of this method, is that a fat fraction value is independent of the feed rate. A drop in a wavelength ratio per second due to a difference in fat fraction  $\Delta fat(\%)/s$ , depends on fat fraction transition per millimeter in the tissue  $\Delta fat(\%)/mm$  (the organic transition from cancellous to cortical bone) and the feed rate at which a drill passes it  $mm/s$ , as shown in Equation 3.

$$\Delta fat(\%)/s = \frac{\Delta fat(\%)/mm}{mm/s}$$

Equation 3. The fat fraction change per second, causing a wavelength ratio drop in a.u./s

If a drill enters a different tissue layer at a low feed rate, the drop in a.u./s is possibly not high enough to reach the threshold. A certain fat fraction however, could serve as a trigger, regardless of the drill's feed rate or previous measurement.

The fat fraction-based bone tissue identification has been done through probes and the placement of a fiber-equipped orthopaedic screw in several studies by, among others, Swamy, Bursröm, Spliethoff. [63] [64] [65]. The research shows promising results regarding accurate cortical bone detection. In contrast to the research by Duperron *et al.* however, Swamy *et al.* recorded the spectra while the optical screw probe stood still in the tissue. After each turn, a DR spectrum was taken [63].

A next step in the development of DRS drills is to study the DRS derived fat fraction at different drilling feed rates, to verify its accuracy while more closely mimicking the clinical praxis.

## 1.3. DRS drill concepts

Two challenges have to be overcome in order to create the hardware of a DRS fiber-equipped drill. The fibers have to be integrated into the drill bit and the fibers also have to be connected to a DRS-console.

### 1.3.1. Fiber integration and connection

Integrating optical fibers into a drill bit can essentially be done in two ways, as shown in *Fig. 12*:

1. **Rotating fibers:** integrating optical fibers into the drill bit and have them rotate along with it.
2. **Stagnant fibers:** integrating fibers into a non-rotating (stagnant) probe and insert this fiber-equipped probe into a rotating cannulated drill.

#### Rotating fibers

The first option has the advantage that the drill is physically similar to a regular bone drill with irrigation channels. The axial rotational forces are identical to currently applied bone drills, because the drilling surface (the tip that chisels away tissue) is identical.

It has disadvantages as well. The available DRS console emits and collects light signals through a physical connection with wires. Wires that rotate at 500rpm, will be tangled up immediately.

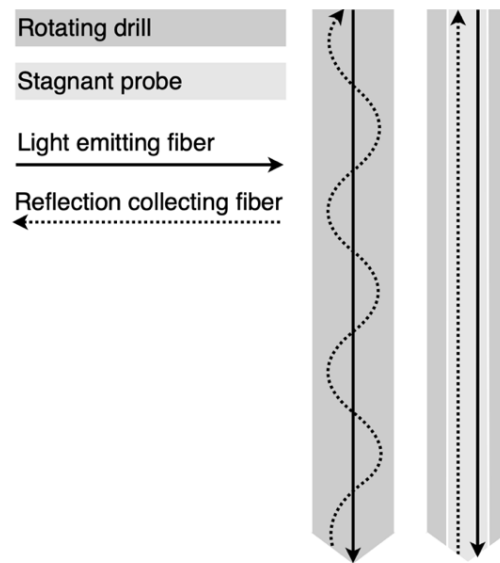


*Figure 11.* DRS drill concepts: rotating fibers (left) and a stagnant fiber-equipped probe (right)

Duperron *et al.* have developed a physical coupling that connects the rotating drill with external light sources and collectors, shown in *Fig. 13* (on the next page) [57]. A rotating reflected light collector could possibly also be wirelessly connected through a digital radio signal.

#### Stagnant fibers

The second option, the stagnant fiber-equipped probe, has specific advantages too. There are no problems regarding the coupling to the DRS-console, as optical wires can be connected directly to the stagnant probe (they will not rotate during the drilling).

This is not only a quick and practical solution for the development of a test setup; it could be clinically relevant as well. If the system proves useful in bone

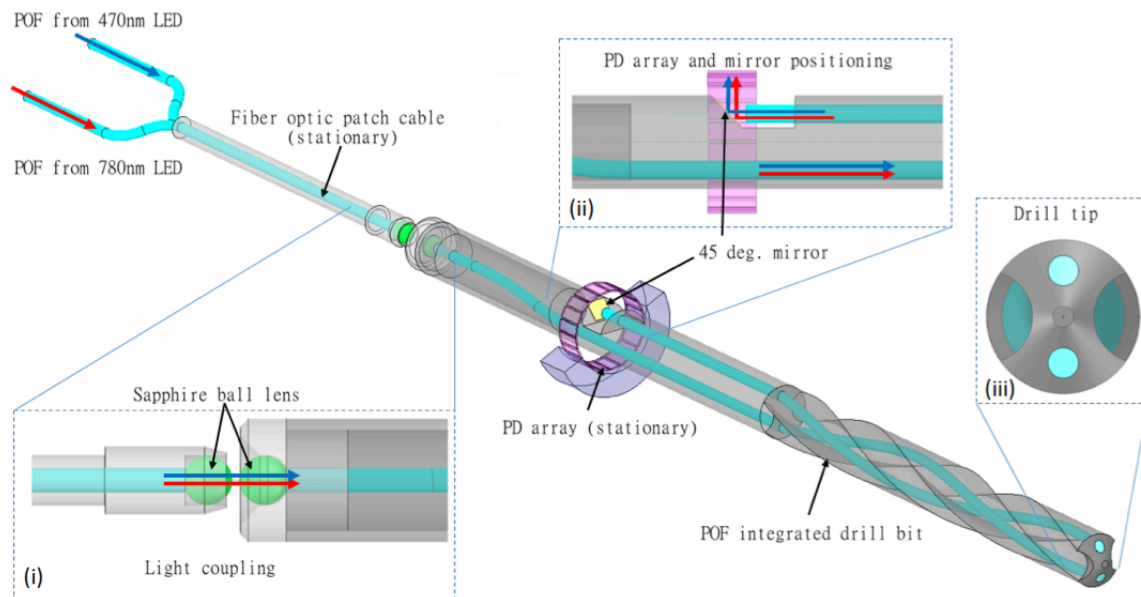


Figure 12. A rotating DRS fiber-equipped drill developed by Duperron et al. [35]

drilling, a reusable stagnant DRS-probe can be introduced into currently available orthopaedic drills. This provides a widely applicable, relatively low-price tissue identification solution, compared to a complete drill, developed to identify tissue through DRS.

However, using a stagnant probe has disadvantages as too. It is expected that axial drilling forces need to be significantly higher, due to the fact that part of the drill-tip does not rotate and chisel away bone tissue. It merely is a sharp probe that needs to be pressed into bone, while the cannulated drill – which has a smaller drilling surface than a regular drill, as can be seen in Fig. 5– rotates around it, removing bone tissue.

The magnitude of the mechanical effects of this design choice is unknown. Therefore, experimental testing is required to see whether the expected increase of axial forces falls within the range of forces that can be applied by surgeons during delicate spine surgeries.

### 1.3.2. Concept selection

Both the rotating and the stagnant fiber concepts have their strengths and weaknesses, but based on the financial and time limitations of this master thesis the stagnant fiber-equipped probe concept is selected.

A fiber-equipped probe was readily available at Philips prior to starting this research. A rotating fiber system like the one created by Duperron *et al.* in Fig. 13, requires the purchase or machining of a wide range of parts, such as a ball lens coupling, a circle of PD-arrays and elaborate optical fiber integration [57]. The stagnant probe concept however, only required a cannulated drill with a suited channel diameter. This made the concept considerably more attractive regarding this project's timespan and financial costs. Furthermore, copying a drill such as the one developed by Duperron *et al.*, offered no advancements in the exploration of DRS drill concepts [57].

Lastly, it was interesting to develop the stagnant probe concept due to its clinical relevance. If the system proves effective to bone drilling, a reusable stagnant DRS-probe can be introduced into currently available orthopaedic drills. This provides a widely applicable, relatively low-price tissue identification solution, compared to a complete drill, developed to identify tissue through DRS, as mentioned in the previous Paragraph 1.3.1.

## 1.4. Research questions and hypotheses

As discussed in Section 1.2., several studies have already succeeded in identifying tissue types and differentiating cortical and cancellous bone through spectroscopy [57] [63] [64] [60]. Duperron *et al.* have also conducted experiments with a DRS fiber-equipped drill –even introducing an automated drill stop with varying degrees of success [57]. This can be regarded as a proof of concept of a DRS fiber-equipped surgical drilling instrument. This research focuses on DRS-tissue identification at various feed rates.

### 1.4.1. Feed rate speed limit

To progress this field of research, a next step is to increase the accuracy of DRS fiber-equipped drilling instruments. The accuracy is currently insufficient, as a mere 50% of the automated drill stops ensured a timely halt at a cancellous-cortical bone boundary [57]. One way of possibly improving this accuracy, is to study the way the DRS-signal behaves at different penetration speeds.

So far, drilling DRS tissue identification has been done in either a stationary manner or at a feed rate of 1mm/s [57] [63]. Varying the feed rate could provide insights into how the DRS-signal behaves when optical measurements are taken while drilling. More specifically, a feed rate ‘speed limit’ can be established, which can be compared to feed rates that are currently applied by surgeons.

It is of interest to eventually develop a system that has a higher speed limit than the feed rate surgeons prefer to use. Furthermore, a higher speed limit would decrease the drilling time and would therefore limit the occurrence of thermal osteonecrosis (discussed in Paragraph 1.1.2). If the speed limit of the setup in this research proves insufficient for the current surgical practice, opportunities for improvement can be identified.

#### Question

What is the maximum feed rate at which the DRS fiber-equipped drilling instrument can be used to ensure no tissue boundary breach takes place when the drill approaches a cancellous to cortical bone tissue boundary?

#### Hypothesis

In a simplified model, the maximum feed rate has been derived from the so called ‘overshoot’. The overshoot is in this case defined as the distance (in mm) that a drill travels beyond the optical tissue detection, while the optical signal is processed. It can be identified through *Equation 4*, using the feed rate  $v$  (mm/s), the integration time  $t_{integration}$  (s), and the LAD. The integration time is presumed to dictate the DRS-system’s sampling frequency, along with a ‘dead’ or inactive period between two measurements, which is expected to be negligible.

$$Overshoot = (v \cdot t_{integration}) - LAD$$

*Equation 4.* Hypothetical drilling overshoot determination

As shown in *Table 1*, several studies have deemed minor cortical breaches to be acceptable, which would allow a small overshoot. In this study however, the aim is to completely eliminate breaching screws, so the maximal overshoot is chosen to be 0mm. The remaining cortical bone can act as a buffer, as discussed in Paragraph 1.2.2.

The LAD varies, based on (among others) selected wavelengths, tissue types and fiber distance [58] [59]. Duperron *et al.* have reported a 0,25mm LAD while observing wavelengths of 470nm and 780nm, using a 1,5mm optical fiber distance on bovine bone [57]. Swamy *et al.* used the full spectrum from 400nm to 1600nm and found that the DRS-derived fat fraction started dropping more than 1mm before tissue boundary was reached [63]. Although this does not meet the definition of the LAD, it suggests that the LAD might be larger than 0,25mm when observing the full spectrum.

A 0,2s integration time is assumed, derived from studies by Duperron *et al.* and Evers *et al.*, resulting in a 5Hz sampling frequency [57] [65].

Using the abovementioned values in *Equation 4*, the maximum feed rate is estimated at 1,25mm/s. This would be lower than the average 1,5mm/s or the occasional feed rates of above 4mm/s, which were recorded during a surgery visit for this thesis (notes can be found in Appendix 7.1.1.). If the maximum feed rate is 1,25mm, the DRS drilling system would have to become more accurate before it will be applicable to surgical procedures.

## 1.4.2. Axial forces

As mentioned in Paragraph 1.3.1., the selection of the stagnant fiber-equipped probe concept has mechanical implications. Because the drill design features a smaller tissue removing surface than a regular drill (due to the introduction of the stagnant probe) it is expected that the axial drilling forces will have to be higher to penetrate bone tissue. To verify whether this design can be clinically relevant, the magnitude of this force increase needs to be identified.

### Question

What is the difference in axial drilling forces, required to penetrate cancellous and cortical bone tissue, between a drill with a centred stagnant probe and regular bone drill?

### Hypothesis

As no data could be found on forces required to push a stagnant K-wire into bone tissue, a simplified model, shown in *Equation 5*, has been used to estimate axial forces.

$$\Sigma F = V_{bone} \cdot C_{bone} \cdot \left( \frac{A_{bone}}{A_{machining}} \right)$$

*Equation 5.* Axial force estimation in bone drilling

Assuming a constant feed rate, rotational speed, motor torque etc., the sum of the axial forces  $\Sigma F$  (N) can be estimated by multiplying the bone volume that needs to be removed  $V_{bone}$  (mm<sup>3</sup>) by a constant material property of bone –the drilling force required to remove a square millimetre of bone–



$C_{bone}$  (N/mm<sup>3</sup>) and the ratio (a.u.) of the to-be-removed bone surface  $A_{bone}$  (mm<sup>2</sup>) divided by the machining surface of the tissue removing drill  $A_{machining}$  (mm<sup>2</sup>).

A stagnant probe does not remove or ‘chisel away’ any tissue, as it merely pushes tissue sideways towards the incoming machining surface of the drill. Thus, introducing a stagnant probe into a bone drill would increase the required axial forces through the increased surface ratio, because the machining surface decreases while the bone surface stays constant.

When using a regular bone drill or a cannulated one with a probe, the bone constant  $C_{bone}$ , and the to-be-removed tissue  $V_{bone}$  is similar. The difference can be found in the bone-machining surface ratio. A regular 2,7mm diameter drill has a ratio of 1: the bone surface is similar to the machining surface. Using *Equation 6*, a 2,7mmØ drill with a 1,7mmØ channel for a 1,6mmØ fiber-equipped probe has a bone-machining surface ratio of 1,54 a.u.

$$\left( \frac{A_{bone}}{A_{machining}} \right) = \left( \frac{2\pi r_{bone}^2}{2\pi r_{drill}^2 - 2\pi r_{channel}^2} \right)$$

*Equation 6.* The bone-machining surface ratio

Based on *Equation 6*, a force increase of 54% is predicted. The (relatively high) drilling force of 40N mentioned in Paragraph 1.1.2. is therefore expected to increase to 62N. In a study on force sensing in a robotic spinal surgery system, Hu *et al.* measured peak forces of 14N while using a 3mm diameter drill on bovine vertebrae at a 0,5mm/s feed

rate with an 8000rpm rotational speed [66]. With adjacent averaging, the peak forces were approximately 7N; using a drill with a stagnant probe, these would increase to 10,8N.

It should be noted that this model assumes the stagnant probe to have an infinitely sharp tip that guides bone towards the drilling or machining surface in a frictionless manner. In practice however, it can be expected that the axial forces will show a higher increase than predicted; pushing a blunt probe into tissue requires more force than penetration with a sharp one.

Correspondence with surgeons revealed that an increase of the forces required to perform surgery, causes a decrease in a surgeon’s accuracy; the potential error (the possible difference between a surgical instrument’s intended location and its actual location) becomes larger.

During interviews with four orthopaedic surgeons no maximum drilling force could be established. The surgeons do not quantify the pressing forces they exert, but they did express a desire to keep the forces as low as possible.

There was a lower limit to the drilling forces as well, since diseases such as osteoporosis decrease the resistant forces of bone in such a degree that a drill could shoot through the bone, causing the previously described physical damage. Notes of the conversations with surgeons can be found in Appendix 7.1.1.

## 2. Methods

In order to answer the research questions formulated in Section 1.4., an optical and a mechanical experiment are conducted. DRS-based fat fractions and drilling forces are measured, using a custom drilling unit mounted onto a linear stage.

Statistical analyses will show how drilling feed rates influence the optical tissue boundary identification, and whether introducing stagnant probes into a drill influences the forces required to penetrate tissue.

This chapter will discuss the two experiments conducted in this research. In Section 2.1., the variables of the experiments are elaborated, as well as the drilling setup, the properties of the used bone phantom, and the analyses performed on the gathered data.

In Section 2.2., every component of the drilling setup –from the stepper motor to the drill bits– is briefly discussed.

The Delft University of Technology Minimally Invasive Surgery and Interventional Techniques (MISIT) Lab does not allow for real bone usage, and the available fiber equipped-probe is not designed for solid tissue penetration like real bone either. Thus, different phantoms that mimic optical or mechanical bone properties have been produced or purchased. The bone phantoms are discussed in Section 2.3.

Section 2.4. discusses statistical analyses used in this research.

## 2.1. Experiments

Two experiments are conducted to answer the research questions formulated in Section 1.4. The first consists of taking optical measurements to identify how timely the DRS-signals can detect an approaching tissue boundary under varying feed rates. A rotating cannulated drill is used in combination with an optical fiber-equipped probe.

To study the mechanical implications of introducing a stagnant probe, the second experiment measures the axial drilling forces of probe-equipped drills under varying feed rates. The experimental setup is shown in Fig. 14 and Fig 15.

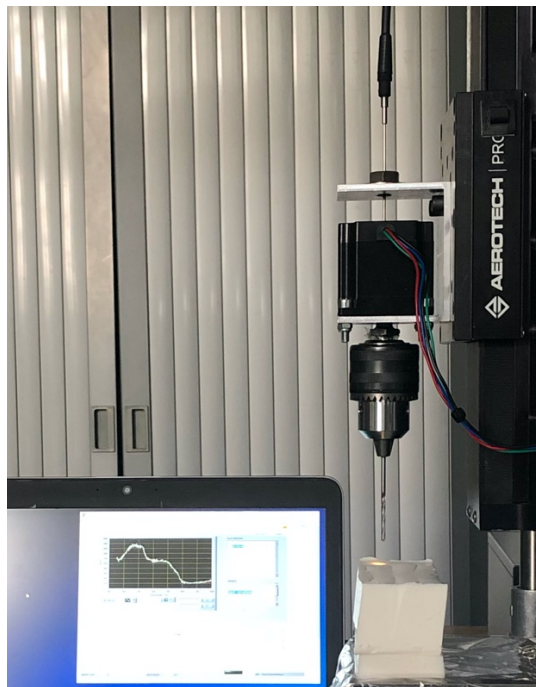


Figure 13. Picture of the (optical) experimental setup used in this research

### 2.1.1. Optical experiment

The optical experiment focuses on two variables:

**The independent variable** is the feed rate. It is the speed at which the drill moves through the tissue boundary of the optical bone phantom (see Fig. 15). The feed rate is manipulated by the linear stage to 0,5, 1, 1,5 2, and 2,5mm/s.

**The dependent variable** is the overshoot, determined as the discrepancy in millimetres between the optical DRS-detected location and the actual location of a tissue boundary.

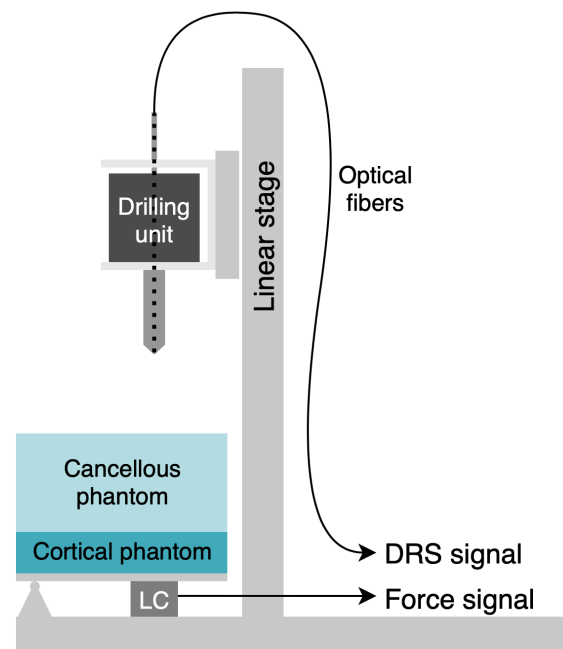


Figure 14. Schematic view of the experimental setup used in this research

This boundary occurs when the drill moves, through an optical cancellous bone phantom into a cortical bone phantom.

Every drilling cycle is filmed, to identify at which DRS-measurement the drill enters the phantom tissue. As the linear stage feed rate, as well as the thickness of the optical bone phantom is known, the actual tissue boundary location can be projected onto the optical measurements.

Details of the linear stage, DRS tissue identification and the bone phantom can be found in Section 2.2 and 2.3. A picture of the optical drilling setup can be found in Appendix 7.2.1.

### 2.1.2. Mechanical experiment

The mechanical experiment uses three variables, two independent and one dependent variable:

**The first independent variable** is the drill type. A regular 2,7mmØ orthopaedic drill, a 1,35mmØ cannulated 2,7mmØ orthopaedic drill and a 1,7mm cannulated 2,7mmØ orthopaedic drill have been used. The cannulated drills provide a channel for K-wires with diameters of respectively 1,25mm and 1,6mm.

Because the tip of the optical probe used in this research is not made to pierce through the solid mechanical bone phantom (the tip is blunt and the steel is hollow), K-wires designed for orthopaedic surgery are used.

**The second dependent variable** is the feed rate, similar to the optical experiment. The feed rates are manipulated by the linear stage to 1mm/s, 2mm/s, 3mm/s and 4mm/s.

**The dependent variable** is the axial drilling force required to penetrate the mechanical bone phantom, expressed in Newton. The force is measured through a load cell (LC in *Fig. 15*) placed under the bone phantom. It is of interest to examine the axial drilling forces as these have to be expressed by the surgeon during SSP procedures.

Because the load cell is connected to the linear stage, the axial forces are reported in combination with their location. These can directly be linked to the known dimensions of the mechanical bone phantom.

Details on the drill bits, the linear stage and the load cell can be found in Section 2.2. and 2.3.

## 2.2. Drilling setup

As briefly discussed in Section 2.1., in order to control the feed rate and the rotational speed during bone drilling experiments, a linear stage is used with a drilling unit, shown in *Fig. 16*, mounted onto it. The linear stage provides the possibility to vary the drilling feed rate, and to determine the drill tip's exact location.

A cannulated stepper motor, which is attached to the mount that connects to the linear stage, can rotate at specifically selected speeds. Through its cannulation –the axis is hollow–, several K-wires and DRS fiber-equipped probes can be inserted into the drilling unit, and kept in place by the mount. A common drill chuck is attached, so that various drill bits can be used.

Being able to use different drills, probes rotational speeds and feed rates is required to conduct this research. Furthermore, it provides a test setup for future experiments in manipulating these variables.

### 2.2.1. Mount

The aluminium mount of the drilling setup, which can be seen in *Fig. 16*, is the central part that connects the key components of this experiment. It is connected to the linear stage, the stepper motor is attached to it, and it provides the possibility to clamp probes and K-wires.

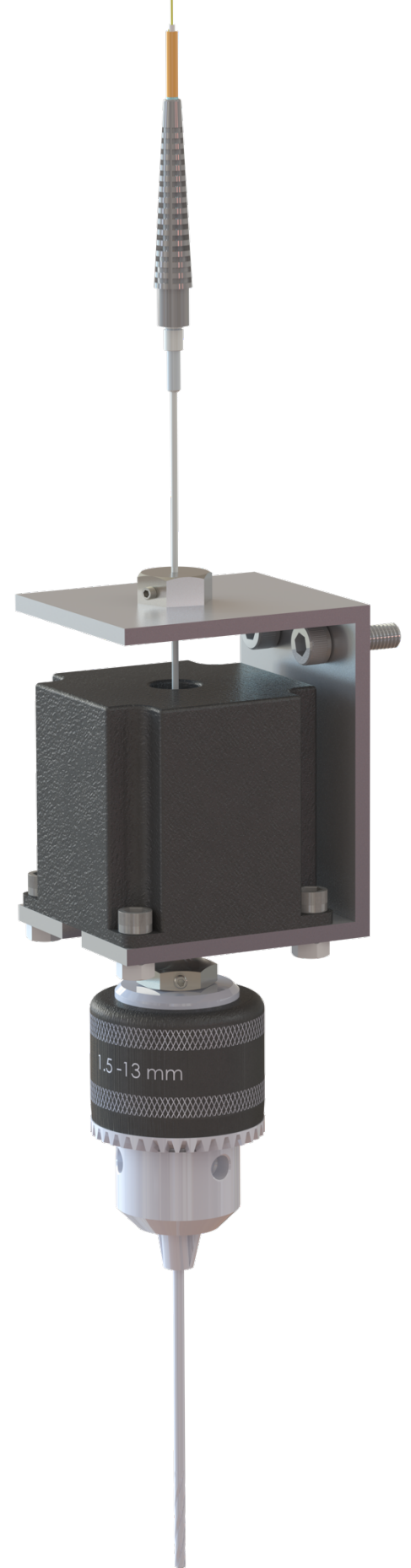


Figure 15. The DRS-drilling unit

The mount has been custom designed for this research. Technical drawings of the mount and its custom accessories can be found in Appendix 7.2.2.1. On the bottom, it features a machined circle that centres the stepper motor, and four holes for bolts. The back (vertical plate) features holes for two M6 bolts at a 25mm distance, compatible with standard stepper motor tabletops.

The top features a tapped hole for an M10 bolt in which the probes can be clamped. Two bolts have been customized with a 1,25mmØ and a 1,6mmØ channel along the axis for the K-wires and optical probe. The bolts also feature perpendicular tapped channels for a clamping M2,5 bolt, to eliminate vertical movement of the probe and K-wires, relative to the drilling unit.

### 2.2.2. Stepper motor

The stepper motor used in the test setup is a Makeblock 57BYG motor, which falls into the category of NEMA 23 stepper motors. It has been selected for two reasons:

1. Rotational speed control
2. Torque output

In order to study the mechanical effects of varying the feed rate, it is important to keep the rotational speed constant. In this research, a rotational speed of 500rpm is used, but for future experiments, the stepper motor provides the opportunity to use desired rotational speeds.

NEMA 23 stepper motors are commonly used for their relatively high torque output. Where smaller stepper motors such as the NEMA 14, 16 and 17 are commonly used in devices like 3D-printers to accurately control the location of the printing nozzle, NEMA 23 models are also used in CNC milling machines [67] [68] [69].

The literature study written prior to this research reports torque values of 0,5Ncm to 2Ncm in bone drilling, with an exceptional peak of 4Ncm [21].

The torque output of a stepper motor is dependent on the model type, the power supply and the rotational speed of interest. The NEMA 23 model has been selected due to its sufficient torque: a holding torque of 1,2Nm. It has been connected to a 12V power supply and a Makeblock 2H microstep driver. The specifications of the Makeblock 57BYG motor, as well as a NEMA 23 stepper motor torque diagram can be found in Appendix 7.2.2.2.

The stepper motor requires a short period of acceleration to build up sufficient inertia for a 500rpm rotational speed. The Arduino® code to program the acceleration, the rotational speed and the rotation time can be found in Appendix 7.2.2.2. as well.

The stepper motor is cannulated 3mmØ all the way through the length of motor axis to provide a frictionless channel for the K-wires and optical probe. Under the mount, the drilling parts are attached to the axis.

### 2.2.3. Linear stage and load cell

The linear stage used in this research is an Aerotech PRO115SL. The product catalogue featuring its specifications and dimensions in Appendix 7.2.2.3., states this stage has a vertical (axial) load capacity of 18kg (177N). In the literature study on conducted prior to writing this research, one remarkably high peak load of 164,8N has been measured [41]. Most studies however, had axial load values of 20N to 40N [37] [49] [46] [47] [43]. The linear stage has a maximum speed of 300mm/s.

The linear stage is connected to a 25 lbs (11,3kg) FUTEK® load cell. The load cell has been placed under a hinge on which the bone phantom lays. It is aligned with the drilling trajectory, as shown in *Fig. 15*. Specifications of the load cell can be found in Appendix 7.2.2.3. as well.

### 2.2.4. Drilling parts

Attached to the axis of the stepper motor, the drilling parts can be found. They consist of a drill chuck (with an SDS adapter), the surgical drill bits, the optical fiber-equipped probe and two K-wires.

#### Drill chuck

The drill chuck is a common chuck, that provides the possibility to use various 1,5mmØ to 13mmØ drill bits. The drill chuck connects to the axis of the stepper motor via a customized SDS adapter with a channel that fits onto the surface

of the axis. To minimize the length of the entire drilling unit –and therefore providing the possibility to use shorter probes and K-wires– the SDS-connecting part is sawn off of the adapter. This leaves the screw thread to which the drill bit connects, and a short axis interface. The adapter features a custom tapped hole for a 2,5mmØ bolt to clamp onto the axis, similar to the way the M10 bolts of the mount clamp onto the probes and K-wires. A technical drawing of the customized SDS adapter can be found in Appendix 7.2.2.4.

#### Surgical drill bits

As mentioned in Paragraph 2.1.2., three types of drill bits have been used: a regular 2,7mmØ orthopaedic drill, a 1,35mmØ cannulated 2,7mmØ orthopaedic drill and a 1,7mmØ cannulated 2,7mmØ orthopaedic drill, all produced by Marquardt Medizintechnik GmbH. The 1,7mmØ cannulated drill has been modified from a 1,25mmØ channel drill through electrical discharge machining by Philips Innovation Services. The AO couplings have been sawn off to shorten the drills, making the setup compatible with shorter K-wires. *Fig. 17* shows the 1,35mmØ cannulated drill (left), 1,7mmØ cannulated drill with 1,60mmØ K-wire (middle) and regular drill (right).

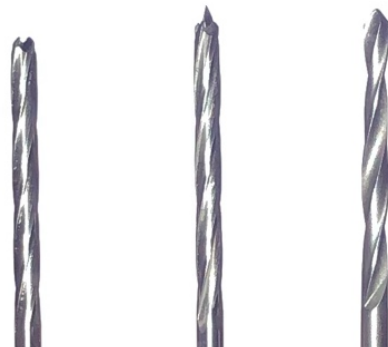


Figure 16. Drill bits used



Cannulated surgical drills are currently used to be inserted over K-wires that have already been placed into bone [70]. This way, the wire acts as a guide of the drill and of cannulated orthopaedic screws. As drilling with a stagnant probe integrated into the drill bit is a novel concept, the mechanical experiment discussed in Paragraph 2.1.2. is of interest.

### Optical probe

As mentioned in Section 1.3., an optical fiber-equipped probe has been used to perform DRS measurements on optical phantom bone tissue. The 1,60mmØ optical probe contains a light emitting, and a reflection collecting optical fiber. The 200µmØ low-OH fibers from Ocean Optics with an NA of 0.22 are at a core-to-core distance of 1,22mm.

The fibers meet the probe surface at a flat tip that resembles a (relatively thick) slot screwdriver, as can be seen in *Fig. 18*. Because this tip is not designed to puncture solid materials such as cortical bone and the mechanical bone phantom, K-wires with a trocar tip have been used in the mechanical experiment. This mechanical limitation does not occur in the optical experiment as it uses a relatively soft, gelatin-based phantom.

### K-wires

In the mechanical experiment, 1,25mmØ and 1,60mmØ stainless steel De Soutter Medical Stericut K-wires have been used. The trocar-tip, shown in *Fig. 18*, features a sharp point that is used for bone penetration in orthopaedic surgery. The label of the 1,25mmØ K-wire can be found in Appendix 7.2.2.4.

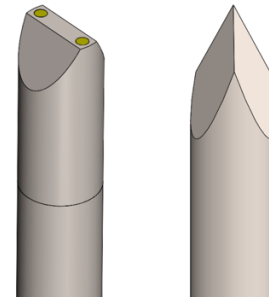


Figure 17. The tip of the optical fiber-equipped probe (left) and a trocar-tip K-wire (right)

## 2.2.5. DRS equipment

This research uses a DRS console that is, among others, featured in previous research by Nachabé and Hendriks [53] [71].

The optical fibers are connected to the DRS console. This console features an incandescent tungsten halogen broadband light source with an integrated shutter (Ocean Optics, HL-2000-HP) and two separate spectrometers. One fiber can be connected to the VIS wavelength region spectrometer with a silicon detector (Andor Technology, DU420A-BRDD) and the other fiber can be connected to the NIR wavelength region spectrometer with an InGaAs detector (Andor Technology, DU492A-1.7).

### Tissue identification

As mentioned in Paragraph 1.2.1., the differentiation between cancellous and cortical bone –which indicates the drill is approaching the bone surface– can be done based on fat fraction. The unique optical properties of fat can be found in the NIR-spectrum, between wavelengths of 1000nm and 1600nm [53] [63].

## Sampling frequency

The sampling frequency of the DRS console is of importance for bone drilling as a high frequency ensures small distances between tissue identification measurements. This way, a sensing drill can quickly identify approaching tissue boundaries, and the chance decreases of passing by a tissue layer unnoticed.

Reaching a high sampling frequency  $F_s$ , as shown in *Equation 7*, depends on the sampling time: time required to take a single DRS shot. In order to acquire reflected light, the console applies an integration time  $t_{integration}$ , similar to the shutter time of a photo camera. The integration time is followed by an inactive period  $t_{inactive}$ , in which the console pauses between two measurements.

$$F_s = \frac{1}{(t_{integration} + t_{inactive})}$$

*Equation 7.* DRS sampling frequency determination

The shorter the integration and the inactive time can be, the higher the sampling frequency is, but this approach features a trade-off. When the integration time is shortened, less reflecting light is collected. This decreases the optical signal intensity (in a.u.) and thus, the signal-to-noise ratio. This can reduce the DRS device's ability to accurately identify tissue.

## Spectrum measurements

The spectrometers in the DRS console are connected to a laptop which runs the in LabView developed program FlexPN, which obtains the measured spectra.

FlexPN (among many options) provides the opportunity to manipulate the integration times of both the VIS and the NIR spectra.

The calibration procedure consists of the measurement of a white reflectance standard (LabSphere, WS-1-SL) over the full VIS and NIR spectrum. A fiber splitter is used, as the optical probe has one reflection collecting fiber, while the DRS console features separate VIS and NIR reflection connections.

Because this research focuses on fat fraction determination, the NIR spectrum is of interest. Therefore, after the calibration, the splitter is removed and the reflection collecting fiber of the optical probe is connected to the NIR wavelength region spectrometer only, thereby removing the undesired light transmission reduction of at least 50%, caused by the splitter.

A background measurement has been performed to minimize the influence of ambient light, dark current, and electric offsets of the detector. The possibility to do continuous background measurements has been turned off in order to reduce the sampling time.

For the VIS wavelength region spectrometer (which receives no light signal), the integration time is reduced to its absolute minimum of 0,006s. The resulting VIS spectrum is not taken into account. For the NIR spectrum, the trade-off between signal intensity and sampling frequency resulted in an integration time of 0,1s.

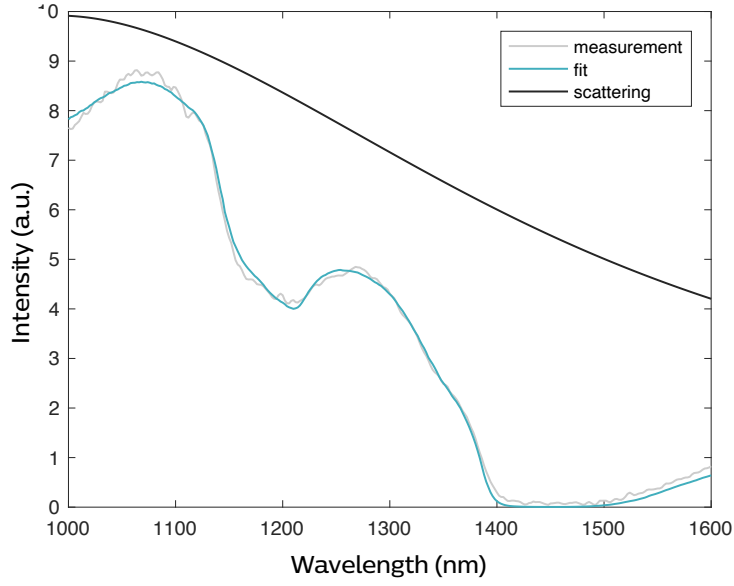


Figure 18. A spectrum of gelatin lipid phantom tissue

Whether this integration time proved to be sufficient for tissue identification has been examined by manually observing individual spectra. This has been done with particular interest in the characteristic reflection dip (or absorption peak) that lipid spectra show at approximately 1200nm [53] [63]. An example of a 0,1s NIR integration time spectrum is shown in Fig. 19.

The spectra are subsequently analysed though software named PNSas, which features fitting and plotting programs. The fitting is done through a model first developed by Farrell *et al.* which uses a Levenberg- Marquardt nonlinear least-squares inversion algorithm to estimate the absorption coefficient  $\mu_a(\lambda)$  and the reduced scattering coefficient  $\mu'_s(\lambda)$  ( $\text{cm}^{-1}$ ) [74] [75].

The (DR) reflection coefficient  $R[\mu_a(\lambda), \mu'_s(\lambda), \rho]$  is a function of the absorption coefficient, the reduced scattering coefficient and the fiber distance  $\rho$ .

The absorption coefficient due to water and fat (or lipid) derived chromophores is expressed in Equation 8. The absorption coefficients  $\mu_a^{\text{water}}$  and  $\mu_a^{\text{lipid}}$  represent the absorption coefficients of pure water and pure lipid. The  $f_{\text{water+lipid}}$  and  $f_{\text{lipid/(water+lipid)}}$  represent the fraction of water and lipid in the total measured substance, and the fraction of lipid within the water and lipid fraction respectively.

A multiplication of  $f_{\text{water+lipid}}$  and  $f_{\text{lipid/(water+lipid)}}$  –which are outputs of the PNSas fit program MainBatchFit– gives the fat fraction of the total measured substance.

$$\mu_a^{\text{water+lipid}}(\lambda) = f_{(\text{water+lipid})} \left[ f_{\frac{\text{lipid}}{(\text{water+lipid})}} \mu_a^{\text{lipid}}(\lambda) + \left( 1 - f_{\frac{\text{lipid}}{(\text{water+lipid})}} \right) \mu_a^{\text{water}}(\lambda) \right]$$

Equation 8. The water- and lipid-based absorption coefficient

## 2.2.6. Electrical circuit

A simplified electrical circuit of the experimental setup is shown in Fig. 20. Particular detail is provided for the stepper motor and its accessories, since these parts have been put together for this experiment specifically. The setup is compatible with a range of linear stages and the optical experiment uses DRS equipment applied in other research as well [63] [71].

A distinction has been made between MacOS and Microsoft® Windows computers (MacBook and HP®) as certain interactions between MatLab® and Excel® (applications used for the PNSas program), such as XLSREAD and XLSWRITE do only function on Microsoft® Windows.

The individual components have been discussed in the previous Paragraphs, but for future experiments –in case the stepper motor torque is insufficient– it should be noted that the Microstep driver and stepper motor can be connected to a power supply with more eclectic potential than 12V.

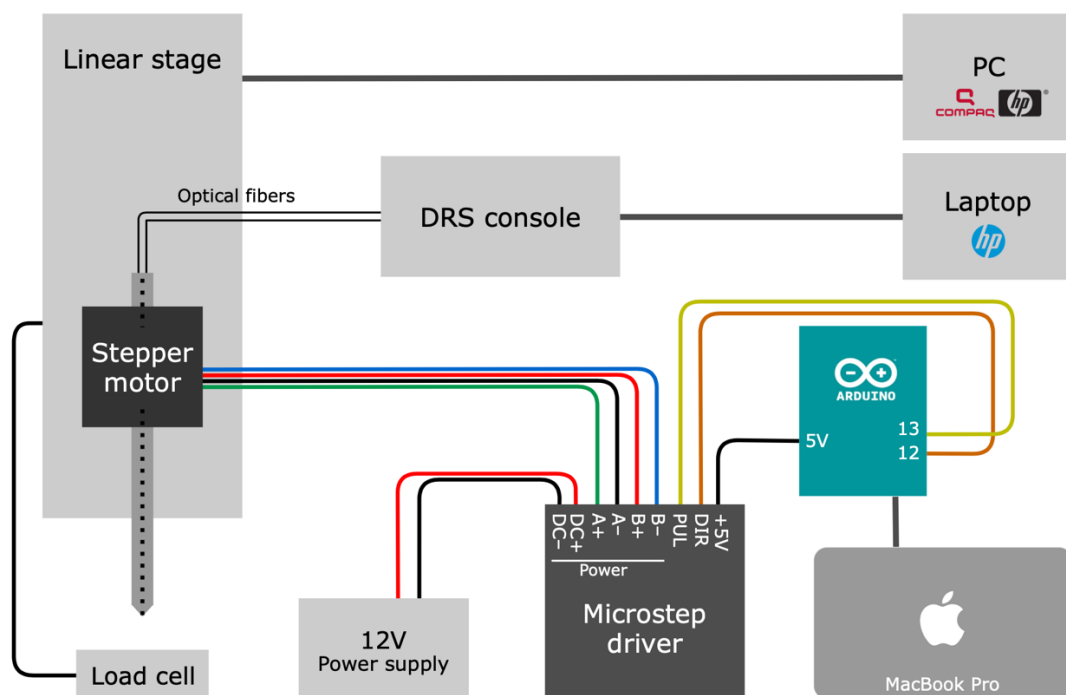


Figure 19. The measurement components and electrical circuit of the drill

## 2.3. Bone phantom tissue

The two experiments (optical and mechanical) elaborated in Section 2.1., make use of different bone phantom tissues. They both consist of a cancellous and a cortical bone layer.

### 2.3.1. Optical bone phantom

The optical bone phantom has been prepared on a basis of gelatin and agar. The fatty cancellous bone phantom is made by adding a 0,5L 20% intralipid emulsion for infusion (purified soybean oil) and to a gelatin solution of 60 grams in 200mL water, resulting in a fat fraction of approximately 13%. Intralipid has been used in several studies as a means of light absorbing and imitating fat in tissue [73] [74]. The cortical bone phantom tissue, which contains no fat, consists of an agar solution of 15 grams 255mL water with 13 grams of barium sulphate, added for its scattering properties.

#### Phantom tissue boundary deformity

As agar jelly features a higher modulus of elasticity ( $\text{N/mm}^2$ ) than gelatin jelly -

which gives it a firmer or stiffer texture—it offers the possibility to minimize deformity of the tissue boundary, as shown in *Fig. 21* [75]. This way, a delayed tissue boundary identification indicates an optical overshoot instead of an accurate optical detection of a deformed phantom tissue boundary.

In preparational experiments, when a drill entered a gelatin phantom, the surface showed the development of a minor (1-2mm) temporary dent. A tissue boundary within a gelatin phantom, can be deformed in a similar manner—as the gelatin (along with the drill) presses on top of the optical phantom tissue boundary.

Experiments with a boundary between a gelatin-based and an agar-based tissue boundary however, showed no visibly observable deformities. The gelatin jelly phantom (due to its lower elasticity modulus) compressed toward the sides into the other gelatin jelly, rather than downward onto the stiffer agar jelly, keeping the optical bone phantom boundary in place.

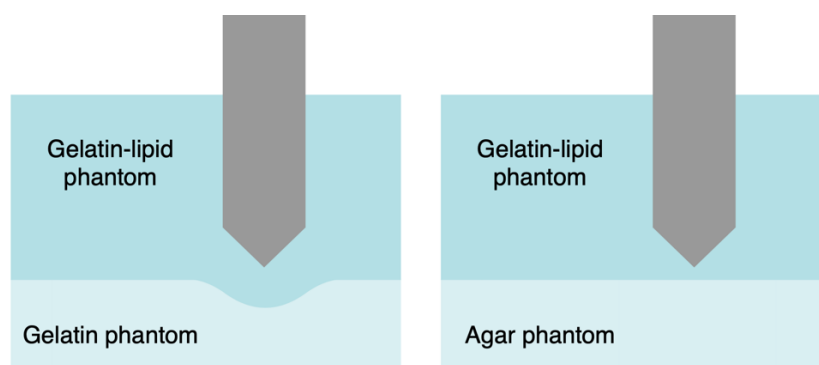


Figure 20. Bone phantom tissue boundary drilling deformity reduction

### 2.3.2. Mechanical bone phantom

The mechanical phantom features the combination of a Sawbones® 15 PCF cellular foam block of 40mm thick, shown in *Fig. 22.* as cancellous bone phantom and short fiber filled epoxy of 3mm thick as mechanical bone phantom. Compared to other foam blocks in the biomechanical product line, the 15 PCF block features relatively large cavities, resulting in a relatively inconsistent mechanical structure [76].

Sawbones® biomechanical materials have specifically been engineered for the purpose of the imitation of mechanical bone properties. The products are common in orthopaedic research [76] [77] [78].

It should be noted that Sawbones® products do not perfectly resemble genuine fresh cadaveric bone material, but since that cannot be used in the

available research facility –the Delft University of Technology MISIT Lab– Sawbones® materials provide the opportunity to test on materials highly similar to those of normal human adult bones [79] [80]. Furthermore, it allows for experiments that can be compared to hundreds of studies that use Sawbones® as well.

Labels (of the ingredients) and pictures of both the optical and the mechanical bone phantoms can be found in Appendix 7.2.3.

### 2.3.3. Benchmark phantom

As a benchmark, to see whether unexpected phenomena in both the optical and the mechanical experiment take place in another phantom as well, a block of young Dutch 48+ cheese is used with a fat fraction of 31%. The label of the cheese can be found in Appendix 7.2.3.



*Figure 21.* A Sawbones® 15 PCF cellular foam block with a thickness of 40mm

## 2.4. Statistical analyses

This Section discusses the analysis of the data acquired during the experiments discussed in Section 2.1.

### 2.4.1. Optical data processing

In the optical experiment, five feed rates are used, namely 0,5mm/s, 1mm/s, 1,5mm/s, 2mm/s and 2,5mm/s. The different feed rates feature five repetitions, resulting in the drilling of a total of 25 holes in the optical bone tissue phantom.

In every single drill cycle, DRS measurements are made and these are translated into a fat fraction. The discrepancy (in mm) between the known location of the phantom tissue boundary and the optical detection of the boundary is analysed. The threshold for the optical boundary detection is chosen at a fat fraction of  $\leq 6,5\%$ . This would, as the optical cancellous bone phantom has a fat fraction of approximately 13%, indicate a drop of at least half of the fat fraction.

The overshoots, or discrepancies between the physical boundary and the optically detected boundary of the phantom tissue, are identified. The

highest feed rate that features no positive overshoot is then established. This feed rate is regarded as the current 'speed limit' of the developed drilling setup.

### 2.4.2. Mechanical data processing

The mechanical experiment consists of using three drill types, namely a regular 2,7mmØ orthopaedic drill, a 1,35mmØ cannulated 2,7mmØ orthopaedic drill with a 1,25mmØ K-wire and a 1,7mmØ cannulated 2,7mmØ orthopaedic drill with a 1,6mmØ K-wire. The feed rates are varied; speeds of 1mm/s, 2mm/s, 3mm/s and 4mm/s are used. Axial drilling forces are measured and the experiments are repeated three times, resulting in a total of 36 drilling cycles.

An ANCOVA tests reveals the presence and significance of the mechanical implications of varying the drill types and the feed rates. This provides an insight into whether the forces that occur during stagnant probe-equipped drill penetration are comparable to axial forces in the current orthopaedic procedures.

# 3. Results

Increasing the drilling feed rate under a constant sampling frequency creates larger distances between the optical measurements. At a feed rate of 0,5mm/s, the DRS-drill detects the phantom tissue boundary before breaching it. Feed rates between 1mm/s and 2,5mm/s optically identify the boundary at a range of locations from 2,1mm before to 3,2mm after the boundary.

The mechanical experiment shows that increasing the feed rate increases the axial drilling forces. Introducing a stagnant probe into the drill increases the axial forces as well –especially in the epoxy mechanical cortical bone phantom, as none of the K-wire equipped drills can penetrate it. When using a regular 2,7mmØ orthopaedic drill on the cancellous bone phantom, the overall measured peak force is 38,2N. Using the 2,7mmØ drill with a 1,6mmØ K-wire, gives a peak force of 57,6N. In a drilling experiment on cheese, the introduction of a K-wire increases the required drilling forces by a factor 3 on average, but among the different feed rates and drill types it varies between 16% and 575%.



This chapter presents the results of the experiments described in Section 2.1.

Section 3.1. shows the results of the optical experiment and Section 3.2. presents the results of the mechanical experiment.

## 3.1. Optical experiment

The optical experiment consists of tissue identification through periodically taken DRS-spectra, translated into a fat fraction. First, individual spectra are observed, then the continuous fat fractions are shown as a signal. The last part of this Section is dedicated to the comparison of different fat fraction signals for varying the feed rates applied in this experiment.

### 3.1.1. Sampling frequency

Using the equipment described in Section 2.2., the minimal VIS integration time of 0,006s and a NIR integration time of 0,1s results in a sampling frequency of approximately 1,2Hz; a mean of 1,20Hz with an SD of 0,02.

In previous trial experiments, a NIR integration time of less than 0,1s resulted in a low signal intensity and signal to

noise ratio (SNR). This affected the spectral fitting and the tissue boundary identification capabilities to such an extent, that no relationship could be identified between the drilling feed rate and the overshoot.

With the 0,006 VIS integration time of and a NIR integration time of 0,1s, the inactive period  $t_{inactive}$  is approximately 0,7s, according to Equation 7. As the inactive period is more or less constant, the extent to which the sampling frequency is affected by reducing the NIR integration time decreases as the integration time decreases. This can be seen in Table 2.

Measuring tissue at a certain (1,2Hz) frequency means there are gaps between tissue identification measurements. The length of these gaps, or the distance (mm) between two optical measurements, depends on the drilling feed rate, as shown in Table 3.

NIR $t_{integration}$ (s)	VIS $t_{integration}$ (s)	$F_s$ (Hz)
0,5	0,006	1,0
0,1	0,006	1,2
0,02	0,006	1,5
0,01	0,006	1,5

Table 2. Sampling frequencies under varying integration times

$F_s$ (Hz)	Feed rate (mm/s)	Distance (mm)
1,2	0,5	0,41
1,2	1,0	0,83
1,2	1,5	1,25
1,2	2,0	1,67
1,2	2,5	2,08

Table 3. Sampling distances under varying feed rate

### 3.1.2. Individual spectra

Typical spectra of the optical bone phantom can be seen in Fig. 23: on the left, a DRS-shot from the lipid-based optical cancellous bone phantom and on the right, a shot from the optical cortical bone phantom made of agar and barium sulphate.

#### Lipid-based cancellous bone phantom

The DRS-derived fat fraction within the water and lipid content ( $f_{\text{lipid}/(\text{water}+\text{lipid})}$ ) of the shots taken in the lipid-based phantom during the 25 drilling cycles, averages at 25,4%, with an SD of 5,1 (%).

This is an overestimation of the actual fat fraction, which is approximately 13%. In a benchmark experiment on cheese with a 31% fat fraction the fat fraction within the water and lipid content averages at 50,5%. In contrast to the experimental methods discussed in Paragraph 2.2.5., fat fraction within the water and lipid content ( $f_{\text{lipid}/(\text{water}+\text{lipid})}$ ) is not multiplied by the DRS-derived fraction of water and lipid ( $f_{\text{water}+\text{lipid}}$ ). As the latter often passed 100%, it causes an even further overestimated fat fraction.

Because this overestimation of the fat fraction takes place in the agar layer as well (see next page), it can be concluded that it is a structural overestimation.

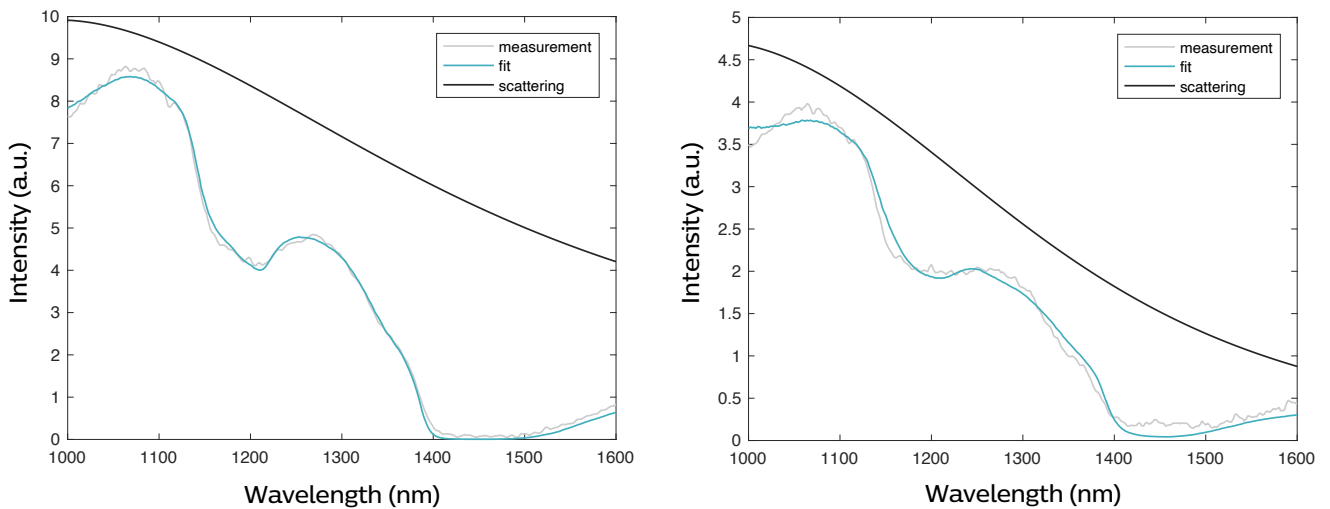


Figure 22. Spectra of lipid bone phantom (left) and the agar bone phantom (right)

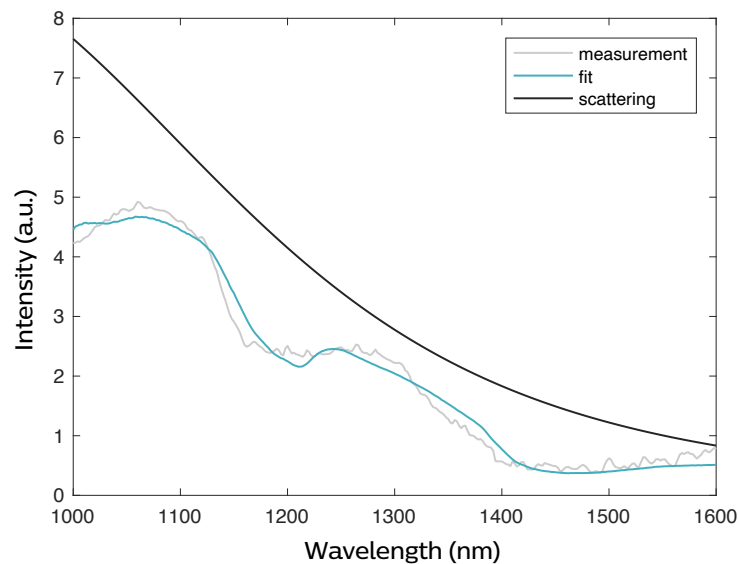


Figure 23. A spectrum of agar phantom resulting in an inaccurate fat fraction identification

### Agar-based cortical bone phantom

While the lipid-based phantom predominantly shows consistent spectra and fat fractions, the DRS-derived fat fraction in agar phantom varies widely between 0% and 84%. *Fig. 24* shows an example of a spectrum taken in agar that resulted in an inaccurate optical fat fraction estimation ( $f_{lipid/(water+lipid)}$ ) of 78,1%. The characteristic optical dip of lipids around 1200nm (as shown in the lipid bone phantom spectrum in *Fig. 23*) can be seen in the fit function, but not in the measurements. The scattering curve, which is inverted in *Fig. 24*, also differs from the typical scattering in the agar bone phantom in *Fig. 23*. In such cases, the fittings lead to inaccurate fat fraction identifications of up to 84%. As a result, the average fat fraction of all the spectra taken in the agar phantom is 19% with an SD of 23%.

Drilling cycles at varying feed rates contained either (almost) none, or many spectra that feature the abovementioned inaccurate fit and

inverted scattering. These spectra can be eliminated from the data as inaccurate measurements, resulting in an average fat fraction is 9,6%, with an SD of 11,0%. In the agar phantom a total of 301 spectra were taken, and the removal of the inverted scattering spectra results in discarding 70 (23,3%) of the measurements, or 5 of the 25 drilling cycles.

### 3.1.3. Tissue boundary detection

The fat fractions, derived from periodically taken DRS shots, create a signal that changes based on the location of the drill tip. This Paragraph examines the DRS drill's ability to detect the optical phantom tissue boundary.

Similar to a surgeon approaching a cortical bone layer from cancellous bone tissue, the DRS drill travels through the lipid-based optical cancellous bone phantom, towards the agar-based optical cortical bone.

Fig. 25 shows the fat fraction ( $f_{\text{lipid}/(\text{water}+\text{lipid})}$ ) measured in five drilling cycles at a feed rate of 0,5mm/s. The removed measurements, discussed in the previous Paragraph (3.1.2.) are shown in grey. While the used and the removed signals largely overlap in the lipid-based phantom, they show considerable difference in the agar-based phantom. The plots similar to Fig. 25 of all other

feed rates can be found in Appendix 7.3.1.

### Tissue boundary detection

Fig. 26 shows the fat fraction measurements at feed rates at 0,5mm/s and 2,5mm/s, excluding the removed drilling cycles. The resolution of the signal of the 2,5mm/s feed rate is visibly lower.

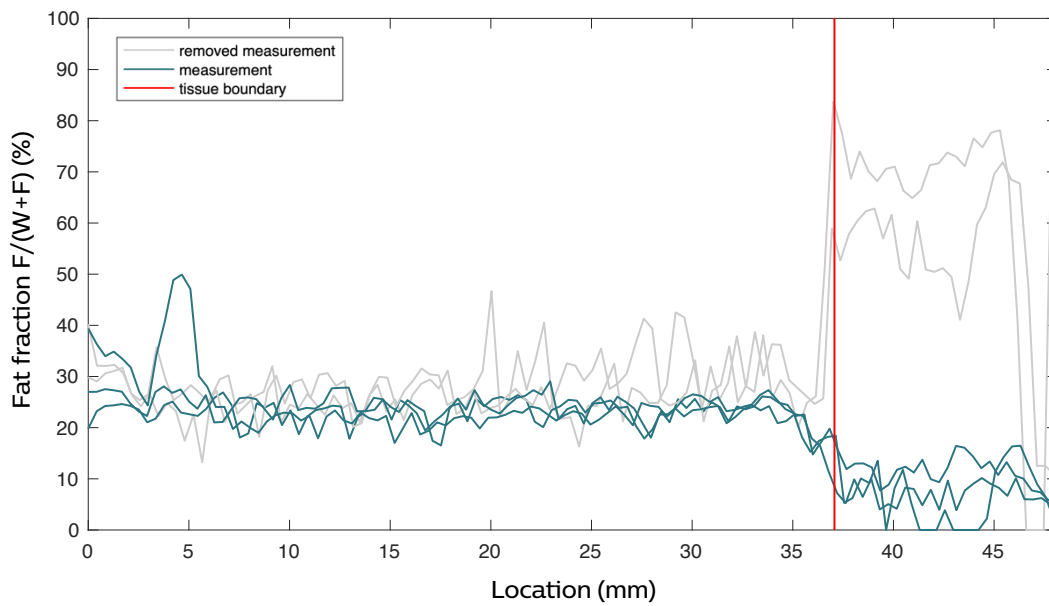


Figure 24. Fat fractions versus location at a 0,5mm/s feed rate

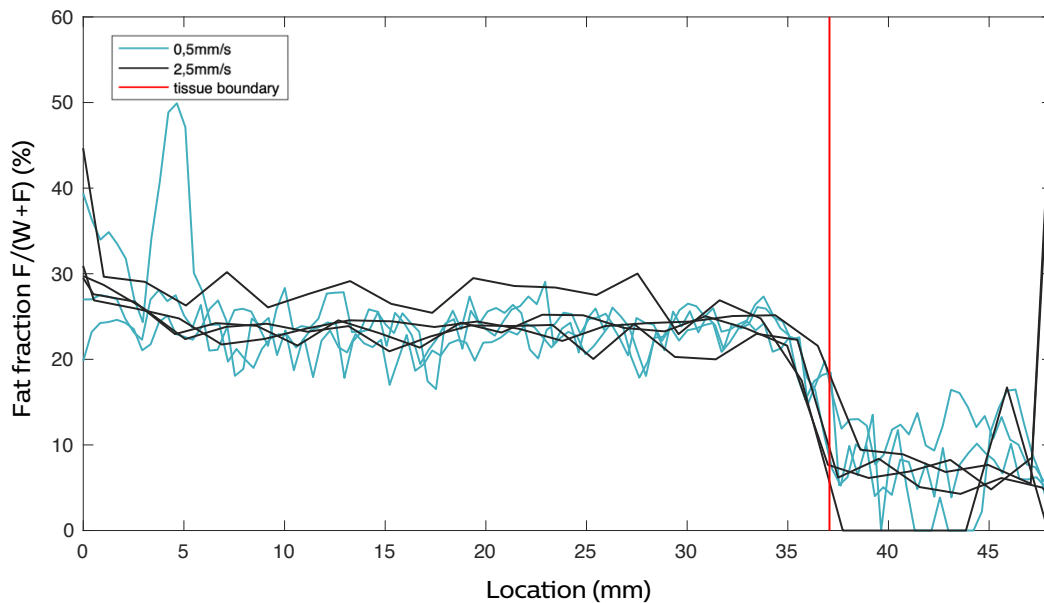


Figure 25. Fat fractions versus location at feed rates of 0,5mm/s and 2,5mm/s

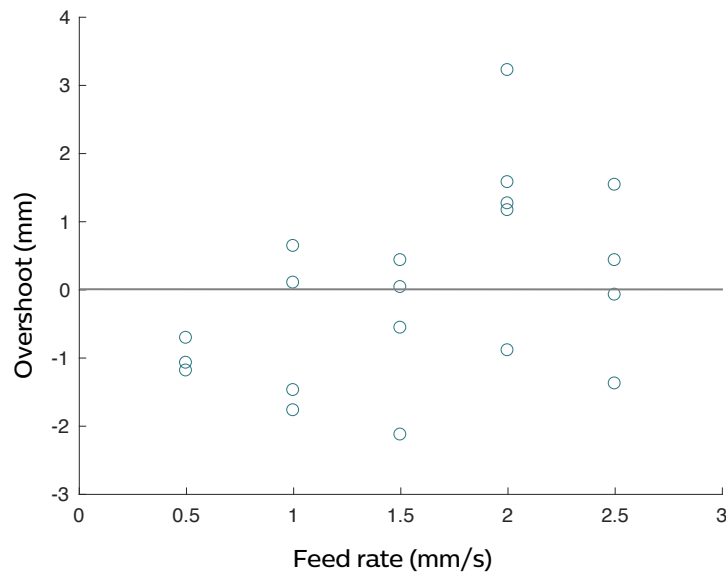


Figure 26. Scatterplot of the feed rate and overshoot of the DRS drilling setup

	0,5mm/s	1mm/s	1,5mm/s	2mm/s	2,5mm/s
overshoot	9,5*	0,6	-2,1	-0,9	-1,3
(mm)	-1,1	10,9*	0,3	1,2	0,8*
	10,1*	-1,4	0,4	3,2	0,4
	-0,7	-1,8	3,1*	1,6	-0,1
	-1,2	0,1	-0,5	1,2	1,5

\*removed measurement

Table 4. Drilling overshoots at varying feed rates

As discussed in Paragraph 3.1.2., the fat fraction of the lipid phantom is overestimated by the applied fitting model. Therefore, the fat fraction threshold values for a tissue stated in Section 2.4. is not applicable to the received data. Since the average fat fraction is 25,4% in the lipid-phantom and 9,6% in the agar layer, the threshold is chosen at 17,5% –again, indicating a drop of at least half of the change in fat fraction.

Table 4 shows the distances from the phantom tissue boundary at which the first fat fraction measurement of  $\leq 17,5\%$  is taken, for all the individual drilling cycles.

The data from Table 4 is shown in Fig. 27. Only at a feed rate of 0,5mm/s does the drill optically detects the boundary before breaching it, which has been chosen as a requirement for safe drilling in Paragraph 1.2.1. As the feed rate increases, the spread of overshoots increases, which corresponds to the larger distance between the optical measurements, as shown in Table 3.

## 3.2. Mechanical experiment

The mechanical experiment studies the axial drilling forces of three drill types, measured with a load cell with a sampling frequency of 5000Hz ( $T_s=0,0002s$ ). The measurements in one individual drilling cycle are shown, after which forces are compared between different feed rates and drill types.

### 3.2.1. Axial drilling forces

The axial forces of a drilling cycle of a regular 2,7mmØ orthopaedic drill in Sawbones® at 2mm/s are shown in Fig. 28. When applying a 2mm/s feed rate for instance, instead of having a constant speed, the stepper motor of the linear stage takes microsteps at 0,83mm/s, 1,67mm/s and 2,5mm/s, that combine into a 2mm/s average overall feed rate.

The microsteps affect the measured axial forces, as a higher feed rate requires a higher feed force (see Paragraph 1.1.2.). The caused peaks and dips can be seen in the raw measurements (in grey) in Fig. 28. These can also be found in benchmark drilling cycles in cheese, confirming that they are indeed caused by properties of the experimental setup and not by the use of Sawbones® materials. A force diagram of a cheese drilling cycle can be found in Appendix 7.3.2.

With the intention of improving the visualization of the data, it is averaged over adjacent frequencies twice –in the case of Fig. 28 at phase shift of  $\tau = 21$  and  $\tau = 13$ . The phase shift varies per measurement, as the different feed rates show varying periods between the micro peak force measurements. The statistical analysis in this Section uses the raw axial drilling force measurements, but the diagrams feature averaged signals.

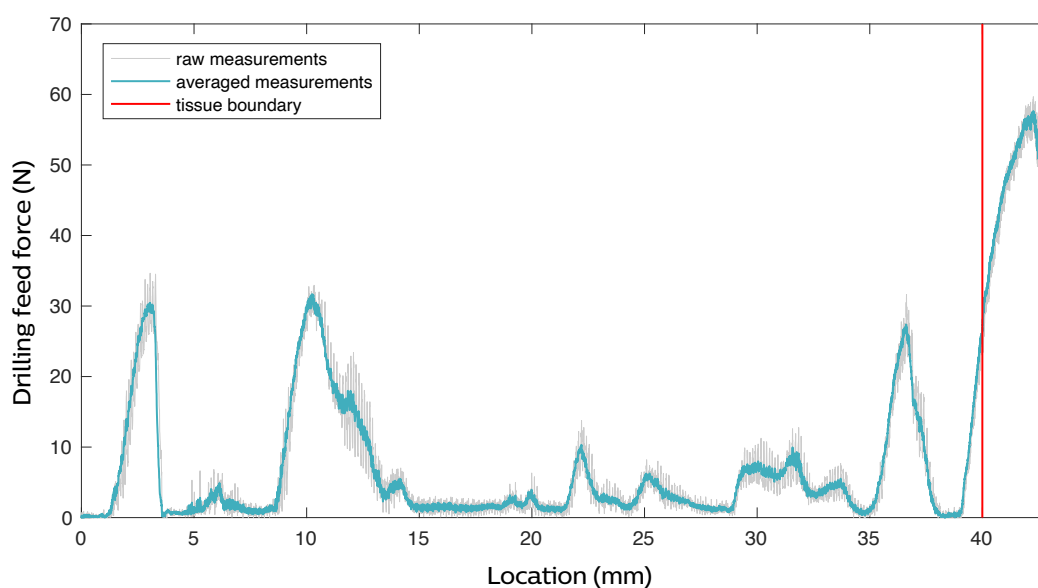


Figure 27. Axial drilling forces of a 2,7mmØ orthopaedic drill in Sawbones® phantom, 2mm/s

As can be seen in *Fig. 28*, the axial forces in the Sawbones® 40mm thick foam block (left) show peaks of approximately 10N and 30N. In the epoxy phantom (right), the forces go up to 60N.

The peaks observed in the foam layer of the Sawbones® phantom can be explained by the properties of the foam. *Fig. 29* shows a schematic view the physical structure of the 15 PCF foam, the glue layer, and the fiber filled epoxy. While traveling through the foam, the drill encounters material clumps and cavities. When the drill encounters a

minor or major clump of material, the axial drilling forces show the peaks that are found in *Fig. 28*. In the benchmark drilling in cheese, which features a constant physical structure, such peaks cannot be found. The glue layer explains why the forces tend to increase before the epoxy layer is reached.

Since the mechanical properties of real bone are more constant than those of the used phantom foam, the drilling cycles –which have been repeated three times– are averaged, as shown in *Fig. 30* [57] [81].

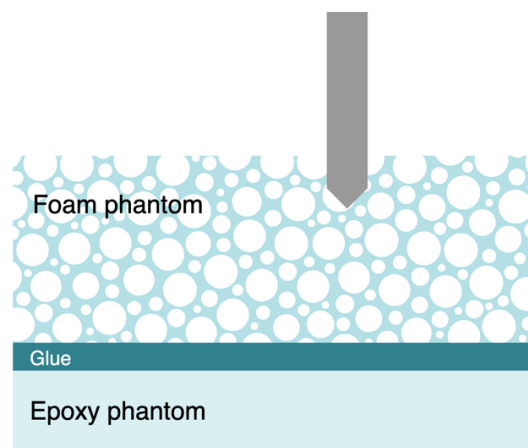


Figure 28. The physical structure of the mechanical Sawbones® phantom

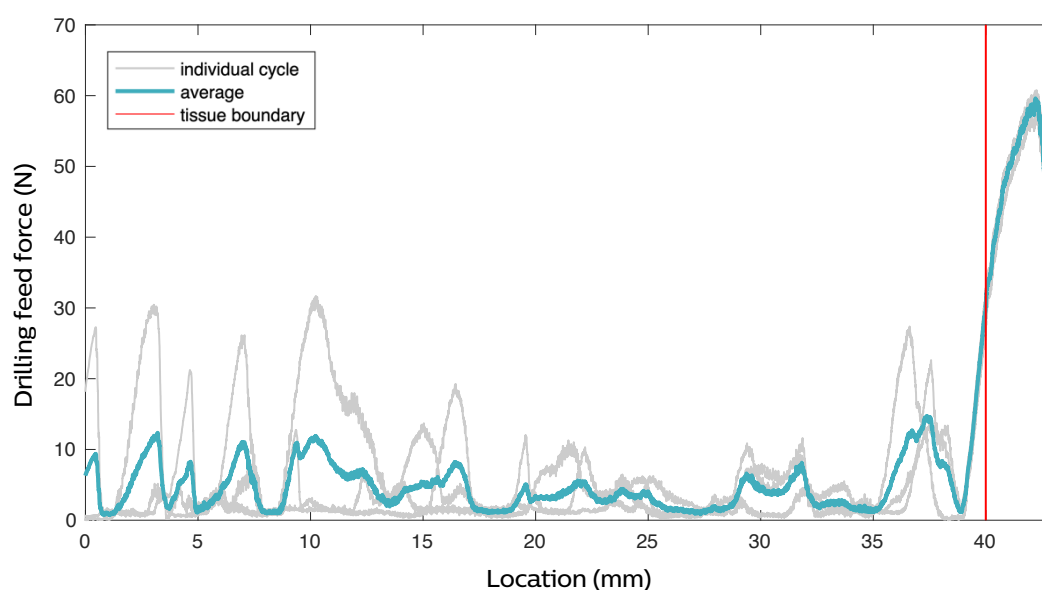


Figure 29. Single and average force measurements of a 2,7mmØ drill in Sawbones® at 2mm/s



The effect of varying the drilling feed rate is shown in *Fig. 31*. Increasing the feed rate increases the (peak) feed forces – which is especially clear in the epoxy cortical bone phantom.

*Fig. 32* shows the effect of varying the drill type. The cannulated drills equipped with K-wires show higher peaks in the

foam phantom, but a more striking difference occurs in the epoxy phantom, as none of the K-wire equipped drills got through the material. The linear stage halted at an axial force of approximately 80N, instead of drilling through the material and decelerating between 42mm and 43mm.

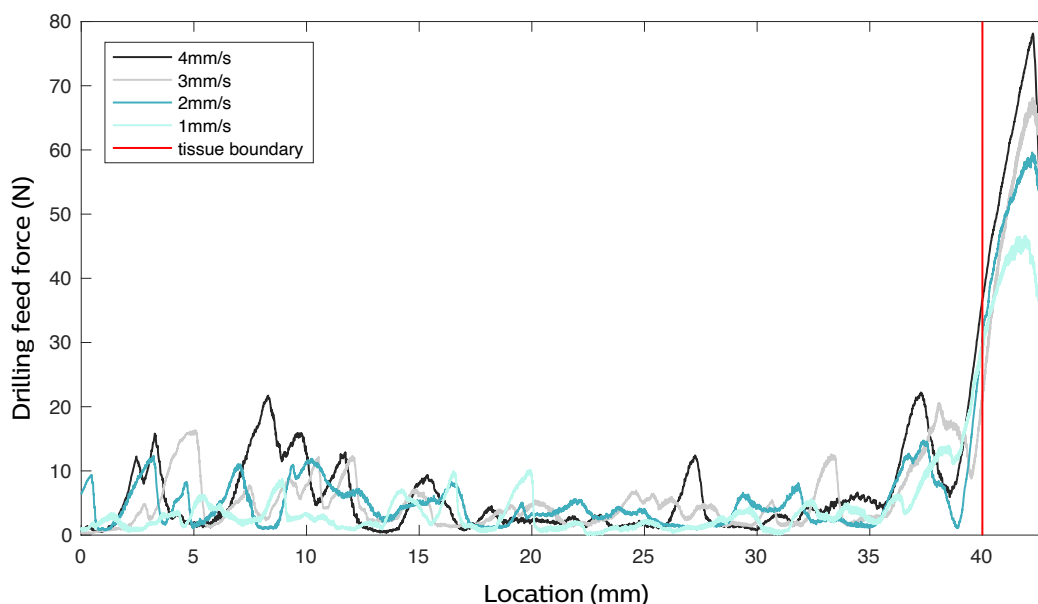


Figure 30. Average force measurements of a 2,7mmØ drill in Sawbones® at varying feed rates

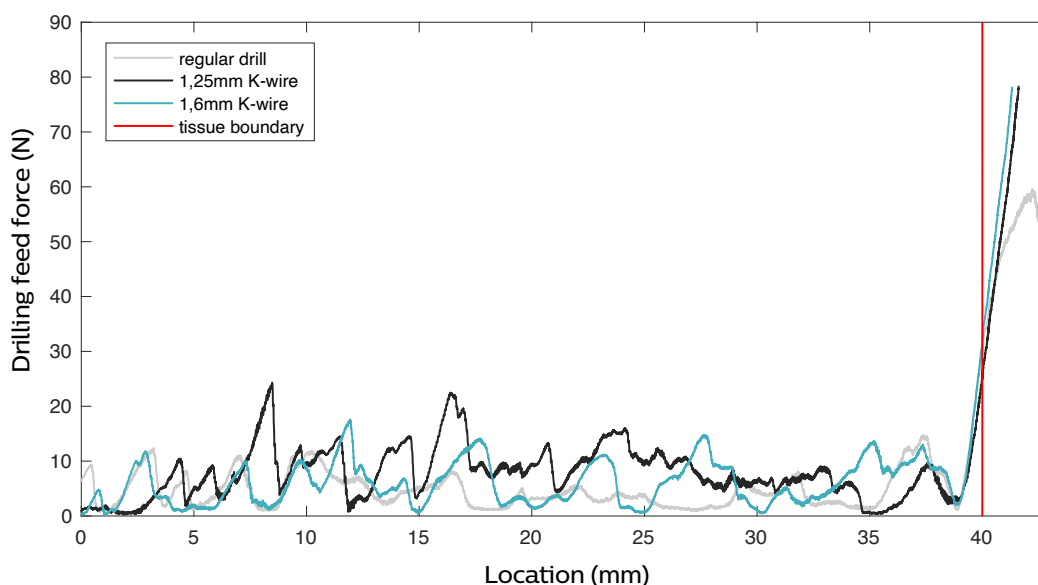


Figure 31. Average axial drilling forces of three drill types in Sawbones® phantom at 2mm/s

The comparison of axial drilling forces can be separated into two analyses: one on the epoxy cortical bone phantom and one on the 15 PCF foam cancellous bone phantom.

### Cortical bone phantom

When comparing different drill types, drilling in the epoxy cortical bone phantom shows binary differences; the K-wire equipped drills do not penetrate through the material –as they require more axial forces than the linear stage can offer– while regular drills do drill all the way through. The approximate 1,5mm epoxy penetration which can be seen in *Fig. 32*, is assumed to be overstated. (This will be elaborated in discussion Paragraph 5.1.2.) Therefore, it is assumed that there is hardly any data from the K-wires in the epoxy layer.

Due to a lack of data in the epoxy cortical bone phantom, no statistical analysis is performed, but it can be concluded that clear differences are present. All of the regular 2.7mm orthopaedic drills penetrate all the way through the epoxy, while none of the K-wire equipped cannulated drills do so.

### Cancellous bone phantom

In the 15 PCF foam cancellous bone phantom, data of all the 36 drilling cycles can be compared based on feed rate and drill type. Means and SD per group can be found in *Table 5*. Introducing a stagnant K-wire increases the axial drilling forces by 55% on average compared to a regular drill, but the increase varies among the different K-wires and feed rates from 30% to 219%. It should be noted that the distribution of the forces is skewed, so the significance of the abovementioned force increases has not been determined.

Drill type Feed rate (mm/s)	2,7mmØ regular drill		1,25mmØ K-wire equipped drill		1,6mmØ K-wire equipped drill	
	Mean (N)	SD	Mean (N)	SD	Mean (N)	SD
1	3,61	5,56	7,91	10,67	5,02	8,19
2	4,90	6,29	8,13	8,61	6,35	8,26
3	5,23	7,40	7,74	10,23	7,55	9,61
4	5,61	7,42	7,84	9,95	8,83	11,43

*Table 5.* Axial forces of different drills and feed rates in Sawbones® foam phantom

An example of the skewed distribution of the force measurements can be seen in *Fig. 33*. It shows measurements taken at a feed rate of 2mm/s, while using a regular 2,7mmØ orthopaedic drill and a 1,7mmØ cannulated 2,7mmØ orthopaedic drill with a 1,6mmØ K-wire. The peak forces measured in the two drilling cycles in *Fig. 33* are 31,14N and 45,25N respectively. The skewness causes the force measurements to be unsuited for statistical analyses that

presume the data is normally distributed. Data transformations such as a Log transformation, have not corrected the data in such a way that a normal distribution can be assumed.

A benchmark experiment on cheese instead of the Sawbones® foam has been carried out too. Drilling in cheese does provide normally distributed measurements, as shown in *Fig. 34*.

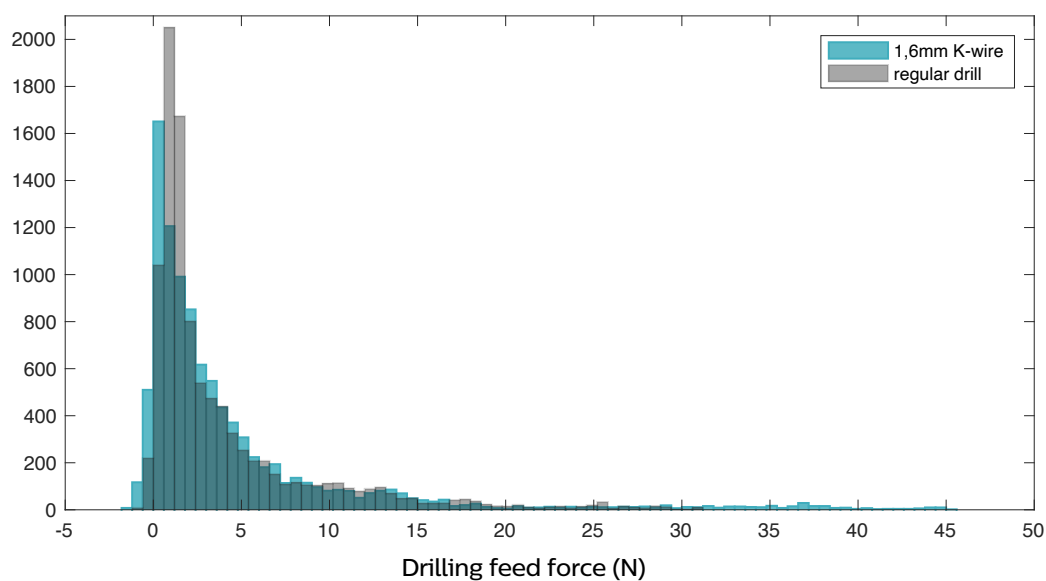


Figure 32. Histograms of axial forces in Sawbones® cellular foam phantom at 2mm/s

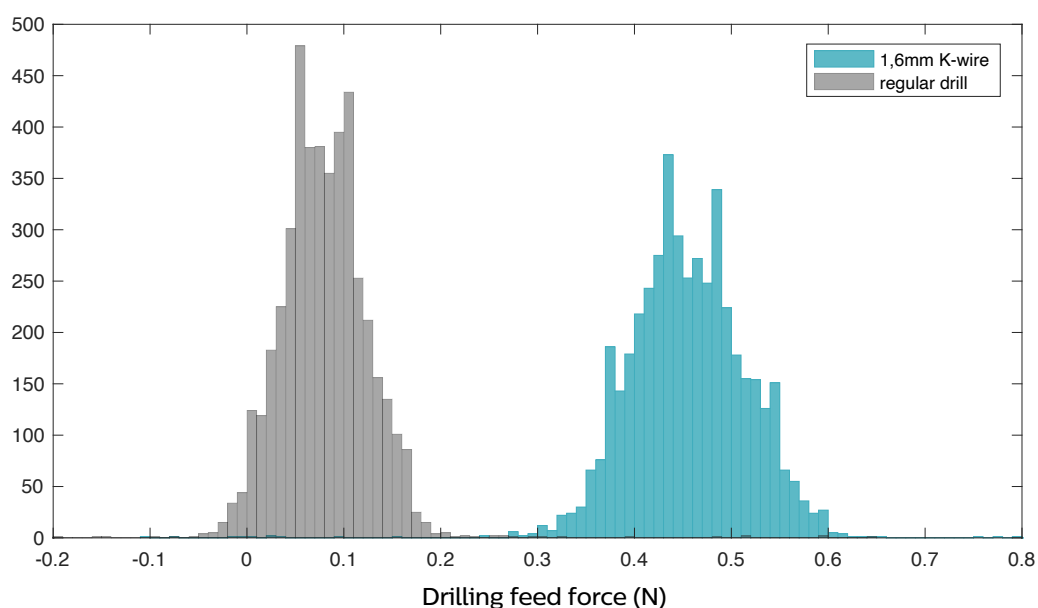


Figure 33. Histograms of axial forces in cheese at 2mm/s

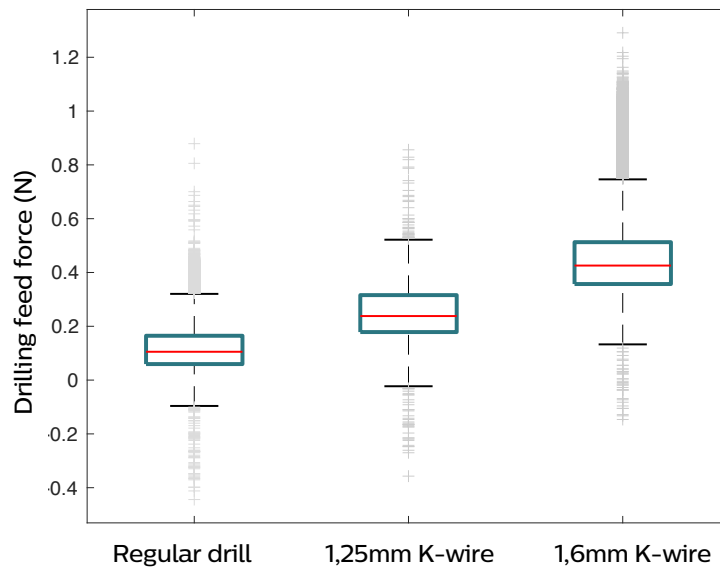


Figure 34. Boxplot of axial forces on varying drill types in cheese

Fig. 35 shows boxplots of different drill types: a regular 2,7mmØ orthopaedic drill, a 1,35mmØ cannulated 2,7mmØ orthopaedic drill with a 1,25mmØ K-wire and a 1,7mmØ cannulated 2,7mmØ orthopaedic drill with a 1,6mmØ K-wire. Table 6 shows the means and SD of the cheese drilling force measurements. On average, the introduction of a K-wire increases the required drilling forces by a 296% (roughly a factor 3).

Among the different feed rates and drill types, the force increase varies between 16% and 575%. Table 7 shows that the feed rate and the drill type both cause the axial drilling forces to differ significantly. The covariate by outcome interaction (Feed rate\*drill type) is significant as well, which means that the assumption of homogeneity of the regression slopes is broken; the slopes of the different feed rates are not similar [86].

Drill type Feed rate (mm/s)	2,7mmØ regular drill		1,25mmØ K-wire equipped drill		1,6mmØ K-wire equipped drill	
	Mean (N)	SD	Mean (N)	SD	Mean (N)	SD
1	0,09	0,06	0,18	0,06	0,37	0,07
2	0,08	0,05	0,23	0,08	0,46	0,06
3	0,17	0,06	0,30	0,09	0,54	0,07
4	0,31	0,07	0,36	0,08	0,88	0,11

Table 6. Axial forces of different drills and feed rates in cheese

Source	d.f.	Sum Sq	Mean Sq	F	Sig.
Feed rate	3	617,19	205,73	30990,92	.000
Drill type	1	1478,9	1478,9	222780,1	.000
Feed rate*drill type	3	88,45	29,48	4441,32	.000
Error	69487	461,28	0,01		

Table 7. ANCOVA tests of between subject effects

### 3.2.2. Rotational speed

Based on the literature review written prior to conducting this research, a relatively low rotational speed of 500rpm is used, as a low rotational speed limits the heat development due to friction (see Paragraph 1.1.2.). Increasing the rotational speed however, can be of interest for further experiments.

A brief examination shows that the stepper motor-powered DRS drill can reach an 1800rpm (6000 pulse per

second) rotational speed while rotating in the air. When receiving more pulses per second, the rotational speed became inconsistent.

In both the in the Sawbones® foam, as well as in the cheese phantom a rotational speed of 1000rpm proved workable; the drill got through the Sawbones® foam without problems and the DRS measurements in the cheese were similar to those measured while using a 500rpm rotational speed. Furthermore, no noteworthy temperature increase of the drill bit or optical probe has been noticed when manually examining these parts.

## 4. Discussion

The inaccurate fat fraction measurements are, but they are not expected to occur in human tissue. The sampling frequency of the optical system need to be increased in order to make the DRS drill timely detect tissue boundaries at higher feed rates.

Suggestions for follow-up research include DRS-tissue identification while drilling at an angle, testing on cadaveric bone, and eventually, clinical trials.

Noteworthy DRS drill concepts are discussed, as well as possible users of the instrument. The potential users are not only neurosurgeons, but also general orthopedic surgeons and dentists.

This chapter discusses the results, follow-up research, concepts for DRS drill concepts and possible DRS drill users.

Section 4.1. discusses the performance of the DRS drill in both the optical and mechanical test. Section 4.2. briefly suggests opportunities to improve the

optical measurements, and causes to conduct more experiments with the DRS drill. Section 4.3. discusses follow-up research and Section 4.4. suggests points of attention for further DRS drill concept development. Lastly, in Section 4.5., possible users, as well as potential secondary benefits of a DRS drill are discussed.

## 4.1. DRS drill performance

The quality of the used bone phantom is an essential part of this research, as it is intended to resemble real bone as much as possible. The shortcomings of both the optical and the mechanical bone phantom are discussed in this Section.

### 4.1.1. Optical bone phantom

As mentioned in Paragraph 3.1.2., the fat fractions are consistently overestimated. Furthermore, the fat fraction identifications in the agar-based optical cortical bone phantom show inaccurate measurements in five (23%) of the drilling cycles.

Whether these phenomena are of importance for the further development of a DRS drill, is based on two criteria:

1. It affects general tissue boundary identification abilities.
2. It is observed in human tissue as well.

#### Fat fraction overestimation

Because the fat fraction overestimation is consistent (affecting both the fat and the non-fat phantom tissue), it has a limited effect on the DRS drill's ability to detect a tissue boundary. Only the threshold value for the tissue boundary needed adjustment, as discussed in Paragraph 3.1.3. The consistency of the overestimation can also be observed in *Fig. 23* and *Fig. 24*, as the dip in the fit function at approximately 1200nm is lower than the actual optical

measurements in all the spectra. Several studies using the same equipment on real bone however, do not report this structural overestimation [63] [64] [65].

The fitting and fat fraction identifications are the result of a model that is initially generated for biological tissues. The model fits and identifies the fat fraction based on specific assumptions –such as the assumption that the mean free path is smaller than the fiber distance– and by comparing the measured spectrum to spectra of specifically selected chromophores that appear in human tissue.

One can speculate about the effects of the assumptions and the included references in regard to the used phantom, but this is regarded beyond the scope of this thesis. This is a research on applying DRS tissue identification to drilling equipment, not on adjusting the DRS identification technique to artificial phantom tissue.

To still provide some background information on this however, the following brief examples show how used references of the model can influence the resulting fat fraction identification.

The applied model takes the chromophores of fat, water, deoxygenated-hemoglobin (Hb), oxygenated- hemoglobin (HbO<sub>2</sub>) and collagen into account. Collagen is a structural animal protein that can be found in the human body, and also in – as they are both animal products– cheese and gelatin. Gelatin is also



referred to a hydrolysed collagen [83]. Similar to fat, a collagen absorption spectrum features a peak (or a reflection dip) at 1200nm [86].

When excluding the reference to collagen from the model, the scattering changes and reflection dip in the fit at 1200nm becomes even larger, as can be seen in *Fig. 36*, taken in the gelatin lipid phantom. The fat fraction overestimation is subsequently increased by approximately 10% (from 41,3% to 51,0%). This effect occurs in the agar phantom layer as well.

Changing the fat fraction ( $f_{\text{lipid}/(\text{water}+\text{lipid})}$ ) scaling factor in the model from 100 to 50, results a similar fit function, but the resulting fat fraction is divided by two. Apart from not improving the resemblance between the fit and the measurement function, this handling also features the downside that the identification of a substance of 100% (pure) fat will also be scaled to 50%.

Although the discussed fitting issues are not resolved by the abovementioned changes to the model, the examples are illustrative for the way the assumptions of the used model affect the fat fraction identifications shown in this thesis.

### Excluded drilling cycles

The optical fit-based fat fractions in the agar phantom that contained no fat, occasionally went up to values of 50% to 80%, as shown in *Fig. 25*. *Fig. 23* shows an example of a spectrum that resulted in fat fraction measurement of 78,1%. The fit projects the characteristic dip of a lipid spectrum at 1200nm on a measured function that does not feature such a dip. These measurements only occurred in the agar-based optical bone phantom, not in the gelatin lipid-phantom or in the cheese.

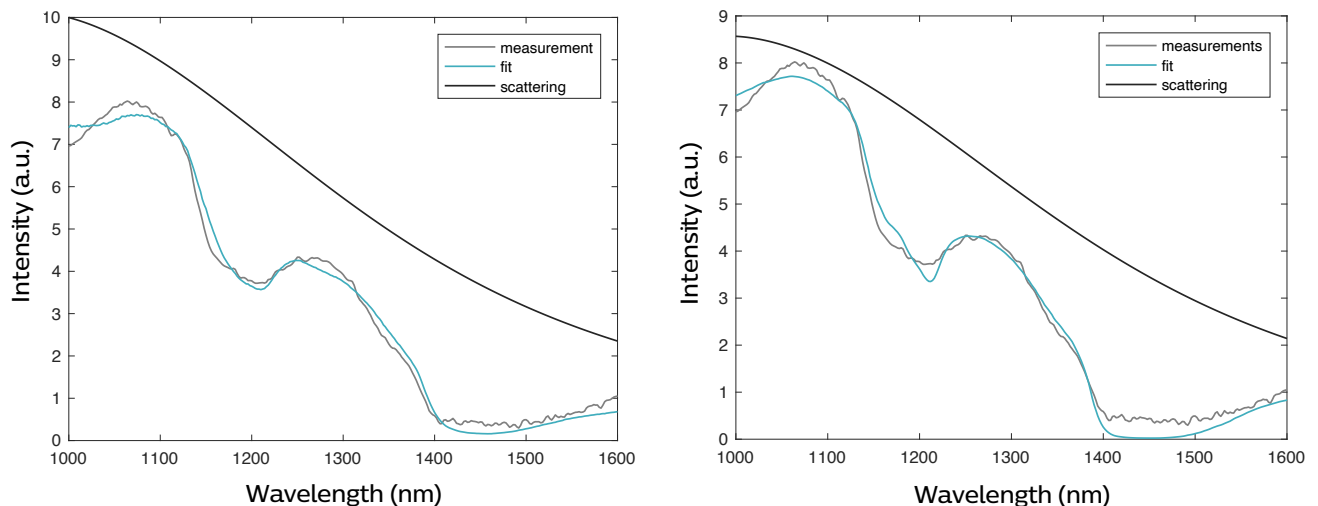


Figure 35. Spectra and fit functions with (left) and without (right) taking collagen into account

Because they compromised the tissue detection abilities of the DRS drill (the fat fraction threshold value is not reached), the measurements have been excluded from the comparison of the feed rate and the drill overshoot in Paragraph 3.1.3.

Similar to the structural fat fraction overestimation, these highly inaccurate tissue identifications are not mentioned in several studies using the same equipment on real bone [63] [64] [65]. Therefore, it is assumed that they are a result of that the used spectral data modelling –which is developed for biological tissue identification– is not perfectly suited for the used artificial phantom.

If this phenomenon occurs in real bone tissue as well, it is of interest for the development of a DRS drill to eliminate it, through optimization of the fitting model.

#### **4.1.2. Mechanical bone phantom**

The different drill types show different behaviour in the cortical and the cancellous bone phantom layer.

##### **Cancellous bone phantom**

The skewed data in the cancellous bone phantom, of which an example is shown in *Fig. 33*, causes the measurements to be unsuited for statistical analyses that assume a normal distribution. This skewness is not found in studies on drilling in real bone [41] [57]. Nonetheless, the (peak) values of the force measurements do provide insights in the

height of the forces that can be expected while drilling in bone. When using a regular 2,7mmØ orthopaedic drill on the cancellous bone phantom, the measured peak force is 38,2N. Using the 2,7mmØ orthopaedic drill with a 1,6mmØ K-wire, a peak of 57,6N is observed. Both peaks are found in drilling cycles with a feed rate of 4mm/s.

The axial drilling forces measured while using the 2,7mmØ orthopaedic drill in the Sawbones® phantom are relatively high compared to forces found in studies on cadaveric bone drilling. In the epoxy cortical bone phantom layer, forces vary between approximately 40N and 80N, while several studies on cadaveric cortical bone report drilling force values between 20N and 40N [21]. Studies by Duperron *et al.* and Tahmasbi *et al.* however, show consistent values of approximately 100N in cortical bone [41] [57]. It can therefore be concluded that the axial drilling forces in the Sawbones® bone phantom, although it is a relatively hard material, fall within the range of forces found in the literature research written prior to conducting this research [21].

##### **K-wires in cortical phantom**

The linear stage halted when the axial forces approached 80N. Based on the linear stage specifications however (see Paragraph 2.2.3.), it was expected that a feed force of approximately 180N could be produced.

In *Fig. 32*, it can be seen that the K-wire equipped drills travel into the epoxy for approximately 1,5mm, but during the occurrence of the sudden force increase it has been visibly noted that the linear

stage compressed the entire drilling setup. Therefore, it is assumed that the covered distance in the epoxy, shown in *Fig. 32*, does not represent penetration of the cortical bone phantom, but rather the compression of the hinge with the load cell and the lab jack it is placed upon.

Based on these experiments, it can be argued that the stagnant probe-equipped drills have a flawless mechanical system of stopping at a cortical bone tissue boundary. It should however be noted that the Sawbones® epoxy cortical bone phantom is relatively hard (as previously mentioned in this Paragraph) and thick, compared to the cortical thickness of the cervical pedicle. These can be as thin as 0,90mm on average, as discussed in Paragraph

1.1.1. Thus, a probe equipped drill can possibly still drill through cortical bone in the human body.

Being able to penetrate cortical bone with a DRS drill can be beneficial, as a surgeon would then be able to use a drilling instrument with one (sensing) drill bit during the entire surgery, instead of alternating between a reamers, drills and probes as is currently the case in SSP [21]. Materials that feature a closer mechanical resemblance to human bone than Sawbones® are needed to verify whether stagnant probe equipped drills can penetrate cortical bone. As stated above, this could improve the clinical applicability of a probe equipped orthopaedic drill. For this reason, experimenting on cadaveric bone is advised.

## 4.2. Optical measurement improvements

As discussed in the previous Section, the drill performance in the optical experiment is influenced by the extent to which the optical bone phantom resembles biological tissue. In order to better study the performance of the drill, (cadaveric) bone drilling is advised.

Apart from improving the optical properties of a bone phantom, the DRS device itself can be improved as well. This Section focuses on ways to enhance the optical tissue boundary identification abilities of the drill.

### 4.2.1. Sampling time

The sampling time has proven to be essential to the DRS drill's ability to identify tissue boundaries, as discussed in Section 3.1. A larger the sampling time, causes the larger gaps between two optical measurements, and thus, a larger chance that a tissue boundary is overlooked in the meantime. The current maximum feed rate of 0,5mm/s should be increased to 5mm/s, as that is the maximum feed rate observed in the OR (see Appendix 7.11. Visited surgery notes).

The sampling time, described in *Equation 7* in Paragraph 2.2.5., consists of the integration time  $t_{integration}$ , and an inactive period  $t_{inactive}$ . In this experiment, the sampling frequency, as discussed in Section 3.1., is approximately 1,2Hz. This frequency is a result of an integration, and an inactive period of approximately 0,1s and 0,65s respectively.

The expected 5Hz sampling frequency, mentioned in Paragraph 1.4.1., has not been reached, due to the fact that the inactive period could not be decreased in the DRS console that has been used. Because the integration time has been reduced to 0,1s, it represents only approximately 12% of the sampling time. Therefore, it is recommended to first focus on investigating possibilities to decrease the 0,7s inactive period  $t_{inactive}$ .

In the optical test results, the overshoots as the feed rate increases, seem to be the result of a larger spread of the measurements as shown in *Table 3*. When using a feed rate above 0,5mm/s, the larger distances between the measurements cause drilling overshoots. In order to have similar distances between optical measurements at 5mm/s (a factor 10 faster), the sampling frequency of 1,2Hz would have to be multiplied by a factor 10, to approximately 12Hz. The corresponding sampling time is 0,083s. This frequency cannot be obtained by only eliminating the inactive period, so the used NIR integration time  $t_{integration}$  of 0,1s needs to be reduced as well.

A structural delay due to drill travelling during, as mentioned in the hypothesis in *Equation 4*, has not been identified, but it could be that this starts playing a more significant role at higher feed rates; at 5mm/s the drill covers a 0,5mm distance during the integration time of 0,1s, while the distance is only 0,05mm at a 0,5mm/s feed rate. Minimizing the integration time  $t_{integration}$  would reduce this effect too.

### 4.2.2. Signal intensity

Apart from reducing the sampling time, the signal quality can be improved as well. This does not only provide an opportunity to decrease the sampling time. Improving the signal intensity also leads to a higher SNR in the individual spectra, resulting in more accurate fat fraction identifications, like the removal of the fiber splitter did, as discussed in Paragraph 2.2.5.

A way of improving the measured light intensity, is by increasing the optical fiber diameter. This can be explained with a quantity called etendue.

Etendue is a geometric light quantity described as the product of the area of a light source and its solid angle [89]. In a perfect optical system, shown in *Fig. 37*, etendue is preserved, which means that a light bundle projects an image that either has a larger area and a smaller angle, or a smaller area with a larger angle –the product remains constant.

In the optical experiment of this research, as light penetrates the tissue, the etendue is ‘spread out’. As the experimental test setup is not a perfect optical system, light is scattered and absorbed. However, in a simplified manner, the DRS collecting fiber can be seen as an etendue collecting surface with the same area as the light source, placed on the projection area of *Fig. 37*.

*Fig. 37* shows a system where the projection is a result of a light transmission of 100%. If the lens (or tissue) scatters the light however, part of it will be reflected back to the light source. Thus, if the collecting fiber is placed next to the light source, it captures the diffuse reflection.

When using an optical reflection collecting fiber with a larger diameter, more of the etendue can be captured, as it covers a larger section of the projection area. When using a light emitting fiber with a larger diameter as well, the area of the light source increases, releasing more etendue too.

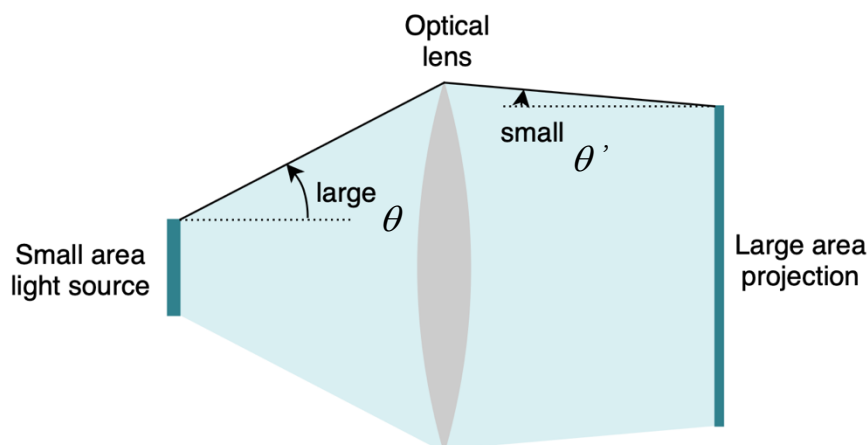


Figure 36. The preservation of etendue in a perfect optical system

### 4.2.3. More measurements

More measurements are needed to gain more detail about the DRS drill's optical performance described in this thesis.

#### Feed rate speed limit

The experiment shows that the feed rates that show no overshoot are below 1mm/s. In this area, data is collected through five drilling cycles, of which two have been discarded due to inaccurate measurements, discussed in Section 3.1. More measurements in the feed rate range below 1mm/s are required to add certainty to the resulting maximum feed rate.

Furthermore, using more feed rates within this range, can possibly show that the maximum feed rate is above 0,5mm/s (but below 1mm/s). This would affect the extent to which the sampling time should be decreased.

#### LAD

When using a low feed rate such as 0,05mm/s, the LAD of this drilling system can be established. As the LAD depends on several factors including the optical properties of the tissue (as mentioned in Paragraph 1.2.1.) it is of interest to establish the LAD of this drilling system not only in optical phantoms, but also in real bone tissue [58].

## 4.3. Follow up research

This Section briefly discusses the next steps in research, required to further develop a DRS drill, suited for cervical SSP.

### 4.3.1. Drilling at an angle

This research used a drilling setup to approach a phantom tissue boundary perpendicular to the drilling direction. During SSP however, tissue boundaries of pedicles are usually approached at an angle, as shown in *Fig. 38*. As the right half of the drill tip is still in the cancellous bone, the left half is at risk of beaching the cortical bone. Research on DRS drilling at an angle can support finding the required calibration for tissue boundary identification.

### 4.3.2. Cadaveric testing

This experiment uses phantom tissues, which feature the upside of having sudden tissue boundaries of which the location can be known precisely. Phantoms have the downside however, that they do not possess the actual optical and mechanical properties of real bone.

The mechanical properties of real bone are of interest to see whether a handheld stagnant probe-equipped drill can be used to penetrate bone. If it handles in a similar way as a regular bone drill, a surgeon can safely

experiment with the instrument, as it only provides extra feedback, without reducing any.

The optical properties of real bone are important to conduct DRS drilling experiments on as well. The cancellous to cortical bone boundaries are organically shaped and they are more gradual than the bone phantom. Furthermore, the DRS fat fraction identification can be done in a shorter time when based on a limited number of wavelengths, instead of the entire spectrum from 1000nm to 1600nm. The selection of these wavelengths should be based on drilling experiments in real bone.

### 4.3.3. Clinical trials

In the last stage of the DRS drill development, clinical trials should take place in order to quantify the actual intended effect that the system is supposed to have: a reduction in spinal screw misplacements.

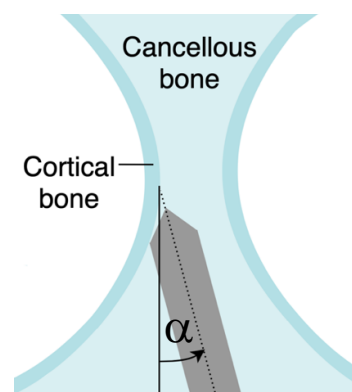


Figure 37. Approaching a cortical bone boundary at angle  $\alpha$  in a pedicle

## 4.4. DRS drill concept development

This Section specifies desired properties of an optical probe for drilling and it briefly discusses two DRS drill concepts, that can be of interest for the further development of the instrument.

### 4.4.1. DRS drilling probe

Although drilling with a stagnant probe causes considerable axial force increases and the K-wire equipped drills have not been able to penetrate the Sawbones® epoxy cortical bone phantom, it could still be possible that a probe-equipped drill is applicable in the OR, as discussed in Paragraph 4.1.2. The used optical probe shown in *Fig. 18*, is not customized for orthopaedic drilling however, so this Paragraph discusses possible adjustments to the probe to improve its orthopaedic applicability.

#### Probe diameter

The results of Paragraph 3.2.1. show that a larger probe diameter increases the required axial drilling forces, while surgeons prefer to keep the axial drilling force low, as discussed in Paragraph 1.4.2. So, if choosing to develop a stagnant optical probe-equipped drill, it is of interest to keep the probe diameter limited. In the used fitting model however, a certain optical fiber distance is required; part of the diffuse approximation assumed by the model, is that the free path length of a photon is small compared to the fiber distance.

A study by Li, Liu and Quan on porcine bone drilling however, shows their ability to optically detect tissue changes while using no fiber distance (200 $\mu$ m-diameter fibers are arranged in parallel at a core-to-core distance of 200 $\mu$ m), so this distance can be very small [90].

#### Probe tip angle

As discussed in Paragraph 2.2.4., an optical probe needs a sharp tip to be suited for orthopaedic applications. The optical fibers would then have to be angled, to be flush with the sharp, angled tip. Studies show angles as small as 20 degrees with respect to the needle axis for DRS tissue identification [91]. Such an angle makes a sharp tip, but it possibly causes challenges too: (when using a certain fiber distance), the distance between the fiber surface and the probe tip increases when the tip angle  $\beta$  decreases, as shown in *Fig. 39*. This could compromise (part of) the drill's ability to detect a tissue boundary before breaching it. The variables of *Fig. 39* need to be optimized with regard to the optical performance and the required axial drilling forces.

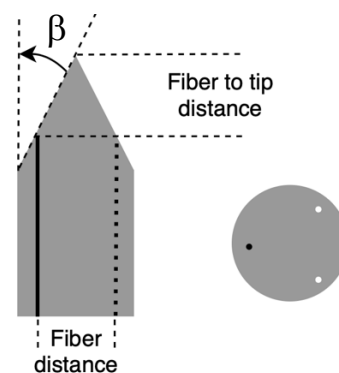


Figure 38. Probe tip variables and a cross section of a possible probe design



It could furthermore be possible that the optical signal intensity is relatively low if the light collecting fiber lies in 'in the shadow' of the probe tip. If this proves problematic, a design with two light emitting probes, shown as white fibers in the cross section of the probe in *Fig. 39*, could possibly offer a solution.

#### 4.4.2. One fiber

If the DRS concept with a stagnant probe features insurmountable mechanical consequences, rotating fibers have to be reconsidered, although the coupling of rotating fibers to a light source and a reflection detector remains challenging. The use of one single centred rotating fiber, connected to a stagnant fiber through a sapphire ball lens, shown on the left of *Fig. 40*, features a relatively simple fiber coupling mechanism.

The concept uses one fiber that is both the light emitting and the reflection collecting fiber. The reflected light in this single fiber however, contains relatively less of the optical properties of the tissue than a separated reflection collecting fiber does, as the reflected light travels through the tissue for at least the fiber distance.

The concept could work, if the spectral fitting can be done without a fiber distance. As the previously mentioned study by Li, Liu and Qian used no fiber distance, so testing a one-fiber concept could be promising [90].

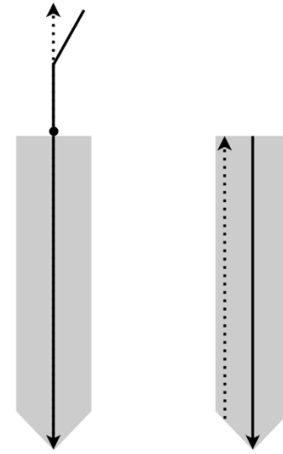


Figure 39. The one-fiber (left) and the directional feedback (right) DRS drill concepts

#### 4.4.3. Directional feedback

One of the surgeons interviewed during this research asked if a DRS drill could provide information about in which direction a bone boundary is located – a question worth considering.

When combining a rotating reflection collecting fiber with a centred light emitting fiber, shown on the right of *Fig. 40*, the drill could potentially identify minor periodic differences in the fat fraction, that coincide with the rotational speed of the drill. If the spectrum integration is fast enough to be performed several times in a limited amount of drill rotations, and if the optical signal differences are large enough, the drill could connect the periodical peak in the 'fat fraction function' to the rotational orientation of the drill, indicating the direction of the cortical bone.

When looking at the sampling frequency and the SD of the fat fractions in this experiment however, we are not close to providing directional feedback.

## 4.5. Applicability of a DRS drill

This project started off as a research to improve SSP, but among the way, surgeons other than neurosurgeons showed interest in the DRS drill as well. This Section briefly discusses possible users of the drill and issues they raised.

### 4.5.1. DRS drill users

Neurosurgeons have shown interest in this project from the start, allowing surgery visits and expressing the issues they encounter while performing surgery. Notes of the surgeon visits and interviews can be found in Appendix 7.1.1.

The most pressing problems for surgeons included navigational difficulties, but the use of fluoroscopy during the surgical procedures caused frustration too. First of all, taking fluoroscopic shots takes time, especially if –in the case of the scoliosis surgery– more than 50 shots have to be taken. Secondly, the surgical team is exposed to harmful radiation while wearing uncomfortable protective gear [92].

One neurosurgeon –although jokingly– mentioned that finally, a (this) research provides an opportunity to discard all the “annoying” protective gear that surgeons wear throughout the surgery. Although the complete elimination of fluoroscopic shots is not near, nor has it been a specific object of this research, the comment can be interpreted as a genuine frustration, that a DRS drill could partly solve.

General orthopaedic surgeons explained they could use a sensing drill as well. ‘Shooting through’ the bone is a problem that every orthopaedic surgeon mentioned. They developed personal, non-standardized ways of navigational support, based on sound and vibrations. Based on the subjectivity of some of these approaches, there seems to be a demand for technical support.

Dentists could possibly use a DRS drill as well. When dentists use an orthopaedic drill for the placement of dental implants and grafts, they are at risk of damaging the alveolar and the lingual nerve [83]. The alveolar nerve is shown in *Fig. 41*. Although these nerves are not surrounded by a DRS-detectible cortical bone layer like the spinal cord, their diameters of 2,6mm are be large enough to be detected by a DRS drill [94]. A study by Hendriks *et al.* also shows promising results on DRS nerve detection for anaesthesia through needle injection close to nerves [95].

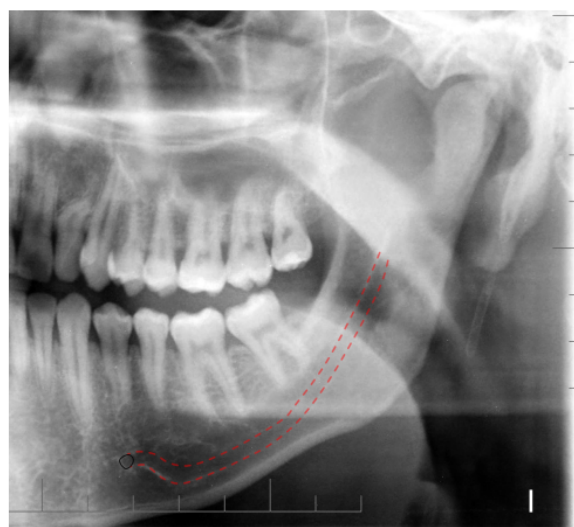


Figure 40. A fluoroscopic image of a jaw with the alveolar nerve marked in red [85]

#### 4.5.2. Thermal osteonecrosis

Thermal osteonecrosis, as discussed in Paragraph 1.1.2., is the irreversible death of bone cells (osteocytes) due to heat. It can result in a longer recovery period and orthopaedic screw loosening [37].

If technical navigational support such as a DRS drill proves a better alternative to current procedures, it could possibly be used to drill more accurately, but also at a higher feed rate. An interviewed surgeon mentioned he has to drill very carefully, due to a lack of feedback (see Appendix 7.1.1.). Since limiting the drilling time has the largest effect on tissue temperature rises of the variables discussed in Paragraph 1.1.2., using a DRS drill could indirectly mitigate thermal osteonecrosis [46] [47].

#### 4.5.3. Osteoporosis

One of the interviewed surgeons asked whether a DRS drill would be able to identify bone affected by osteoporosis. If so, a surgeon could adjust pressing forces (axial feed forces) on the drill to the relatively soft bone structure. Therefore, it is of interest to investigate if healthy and osteoporotic bone can be differentiated through DRS.

#### 4.5.4. User interaction design

The study on DRS bone drilling by Duperron *et al.* concerns the development of an automated drill stop [57]. It remains to be seen however, whether a forced automated stop would be the best way of integrating DRS tissue identification into drilling instruments. The system could result in false positive tissue boundary identification, stopping the drill when in fact, no tissue boundary is present. Furthermore, the DRS system would have to be turned off if the drill is used for drilling in cortical bone. This can cause frustration among the users.

Instead of dictating a drill stop, a DRS drill could also be used to guide the surgeon. This central issue in the user interaction design concerns whether the DRS drill can autonomously ‘decide’ to stop, or whether it supports a surgeon in such decision making. If a surgeon supporting system is chosen, more research is required into which way of feedback communication is most desirable for a DRS drill.

# 5. Conclusions

The DRS drilling feed rate speed limit based on this experiment is 0,5mm/s.

In the Sawbones® 15 PCF cellular foam mechanical cancellous bone phantom, the drills show forces up to 60N. Introducing stagnant K-wires into the drill in a benchmark drilling experiment on cheese increased the drilling forces by approximately a factor 3. None of K-wire equipped drills have been able to penetrate the epoxy cortical bone phantom.

This chapter briefly discusses the initial research questions and their conclusions. Section 5.1. concludes the optical experiment and Section 5.2. concludes the mechanical experiment.

## 5.1. Optical experiment

In the optical experiment, the drilling feed rate of the DRS-drill has been varied to study the effect it has on the instrument's ability to timely detect a tissue boundary.

The research question of this experiment is described in Section 1.4. as:

What is the maximum feed rate at which the DRS fiber-equipped drilling instrument can be used to ensure no tissue boundary breach takes place when the drill approaches a cancellous to cortical bone tissue boundary?

### 5.1.1. Feed rate speed limit

The identified speed rate limit is 0,5mm/s. As previously mentioned in the in Paragraph 3.1.3. and the discussion Sections 4.1. and 4.2. More drilling cycles can be done to further specify this maximum speed rate.

### Sampling time

The hypothesis formulated in Section 1.4. assumes an integration time  $t_{integration}$  of 0,2s and a negligible inactive period  $t_{inactive}$ . The opposite is the case: the integration time is reduced to 0,1s in this experiment, while the inactive period of approximately 0,7s –reaching a sampling frequency of approximately 1,2Hz. Therefore, the ability of the DRS drill to accurately detect tissue boundaries is more influenced by the distances between the DRS measurements than by the distance covered during the DRS integration time.

## 5.2. Mechanical experiment

In the mechanical experiment the drill types and feed rates have been varied to study their effect on the axial drilling forces –the force a surgeon needs to exert on the drill, in order to penetrate bone.

The research question of this experiment is described in Section 1.4. as:

What is the difference in axial drilling forces, required to penetrate cancellous and cortical bone tissue, between a drill with a centred stagnant probe and regular bone drill?

### 5.2.1. Axial drilling force increases

The hypothesis in Section 1.4. predicted a 54% axial force increase, based on the reduced machining surface of a cannulated drill.

An analysis of the axial forces in cancellous and cortical bone phantom showed, first of all, that –in contrast to regular orthopaedic drills, none of the probe-equipped drills have been able to penetrate the epoxy cortical bone phantom. It can be concluded that there is a difference in required axial forces between regular and probe-equipped drills in the epoxy cortical bone phantom, as the probe-equipped drills consistently required more forces than the linear stage could provide.

The effect size of this phenomenon cannot be determined due to a lack of data in the epoxy layer; it is unknown how high the required axial forces of the K-wire-equipped drills would have risen (see *Fig. 32*) if the linear stage provided a higher pressing force.

Due to the inconsistent structure of the Sawbones® 15 PCF foam cancellous bone phantom, the retrieved data is unsuited for statistical analyses that assume a normal distribution. As discussed in Paragraph 4.1.2., the range of the forces does fall within values seen in other bone drilling studies. While using a regular 2,7mmØ orthopaedic drill on the cancellous bone phantom, the measured peak force is 38,2N. Using the 2,7mmØ orthopaedic drill with a 1,6mmØ K-wire, a peak of 57,6N is observed.

A drilling experiment in cheese did produce normally distributed force measurements and significant differences between the drill types. On average, the introduction of a K-wire increases the required axial drilling force by 296% (roughly a factor 3). However, among the different feed rates and drill types, the force increase varies between 16% and 575%. Experiments on (cadaveric) bone are recommended to verify the clinical applicability of a probe equipped drill in both cancellous and cortical bone.

## 6. References



- [1] S. Irvine, "The Daily Beast," [Online]. Available: [https://img.thedailybeast.com/image/upload/c\\_crop,d\\_placeholder\\_euli9k,h\\_1439,w\\_2560,x\\_0,y\\_0/dpr\\_2.0/c\\_limit,w\\_740/fl\\_lossy,q\\_auto/v1492193970/articles/2014/11/03/patients-screwed-in-spine-surgery-scam/141102-cir-medical-scam-tease\\_mukxv0](https://img.thedailybeast.com/image/upload/c_crop,d_placeholder_euli9k,h_1439,w_2560,x_0,y_0/dpr_2.0/c_limit,w_740/fl_lossy,q_auto/v1492193970/articles/2014/11/03/patients-screwed-in-spine-surgery-scam/141102-cir-medical-scam-tease_mukxv0). [Accessed 1 2019].
- [2] Z. Pan, J. Zhong, S. Xie, L. Yu, C. Wu, Y. Ha, K. K. N., Z. Y. and K. Cao, "Accuracy and Safety of Lateral Vertebral Notch-Referred Technique Used in Subaxial Cervical Pedicle Screw Placement," *Operative Neurosurgery*, 2018.
- [3] E. J. Woo and M. N. DiCuccio, "Clinically significant pedicle screw malposition is an underestimated cause of radiculopathy," *The Spine Journal*, no. 18(7), pp. 1166-1171, 2018.
- [4] T. Yoshii, T. Hirai, K. Sakai, H. Inose, T. Kato and A. Okawa, "Cervical pedicle screw placement using intraoperative computed tomography imaging with a mobile scanner gantry," *European Spine Journal*, no. 25(6), pp. 1690-1697, 2016.
- [5] S. L. James, D. Abate, K. H. Abate, S. M. Abay, C. Abbafati, N. Abbasi and I. Abdollahpour, "Global, regional, and national incidence, prevalence, and years lived with disability for 354 diseases and injuries for 195 countries and territories, 1990–2017: a systematic analysis for the Global Burden of Disease Study 2017," no. 392(10159), pp. 1789-1858, 2018.
- [6] J. Hartvigsen, M. J. Hancock, A. Kongsted, Q. Louw, M. L. Ferreira, S. Genevay and R. J. Smeets, "What low back pain is and why we need to pay attention," *The Lancet*, no. 391(10137), pp. 2356-2367, 2018.
- [7] The Economist, "The burden of back pain," *The Economist*, no. Jan 18th, 2020.
- [8] M. Allaoui, F. Zairi, M. C. Tétard, J. Gaughan, D. Chopin and R. Assaker, "Contribution of Dynamic Surgical Guidance to the Accurate Placement of Pedicle Screws in Deformity Surgery: A Retrospective Case Series," *World Neurosurgery*, no. 120, pp. e466-e471, 2018.
- [9] N. E. Foster, J. R. Anema, D. Cherkin, R. Chou, S. P. Cohen, D. P. Gross and J. A. Turner, "Prevention and treatment of low back pain: evidence, challenges, and promising directions," *The Lancet*, vol. II, no. 391(10137), pp. 2368-2383, 2018.
- [10] W. m. member, "https://forums.mtbr.com," Dec 2005. [Online]. Available: <https://forums.mtbr.com/rider-down-injuries-recovery/I5-s1-spinal-fusion-fix-stenosis-1032599.html>. [Accessed Apr 2020].
- [11] E. Koktekir, Z. O. Toktas, A. Seker, A. Akakin, D. Konya and T. Kilic, "Anterior transpedicular screw fixation of cervical spine: is it safe? Morphological feasibility, technical properties, and accuracy of manual insertion," *Journal of Neurosurgery: Spine*, no. 22(6), pp. 596-604, 2015.
- [12] N. Shepard, H. Pham, V. Natarajan, T. Errico and M. Rieger, "Use of a Novel Computerized Drill for Pedicle Screw Insertion in the Thoracic and Lumbar Spine: A Cadaveric Study," *International journal of spine surgery*, no. 13(4), pp. 329-335, 2019.
- [13] Y. J. Kim, L. G. Lenke, G. Cheh and K. D. Riew, "Evaluation of pedicle screw placement in the deformed spine using intraoperative plain radiographs: a comparison with computerized tomography," *Spine*, no. 30(18), pp. 2084-2088, 2005.
- [14] Y. Hojo, M. Ito, K. Suda, I. Oda, H. Yoshimoto and K. Abumi, "A multicenter study on accuracy and complications of freehand placement of cervical pedicle screws under lateral fluoroscopy in different pathological conditions: CT-based evaluation of more than 1,000 screws," *European Spine Journal*, no. 23(10), pp. 2166-2174, 2014.
- [15] G. Calvosa, M. Tenucci, M. Galgani and S. Vallini, "In Modern Thoraco-Lumbar Implants for Spinal Fusion," in *Imaging in Lumbar Spine Surgery: The Role of Intraoperative CT Scan*, Springer, Cham., 2018, pp. (pp. 15-22).
- [16] MK medical GmbH & Co. KG, "KIRSCHNER WIRES / K-WIRES," [Online]. Available: <https://www.mk-medical.com/en/products/kirschner-wires/>. [Accessed Jul 2020].

- [17] KeeboMed, Inc, "Cannulated Drill Bit," 2020. [Online]. Available: <https://www.keebomed.com/products/cannulated-drill-bit?variant=12102636142718>. [Accessed Jul 2020].
- [18] © Judd Medical Limited, "K-wires," [Online]. Available: <https://judd-medical.co.uk/product/arthrodesis-wires-double-trocar/>. [Accessed Jul 2020].
- [19] C. A. Dickman, K. T. Foley, V. K. Sonntag and M. M. Smith, "Cannulated screws for odontoid screw fixation and atlantoaxial transarticular screw fixation," *Journal of neurosurgery*, no. 83(6), pp. 1095-1100, 1995.
- [20] Orthopromed Inc., "Orthopromed 1101 Mini Cannulated Bone Drill," 2020. [Online]. Available: <https://www.orthopromed.com/product/orthopromed-1101-mini-cannulated-bone-drill/>. [Accessed Jul 2020].
- [21] M. P. Kan, "Seeing the light: applying diffuse reflectance spectroscopy to surgical drilling instruments: a literature study on applying diffuse reflectance spectroscopy (DRS) to surgical drilling instruments to improve safety during spinal screw placement," Delft University of Technology, Delft, 2020.
- [22] L. Westermann, C. Spemes, E. P. M. Simons, M. J. Scheyerer, J. Siewe and D. Baschera, "Computer tomography-based morphometric analysis of the cervical spine pedicles C3–C7," *Acta neurochirurgica*, no. 160(4), pp. 863-871, 2018.
- [23] R. Gupta, K. Kapoor, A. Sharma, S. Kochhar and R. Garg, "Morphometry of typical cervical vertebrae on dry bones and CT scan and its implications in transpedicular screw placement surgery," *Surgical and Radiologic Anatomy*, no. 35(3), pp. 181-189, 2013.
- [24] A. Jea, K. K. Johnson, W. E. Whitehead and T. G. Luerissen, "Translaminar screw fixation in the subaxial pediatric cervical spine," *Journal of Neurosurgery: Pediatrics*, no. 2(6), pp. 386-390, 2008.
- [25] B. Lin, Y. Xu, Z. M. Guo, H. Liu, Z. W. Chen and M. C. He, "Feasibility of atlantoaxial pedicle screws' placement in children 6–8 years of age: a cadaveric and tomographic study," *Journal of Pediatric Orthopaedics B*, no. 22(5), pp. 399-403, 2013.
- [26] M. J. Geck, E. Truumees, D. Hawthorne, D. Singh, J. K. Stokes and A. Flynn, "Feasibility of rigid upper cervical instrumentation in children: tomographic analysis of children aged 2–6," *Clinical Spine Surgery*, no. 27(3), pp. E110-E117, 2014.
- [27] C. S. Vara and G. H. Thompson, "A cadaveric examination of pediatric cervical pedicle morphology," *Spine*, no. 31(10), pp. 1107-1112, 2006.
- [28] S. Lu, Y. Q. Xu, G. P. Chen, Y. Z. Zhang, D. Lu, Y. B. Chen and X. M. Xu, "Efficacy and accuracy of a novel rapid prototyping drill template for cervical pedicle screw placement," *Computer Aided Surgery*, no. 16(5), pp. 240-248, 2011.
- [29] X. Zheng, R. Chaudhari, C. Wu, A. A. Mehbod and E. E. Transfeldt, "Subaxial cervical pedicle screw insertion with newly defined entry point and trajectory: accuracy evaluation in cadavers," *European Spine Journal*, no. 19(1), pp. 105-112, 2010.
- [30] A. R. Patwardhan, P. S. Nemade, S. K. Bhosale and S. K. Srivastava, "Computed tomography-based morphometric analysis of cervical pedicles in Indian population: a pilot study to assess feasibility of transpedicular screw fixation," *Journal of postgraduate medicine*, no. 58(2), p. 119, 2012.
- [31] M. Moser, M. Farshad, N. A. Farshad-Amacker, M. Betz and J. M. Spirig, "Accuracy of patient-specific template-guided versus freehand cervical pedicle screw placement from C2–C7: a randomized cadaveric study," *World neurosurgery*, 2019.
- [32] M. M. M. Eldin, "Cervical pedicle screw fixation: anatomic feasibility of pedicle morphology and radiologic evaluation of the anatomical measurements," *Asian spine journal*, no. 8(3), p. 273, 2014.
- [33] V. K. Viswanathan, S. Subramanian and S. Viswanathan, "Comparison of Three Different Options for C7 Posterior Vertebral Anchor in the Indian Population—Lateral Mass, Pedicle, and Lamina: A Computed Tomography-Based Morphometric Analysis," *Asian Spine Journal*, no. 12(4), p. 726, 2018.
- [34] S. C. Ludwig, J. M. Kowalski, C. C. Edwards and J. G. Heller, "Cervical pedicle screws: comparative accuracy of two insertion techniques," *Spine*, no. 25(20), pp. 2675-2681, 2000.

- [35] M. M. Panjabi, E. K. Shin, N. C. Chen and J. L. Wang, "Internal morphology of human cervical pedicles," *Spine*, no. 25(10), pp. 1197-1205, 2000.
- [36] C. Barrey, F. Cotton, J. Jund, P. Mertens and G. Perrin, "Transpedicular screwing of the seventh cervical vertebra: anatomical considerations and surgical technique," *Surgical and Radiologic Anatomy*, no. 25(5-6), pp. 354-360, 2003.
- [37] R. K. Pandey and S. S. Panda, "Drilling of bone: A comprehensive review," *Journal of clinical orthopaedics and trauma*, no. 4(1), pp. 15-30, 2013.
- [38] A. C. Palmisano, B. L. Tai, B. Belmont, T. A. Irwin, A. Shih and J. R. Holmes, "Comparison of cortical bone drilling induced heat production among common drilling tools," *Journal of orthopaedic trauma*, no. 29(5), pp. e188-e193, 2015.
- [39] H. Heydari, N. Cheraghi Kazerooni, M. Zolfaghari, M. Ghoreishi and V. Tahmasbi, "Analytical and experimental study of effective parameters on process temperature during cortical bone drilling," *Proceedings of the Institution of Mechanical Engineers, Part H: Journal of Engineering in Medicine*, no. 232(9), pp. 871-883, 2018.
- [40] Z. Katic, T. Jukic and D. Stubljär, "Effects of osteotomy lengths on the temperature rise of the crestal bone during implant site preparation," *Implant dentistry*, no. 27(2), pp. 213-220, 2018.
- [41] V. Tahmasbi, M. Ghoreishi and M. Zolfaghari, "Investigation, sensitivity analysis, and multi-objective optimization of effective parameters on temperature and force in robotic drilling cortical bone," *Proceedings of the Institution of Mechanical Engineers, Part H: Journal of Engineering in Medicine*, no. 231(11), pp. 1012-1024, 2017.
- [42] S. Manoogian, A. K. Lee and J. C. Widmaier, "The effect of insertion technique on temperatures for standard and self-drilling external fixation pins," *Journal of orthopaedic trauma*, no. 31(8), pp. e247-e251, 2017.
- [43] Y. C. Chen, Y. K. Tu, J. Y. Zhuang, Y. J. Tsai, C. Y. Yen and C. K. Hsiao, "Evaluation of the parameters affecting bone temperature during drilling using a three-dimensional dynamic elastoplastic finite element model," *Medical & biological engineering & computing*, no. 55(11), pp. 1949-1957, 2017.
- [44] S. C. Möhlhenrich, M. Abouridouane, N. Heussen, A. Modabber, F. Klocke and F. Hölzle, "Influence of bone density and implant drill diameter on the resulting axial force and temperature development in implant burs and artificial bone: an in vitro study," *Oral and maxillofacial surgery*, no. 20(2), pp. 135-142, 2016.
- [45] M. T. Hillery and I. Shuaib, "Temperature effects in the drilling of human and bovine bone," *Journal of Materials Processing Technology*, no. 92, pp. 302-308, 1999.
- [46] Y. K. Tu, W. H. Lu, L. W. Chen, C. H. Chiang, Y. C. Chen and H. H. Tsai, "Thermal contact simulation of drill bit and bone during drilling," *In 2010 4th International conference on bioinformatics and biomedical engineering*, pp. 1-4, 2010.
- [47] Y. C. Chen, Y. K. Tu, Y. J. Tsai, Y. S. Tsai, C. Y. Yen, S. C. Yang and C. K. Hsiao, "Assessment of thermal necrosis risk regions for different bone qualities as a function of drilling parameters," *Computer methods and programs in biomedicine*, no. 162, pp. 253-261, 2018.
- [48] O. Al-Saeed, Y. Marwan, O. R. Kombar, A. Samir and M. Sheikh, "The feasibility of transpedicular screw fixation of the subaxial cervical spine in the Arab population: a computed tomography-based morphometric study," *Journal of Orthopaedics and Traumatology*, no. 17(3), pp. 231-238, 2016.
- [49] R. K. Pandey and S. S. Panda, "Optimization of multiple quality characteristics in bone drilling using grey relational analysis," *Journal of orthopaedics*, no. 12(1), pp. 39-45, 2015.
- [50] K. Gok, A. Gok and Y. Kisioglu, "Optimization of processing parameters of a developed new driller system for orthopedic surgery applications using Taguchi method," *The International Journal of Advanced Manufacturing Technology*, no. 76(5-8), pp. 1437-1448, 2015.

- [51] Medtronic, "OTOLOGIC DRILLS," 2020. [Online]. Available: <https://www.medtronic.com/us-en/healthcare-professionals/products/neurological/powered-surgical-instruments/midas-rex-mr7-high-speed-pneumatic-drills/related-products.html>. [Accessed 6 2020].
- [52] Marquardt U.K. Ltd., "Product catalogue," 2020. [Online]. Available: <https://www.marquardt-uk.com/en-US/portfolio/>. [Accessed 6 2020].
- [53] R. Nachabe, B. H. Hendriks, A. E. Desjardins, M. van der Voort, M. B. van der Mark and H. J. Sterenborg, "Estimation of lipid and water concentrations in scattering media with diffuse optical spectroscopy from 900 to 1600 nm," *Journal of biomedical optics*, no. 15(3), p. 037015, 2010.
- [54] L. L. De Boer, B. G. Molenkamp, T. M. Bydlon, B. H. W. Hendriks, J. Wesseling, H. J. C. M. Sterenborg and T. J. Ruers, "Fat/water ratios measured with diffuse reflectance spectroscopy to detect breast tumor boundaries," *Breast cancer research and treatment*, no. 152(3), pp. 509-518, 2015.
- [55] D. J. Evers, R. Nachabe, M. J. V. Peeters, J. A. van der Hage, H. S. Oldenburg, E. J. Rutgers, G. W. Lucassen, B. H. W. Hendriks and T. J. Ruers, "Diffuse reflectance spectroscopy: towards clinical application in breast cancer," *Breast cancer research and treatment*, no. 137(1), pp. 155-165, 2013.
- [56] D. J. Evers, B. H. W. Hendriks, G. W. Lucassen and T. J. M. Ruers, "Optical spectroscopy: current advances and future applications in cancer diagnostics and therapy," *Future oncology*, no. 8(3), pp. 307-320, 2012.
- [57] M. Duperron, K. Grygoryev, G. Nunan, C. Eason, J. Gunther, R. Burke and P. O'brien, "Diffuse reflectance spectroscopy-enhanced drill for bone boundary detection," *Biomedical Optics Express*, no. 10(2), pp. 961-977, 2019.
- [58] S. G. Brouwer de Koning, E. J. Baltussen, M. B. Karakullukcu, B. Dashtbozorg, L. A. Smit, R. Dirven, B. H. W. Hendriks, H. J. C. M. Sterenborg and T. J. Ruers, "Toward complete oral cavity cancer resection using a handheld diffuse reflectance spectroscopy probe," *Journal of biomedical optics*, no. 23(12), p. 121611, 2018.
- [59] R. Hennessy, W. Goth, M. Sharma, M. K. Markey and J. W. Tunnell, "Effect of probe geometry and optical properties on the sampling depth for diffuse reflectance spectroscopy," *Journal of biomedical optics*, vol. 19(10), p. 107002, 2014.
- [60] T. M. Bydlon, R. Nachabé, N. Ramanujam, H. J. Sterenborg and B. H. Hendriks, "Chromophore based analyses of steady-state diffuse reflectance spectroscopy: current status and perspectives for clinical adoption," *Journal of biophotonics*, no. 8(1-2), pp. 9-24, 2015.
- [61] M. R. Nouh and A. F. Eid, "Magnetic resonance imaging of the spinal marrow: Basic understanding of the normal marrow pattern and its variant," *World journal of radiology*, no. 7(12), p. 448, 2015.
- [62] E. N. Marieb and K. Hoehn, Human anatomy & physiology, Harlow: Pearson Education, 2007.
- [63] A. Swamy, G. Burström, J. W. Spliethoff, D. Babic, C. Reich, J. Groen, E. Edström, A. E. Terander, J. M. Racadio, J. Dankelman and B. H. Hendriks, "Diffuse reflectance spectroscopy, a potential optical sensing technology for the detection of cortical breaches during spinal screw placement," *Journal of biomedical optics*, no. 24(1), p. 017002, 2019.
- [64] G. Burström, A. Swamy, J. W. Spliethoff, C. Reich, D. Babic, B. H. Hendriks and E. Edström, "Diffuse reflectance spectroscopy accurately identifies the pre-cortical zone to avoid impending pedicle screw breach in spinal fixation surgery," *Biomedical Optics Express*, no. 10(11), pp. 5905-5920, 2019.
- [65] A. Swamy, J. W. Spliethoff, G. Burström, D. Babic, C. Reich, J. Groen and B. H. Hendriks, "Diffuse reflectance spectroscopy for breach detection during pedicle screw placement: a first in vivo investigation in a porcine model," *BioMedical Engineering OnLine*, , no. 19(1), pp. 1-12, 2020.
- [66] L. Ehlen, U. J. Zabarylo, F. Speichinger, A. Bogomolov, V. Belikova, O. Bibikova and C. Kamphues, "Synergy of Fluorescence and Near-Infrared Spectroscopy in Detection of Colorectal Cancer," *Journal of Surgical Research*, no. 242, pp. 349-356, 2019.
- [67] D. J. N. R. H. D. V. C. F. Evers, G. W. Lucassen, B. H. W. Hendriks, M. L. F. van Velthuisen, J. Wesseling and T. J. M. Ruers, "Optical sensing for tumor detection in the liver," *European Journal of Surgical Oncology (EJSO)*, no. 39(1), pp. 68-75, 2013.

- [68] Y. Hu, H. Jin, L. Zhang, P. Zhang and J. Zhang, "State recognition of pedicle drilling with force sensing in a robotic spinal surgical system," *IEEE/ASME Transactions On Mechatronics*, no. 19(1), pp. 357-365, 2013.
- [69] K. Pusch, T. J. Hinton and A. W. Feinberg, "Large volume syringe pump extruder for desktop 3D printers," *HardwareX*, no. 3, pp. 49-61, 2018.
- [70] B. T. Wittbrodt, A. G. L. J. Glover, G. C. Anzalone, D. Oppliger, J. L. Irwin and J. M. Pearce, "Life-cycle economic analysis of distributed manufacturing with open-source 3-D printers," *Mechatronics*, no. 23(6), pp. 713-726, 2013.
- [71] N. H. B. Ambrizal, A. Farooqi, O. I. Alsultan and N. B. Yusoff, "Design and development of CNC robotic machine integrate-able with Nd-Yag laser device," *Procedia engineering*, no. 184, pp. 145-155, 2017.
- [72] A. A. Malki, F. M. Salloom, J. Wong-Chung and A. I. Ekri, "Cannulated screw fixation of fractured capitellum: surgical technique through a limited approach.," *Injury*, no. 31(3), pp. 204-206, 2000.
- [73] R. Nachabé, B. H. Hendriks, M. van der Voort, A. E. Desjardins and H. J. Sterenborg, "Estimation of biological chromophores using diffuse optical spectroscopy: benefit of extending the UV-VIS wavelength range to include 1000 to 1600 nm," *Biomedical optics express*, no. 1(5), pp. 1432-1442, 2010.
- [74] T. J. Farrell, M. S. Patterson and B. Wilson, "A diffusion theory model of spatially resolved, steady-state diffuse reflectance for the noninvasive determination of tissue optical properties in vivo," *Medical physics*, no. 9(4), pp. 879-888, 1992.
- [75] B. H. Hendriks, A. J. Balthasar, G. W. Lucassen, M. van der Voort, M. Mueller, V. V. Pully and G. C. Langhout, "Nerve detection with optical spectroscopy for regional anesthesia procedures," *Journal of translational medicine*, no. 13(1), pp. 1-11, 2015.
- [76] Z. Qian, S. S. Victor, Y. Gu, C. A. Giller and H. Liu, "'Look-Ahead Distance" of a fiber probe used to assist neurosurgery: Phantom and Monte Carlo study," *Optics express*, no. 11(16), pp. 1844-1855, 2003.
- [77] P. Lai, X. Xu and L. V. Wang, "Dependence of optical scattering from Intralipid in gelatin-gel based tissue-mimicking phantoms on mixing temperature and time," *Journal of biomedical optics*, no. 19(3), p. 035002, 2014.
- [78] Y. Shiinoki and T. Yano, "Viscoelastic behavior of an agar—gelatin mixture gel as a function of its composition," *Food Hydrocolloids*, no. 1(2), pp. 153-161, 1986.
- [79] Sawbones® , "BLOCKS AND SHEETS," 2017. [Online]. Available: [https://www.sawbones.com/catalog/biomechanical/blocks-and-sheets.html?p=1&product\\_list\\_limit=36](https://www.sawbones.com/catalog/biomechanical/blocks-and-sheets.html?p=1&product_list_limit=36). [Accessed Jul 2020].
- [80] K. Matsumiya, Y. Momoi, E. Kobayashi, N. Sugano, K. Yonenobu, H. Inada and I. Sakuma, "Analysis of forces during robotic needle insertion to human vertebra," *International Conference on Medical Image Computing and Computer-Assisted Intervention*, pp. 271-278, 2003.
- [81] A. Sternheim, M. Daly, J. Qiu, R. Weersink, H. Chan, D. Jaffray and J. S. Wunder, "Navigated pelvic osteotomy and tumor resection: a study assessing the accuracy and reproducibility of resection planes in Sawbones and cadavers," *JBJS*, no. 97(1), pp. 40-46, 2015.
- [82] J. Clyde, V. Kosmopoulos and B. Carpenter, "A biomechanical investigation of a knotless tension band in medial malleolar fracture models in composite Sawbones®," *The Journal of Foot and Ankle Surgery*, no. 52(2), pp. 192-194, 2013.
- [83] J. T. Hausmann, "Sawbones in biomechanical settings-a review," *Osteosynthesis and Trauma Care*, no. 14(04), pp. 259-264, 2006.
- [84] B. W. Loh, C. M. Stokes, B. G. Miller and R. S. Page, "Femoroacetabular impingement osteoplasty: is any resected amount safe? A laboratory based experiment with sawbones," *The Bone & Joint Journal*, no. 97(9), pp. 1214-1219, 2015.
- [85] W. Y. Lee, C. L. Shih and S. T. Lee, "Force control and breakthrough detection of a bone-drilling system," *Ieee/Asme Transactions on mechatronics*, no. 9(1), pp. 20-29, 2004.
- [86] A. Field, "Discovering statistics using IBM SPSS statistics," sage, 2013.

- [87] S. Sibilla, M. Godfrey, S. Brewer, A. Budh-Raja and L. Genovese, "An overview of the beneficial effects of hydrolysed collagen as a nutraceutical on skin properties: Scientific background and clinical studies," *The Open Nutraceuticals Journal*, no. 8(1), 2015.
- [88] S. K. V. Sekar, I. Bargigia, A. Dalla Mora, P. Taroni, A. Ruggeri, A. Tosi and A. Farina, "Diffuse optical characterization of collagen absorption from 500 to 1700 nm," *Journal of biomedical optics*, no. 22(1), p. 015006, 2017.
- [89] R. F. Horton, "Optical design for a high-etendue imaging Fourier-transform spectrometer," *Imaging Spectrometry II*, no. 2819, pp. 300-315, 1996.
- [90] W. Li, Y. Liu and Z. Qian, "Determination of detection depth of optical probe in pedicle screw measurement device," *Biomedical engineering online*, no. 13(1), p. 148, 2014.
- [91] A. E. Desjardins, B. H. Hendriks, M. van der Voort, R. Nachabé, W. Bierhoff, G. Braun and B. Holmström, "Epidural needle with embedded optical fibers for spectroscopic differentiation of tissue: ex vivo feasibility study," *Biomedical optics express*, , no. 2(6), pp. 1452-1461, 2011.
- [92] C. W. Kim, Y. P. Lee, W. Taylor, A. Oygar and W. K. Kim, "Use of navigation-assisted fluoroscopy to decrease radiation exposure during minimally invasive spine surgery," *The Spine Journal*, no. 8(4), pp. 584-590, 2008.
- [93] X. Zha, "Image processing of optical coherence tomography for image guided dental drilling," Doctoral dissertation, Master's Thesis, Delft University of Technology, Biomechanical Engineering, 2011.
- [94] J. Iwanaga, P. J. Choi, M. Vetter, M. Patel, S. Kikuta, R. J. Oskouian and R. S. Tubbs, "Anatomical study of the lingual nerve and inferior alveolar nerve in the pterygomandibular space: complications of the inferior alveolar nerve block," *Cureus*, p. 10(8), 2018.
- [95] B. H. Hendriks, A. J. Balthasar, G. W. Lucassen, M. van der Voort, M. Mueller, V. V. Pully and G. C. Langhout, "Nerve detection with optical spectroscopy for regional anesthesia procedures. Journal of translational medicine," no. 13(1), pp. 1-11, 2015.
- [96] A. P. G. Schmidt, A. C. Rossi, A. R. Freire, F. C. Groppo and F. B. Prado, "Association between facial type and mandibular canal morphology-analysis in digital panoramic radiographs," *Brazilian dental journal*, no. 27(5), pp. 609-612, 2016.
- [97] D. I. Rubin, "Epidemiology and risk factors for spine pain," *Neurologic clinics*, no. 25(2), pp. 353-371, 2007.
- [98] R. Buchbinder, M. van Tulder, B. Öberg, L. M. Costa, A. Woolf, M. Schoene and C. G. Maher, "Low back pain: a call for action," *The Lancet*, no. 391(10137),,, pp. 2384-2388, 2018.
- [99] R. Bhatnagar, D. Y. Warren, P. F. Bergin, L. E. Matteini and J. R. O'Brien, "The anatomic suitability of the C2 vertebra for intralaminar and pedicular fixation: a computed tomography study," *The Spine Journal*, no. 10(10), pp. 896-899, 2010.

# 7. Appendix

## 7.1.1. Visited surgery notes

These notes have been edited to contain only non-confidential and non-privacy sensitive information.

### Prof. dr. van der Elst, 17-01-2020, clavicle fracture, Reinier de Graaf Hospital

Screw #	Drilling time (s)	Length (mm)	Speed (mm/s)	Speed (mm/min)	
1	31,2	14	0,4	26,9	
2	12,2	12	1,0	59,0	
3	11,9	14	1,2	70,6	
4	14,3	14	1,0	58,7	
5	5,1	12	2,4	141,2	
6	12,3	12	1,0	58,5	
7	10,3	14	1,4	81,6	
8	10,6	14	1,3	79,2	
9	3,4	16	4,7	282,4	
10	11	14	1,3	76,4	
11	12,9	14	1,1	65,1	
Average of 2-11				1,5	90,9
Screw diameter: 3,5mm					
Drill diameter: 2,7mm					

Top priorities for bone drilling in screw placement:

1. Keeping the drill in the right location. The anatomical dimensions cause navigational issues and the axial drilling force needs to be adapted to varying bone densities. A sudden tissue change, such as the edge of cortical bone, can cause a drill to 'shoot out' of the bone.
2. Temperature, causing thermal osteonecrosis.
3. Osteoporosis changes the bone density leading to difficulties in predicting the axial drilling forces.

"I would like to keep the drilling forces to a minimum to prevent heat development and thermal bone damage. The drill should do all the work."

"Due to a lack of feedback, you have to drill very carefully."

### Dr. Rutges, 11-03-2020, consult, Erasmus MC Hospital

	<b>time</b>	<b>depth</b>	<b>Speeds up to</b>
best case	10s	40-50mm	5mm/s
worst case	5-10min		0,1mm/s

Top challenges in SSP drilling:

1. Small pedicles



2. The extent to which the spine is rotated (this causes navigational issues)
3. The depth of the wound when using S1 screws causes difficulties to aim for the middle of the pedicle, especially with obese patients

“Apart from pushing on a handheld probe, we try to feel with it where the cancellous (‘soft’) bone is, to find the right drilling direction. The harder the bone, the harder we have to press and the receive less feedback on where we need to go. An advantage is however, that the cortical bone in young patients with relatively hard bone.

In soft bone you hardly press, because otherwise, you won’t receive any feedback on the drilling direction, yet you have a higher risk to pierce the cortical bone.”

“Could a tissue identifying drill tell me whether the bone I am drilling in is affected by osteoporosis? In that case, I could adjust the forces I exert on the drill”

“Could a tissue identifying drill tell me whether I should go left or right?”

### **Drs. Stadhouder, 06-02-2019, scoliosis surgery, Amsterdam UMC Hospital**

Placement of 22 3,5mm spinal screws

Cannulations were checked through up to four fluoroscopy shots (including shots that gave an insufficient view on the cannulation, after which another shot had to be taken).

The nerve function was checked after every screw placement using intraoperative neural monitoring (IONM) technique.

No drilling was involved; the surgeon used the so called free-hand technique, making pre-holes for the spinal screws with a handheld probe.

The surgeons expressed frustration about uncomfortable protective equipment, such as lead aprons and thyroid shields, that is regarded heavy and limits their freedom of movement

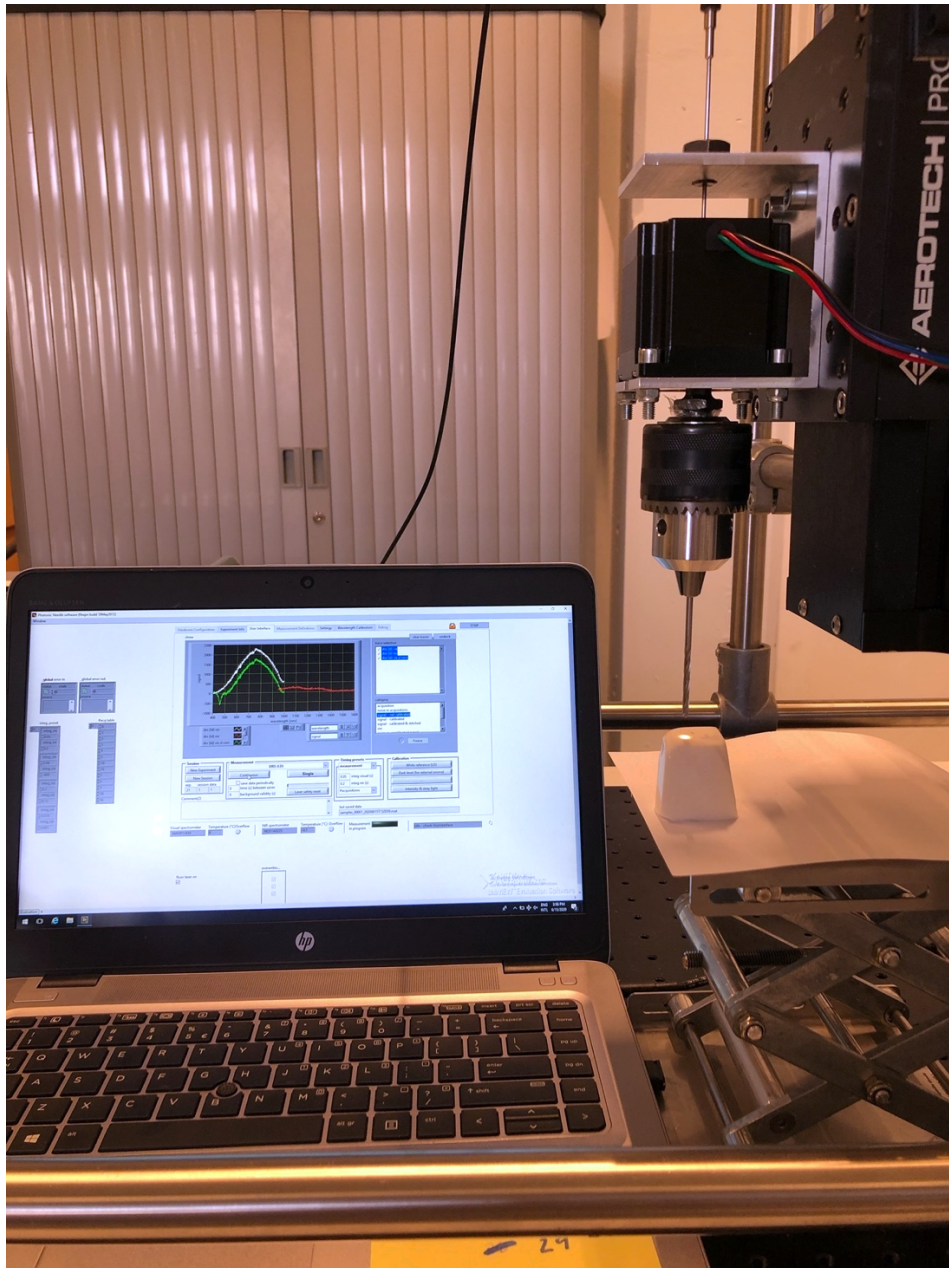
### **Prof. dr. Verhaar, 23-07-2020, consult, Erasmus MC Hospital**

On challenges in bone drilling navigation:

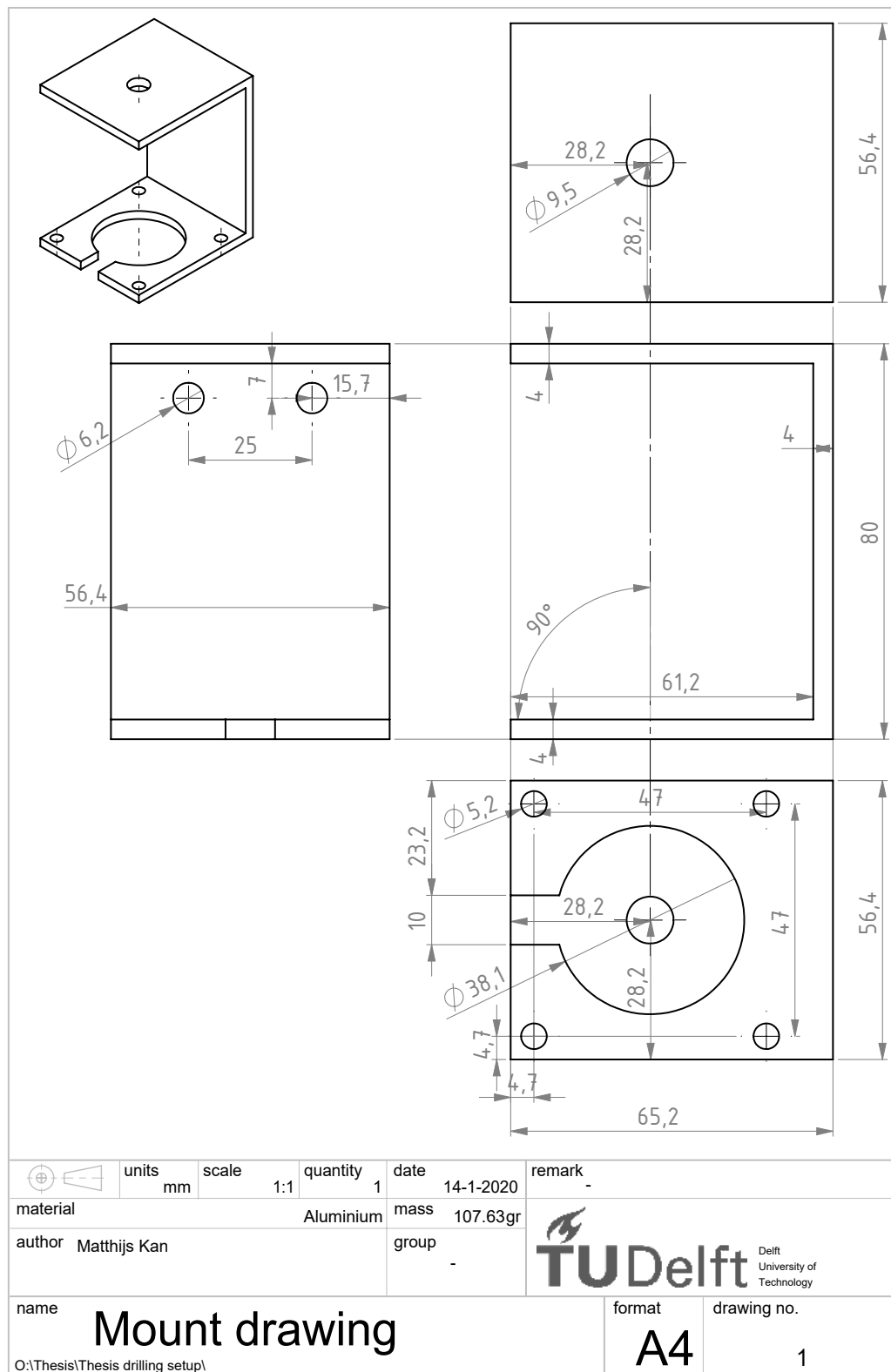
The weight of the drill is possibly the largest source of drilling inaccuracy. The difficulty with drilling, is shooting through the bone. This can cause damage behind the bone. Because the bone is hard, one has to put force on the drill towards the edge, and then suddenly the resistant force disappears at the edge of the bone.

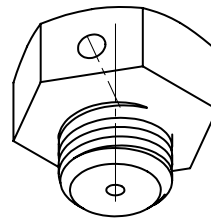
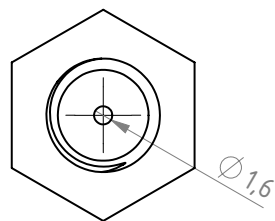
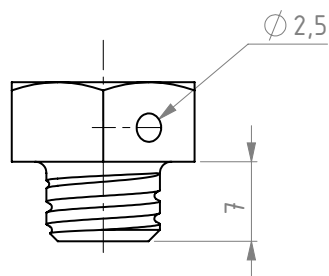
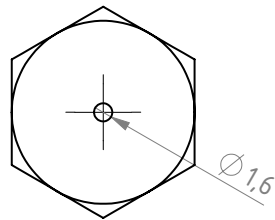
A good orthopaedical surgeon listens to the drilling sound as well. One can hear it when the drill reaches the edge of the bone.



## 7.2.1. Optical drilling setup



## 7.2.2.1. Technical drawings mount components





	units mm	scale 2:1	quantity 1	date 3-7-2020	remark -	
material				mass gr	 <b>TU Delft</b> Delft University of Technology	
author Matthijs Kan				group -		
name <b>Bolt M10</b>					format <b>A4</b>	drawing no. -
O:\Thesis\Thesis drilling setup\Drawings\						

SOLIDWORKS Educational Product. For Instructional Use Only.

## 7.2.2.2. Stepper motor specifications, torque curve and Arduino® script

### Description

Makeblock 57BYG Stepper Motor has higher torque and faster response speed than 42 stepper motor. With Makeblock 57BYG Stepper Motor Bracket, they may be easy to connect to Makeblock structural components.

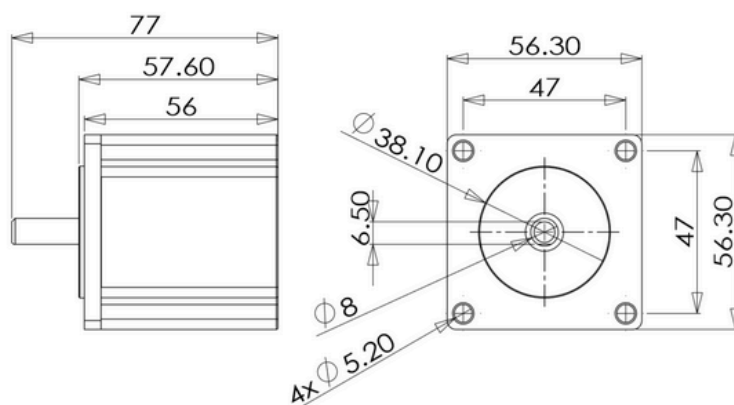
### Features

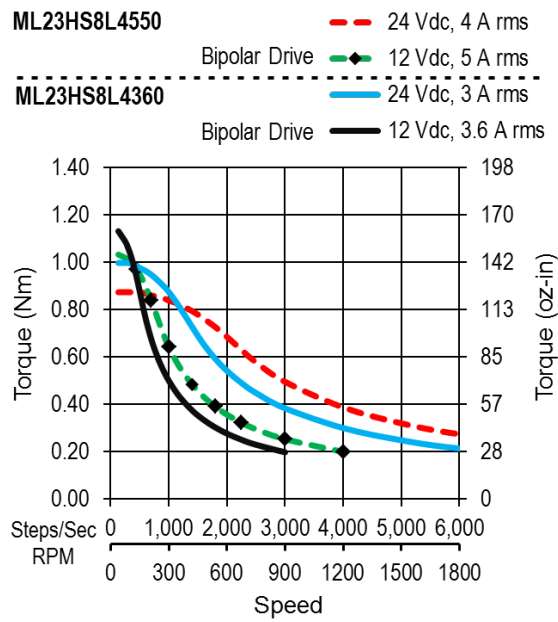
- high output torque
- low noise
- low power consumption

### Specification

- Weight: 700 g
- Motor length: 56mm
- Output shaft length: 8mm D shaft
- Pin count: 4
- Step Angle (degrees) :1.8°
- Holding Torque : 1.2N.m
- Phase current : 2.8A

### Size Charts(mm)





#### DrillingScript

```
#include <SoftwareSerial.h>
#include <Wire.h>
#include <AccelStepper.h>
unsigned long seconds = 1000;
|
// Stepper library and pins used on Arduino
AccelStepper stepper(AccelStepper::DRIVER, 13, 12); //pins: 13-PUL, 12-DIR

void setup()
{
  stepper.setMaxSpeed(1667); //The rotational speed in pulse per second
  stepper.setAcceleration(1667); //The acceleration towards MaxSpeed in pulse increase per second
  stepper.moveTo(45000); //The final position the drill rotates to in cumulative amount of pulses
}

void loop()
{
  stepper.run();
}
```

## 7.2.2.3. Aerotech PRO115SL and FUTEK load cell specifications and dimensions

PRO115SL/SLE Specifications											
PRO115SL/SLE											
Travel			50	100	150	200	250	300	400	500	600
Accuracy(1)	SL	Standard	±6 µm	±6 µm	±8 µm	±8 µm	±9 µm	±10 µm	±12 µm	±14 µm	±16 µm
		Calibrated	±1 µm	±1.25 µm	±1.5 µm	±1.75 µm	±2 µm	±2.5 µm	±3 µm	±3.5 µm	±4 µm
	SLE	Standard	±3 µm	±4 µm	±6 µm	±8 µm	±9 µm	±10 µm	±12 µm	±14 µm	±15.5 µm
		Calibrated	±1 µm	±1 µm	±1 µm	±1.5 µm	±1.5 µm	±1.5 µm	±1.5 µm	±2 µm	±2 µm
Resolution (Min. Incremental Motion)		SL	0.1 µm <sup>(2)</sup> ; 1.0 µm <sup>(3)</sup>								
		SLE	0.05 µm (-E1 Encoder); 0.2 µm (-E2 Encoder); 1.0 µm (-E4 Encoder)								
Bidirectional Repeatability <sup>(1)</sup>		SL	±1 µm	±1 µm	±1 µm	±1 µm	±1 µm	±1 µm	±1 µm	±1 µm	±1 µm
		SLE	±0.5 µm	±0.5 µm	±0.5 µm	±0.5 µm	±0.5 µm	±0.5 µm	±0.5 µm	±0.75 µm	±0.75 µm
Horizontal Straightness <sup>(1)</sup>			±1.5 µm	±2.5 µm	±3 µm	±4 µm	±5 µm	±6 µm	±8 µm	±9 µm	±10 µm
Vertical Straightness <sup>(1)</sup>			±1.5 µm	±2.5 µm	±3 µm	±4 µm	±5 µm	±6 µm	±8 µm	±9 µm	±10 µm
Pitch			19 µrad (3.9 arc sec)	29 µrad (6 arc sec)	29 µrad (6 arc sec)	39 µrad (8 arc sec)	49 µrad (10.1 arc sec)	58 µrad (12 arc sec)	78 µrad (16.1 arc sec)	97 µrad (20 arc sec)	116 µrad (23.9 arc sec)
Roll			19 µrad (3.9 arc sec)	29 µrad (6 arc sec)	29 µrad (6 arc sec)	39 µrad (8 arc sec)	49 µrad (10.1 arc sec)	58 µrad (12 arc sec)	78 µrad (16.1 arc sec)	97 µrad (20 arc sec)	116 µrad (23.9 arc sec)
Yaw			19 µrad (3.9 arc sec)	29 µrad (6 arc sec)	29 µrad (6 arc sec)	39 µrad (8 arc sec)	49 µrad (10.1 arc sec)	58 µrad (12 arc sec)	78 µrad (16.1 arc sec)	97 µrad (20 arc sec)	116 µrad (23.9 arc sec)
Maximum Speed <sup>(4)</sup>			300 mm/s								
Maximum Acceleration <sup>(4)</sup>			Function of Motor, Amplifier Selection, Payload, and Maximum Axial Load								
Load Capacity <sup>(5)</sup>		Horizontal	40 kg								
		Vertical (Axial)	18 kg								
		Side	40 kg								
Moving Mass (w/Tabletop)		SL	1.4 kg								
		SLE	1.6 kg								
Stage Mass (No Motor)		SL	4.0 kg	4.4 kg	4.8 kg	5.2 kg	5.6 kg	6.0 kg	6.8 kg	7.6 kg	8.4 kg
		SLE	4.5 kg	4.9 kg	5.3 kg	5.8 kg	6.2 kg	6.6 kg	7.5 kg	8.4 kg	9.3 kg
Material			Anodized Aluminum								
MTBF (Mean Time Between Failure)			20,000 Hours								

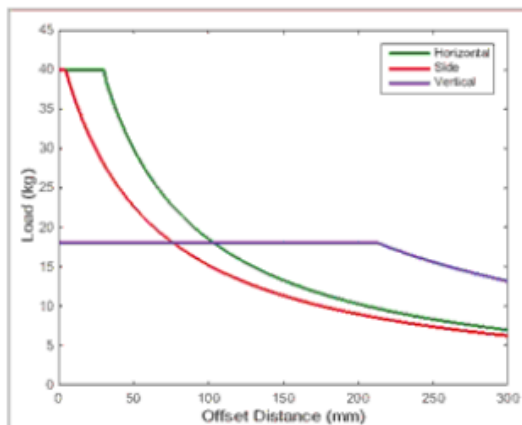
1. Certified with -PL1/PL2 options.
2. Achieved with Aerotech rotary motor with amplified sine encoder.
3. Achieved with Aerotech rotary motor with 2500 cnts/ rev digital encoder.
4. Requires the selection of an appropriate amplifier with sufficient voltage and current.
5. Axis-orientation for on-axis loading is listed.
6. Specifications are for single-axis systems measured 25 mm above the tabletop. Performance of multi-axis systems is payload and workpoint dependent. Contact factory for multi-axis applications.
7. Specifications listed are non-foldback kit options. Contact factory for specifications when a foldback kit (-FBx) is used.

## Electrical Specifications

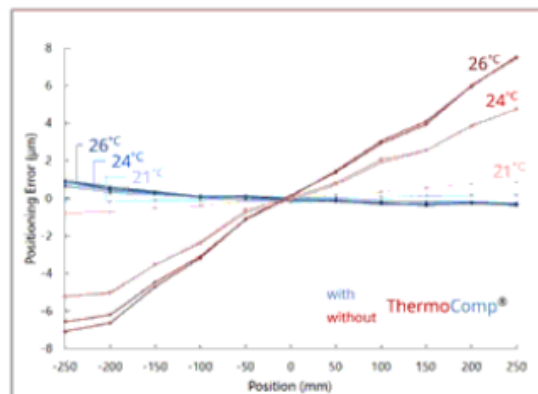
Drive System	Brushless Rotary Servomotor
Feedback (Linear Encoder – SLE Version Only)	Incremental – 1 Vpp and TTL (0.1 $\mu$ m & 0.5 $\mu$ m) Output
Feedback (Rotary Encoder)	Incremental – 1000 lines/rev (1 Vpp) and 2500 lines/rev (TTL)
Maximum Bus Voltage	340 VDC
Limit Switches	5 V, Normally-Closed

## Recommended Controller

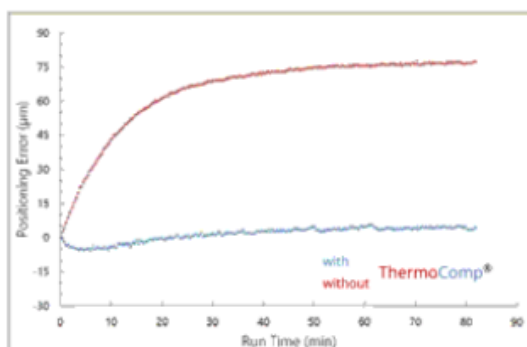
Multi-Axis	A3200	Ndrive HLe/Ndrive CP/Ndrive HPe/Npaq
	Ensemble	Ensemble HLe/Ensemble CP/Ensemble HPe
Single Axis	Soloist	Soloist CP/Soloist HPe



Cantilevered load capability of the PRO115SL/SLE.

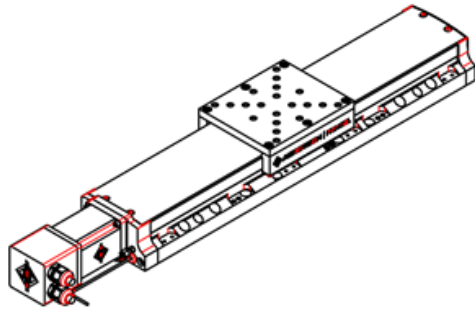


Measurement data showing successful compensation of thermal related positioning errors at several temperatures using the ThermoComp feature. Results are typical of stage performance with and without ThermoComp.

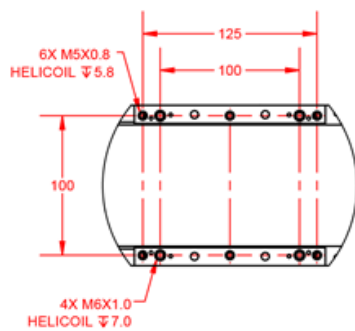
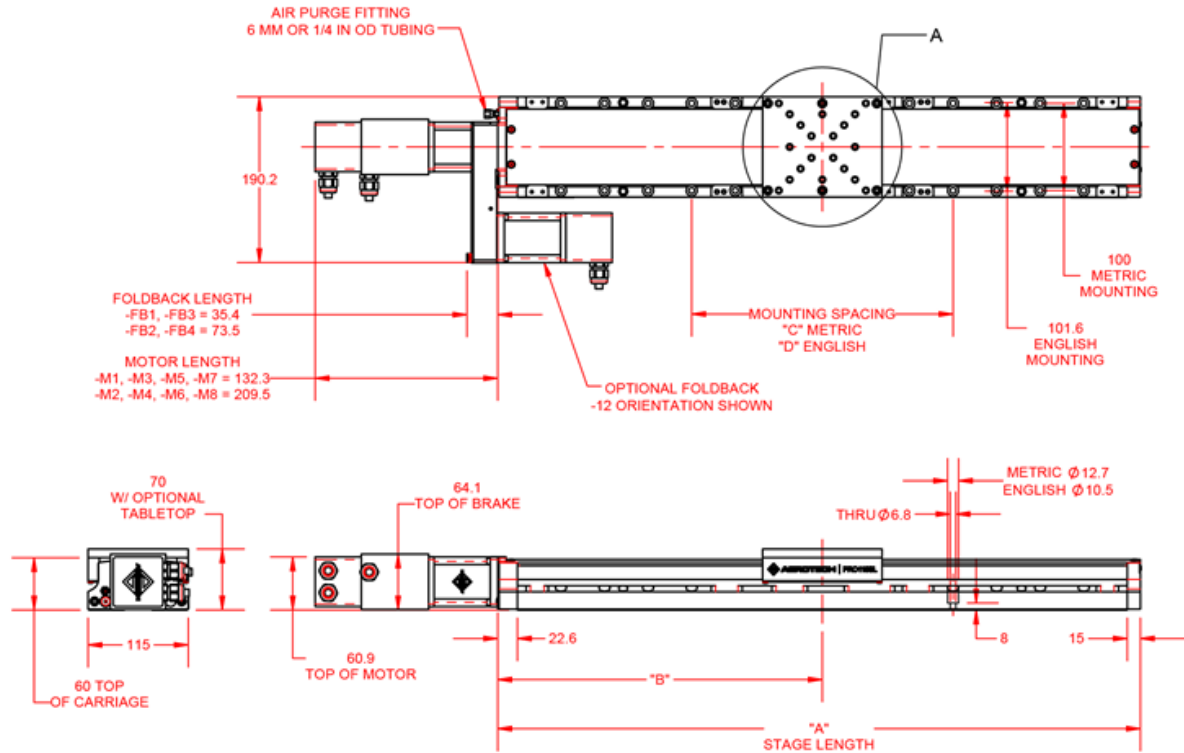
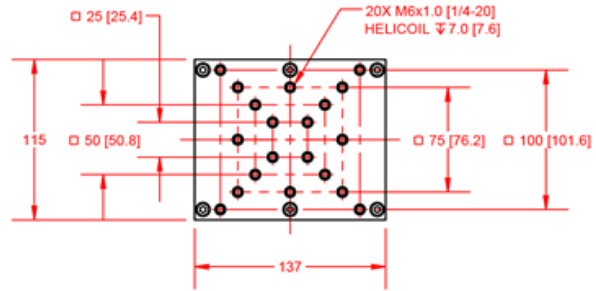


Measurement data showing successful compensation of internal heating related positioning errors during prolonged operation of a ball screw stage using the ThermoComp feature. Results are typical of ball screw stage performance with and without ThermoComp.





OPTIONAL TABLETOP  
-TT1 [-TT2]



DETAIL A  
CARRIAGE MOUNTING HOLES

BASIC MODEL	NOMINAL TRAVEL	ELEC LIMIT TRAVEL	MECH LIMIT TRAVEL	A	B	C	D
PRO115SL-050	50	58.4-63.2	75	287.6	147.6	100	101.6
PRO115SL-100	100	109.2-114	125	337.6	172.6	100, 200	101.6
PRO115SL-150	150	160-164.8	175	387.6	197.6	100, 200	101.6
PRO115SL-200	200	210.8-215.6	225	437.6	222.6	100, 200, 300	101.6
PRO115SL-250	250	261.8-266.4	275	487.6	247.6	100, 200, 300	101.6, 355.6
PRO115SL-300	300	312.4-317.2	325	537.6	272.6	100, 200, 300, 400	101.6, 355.6
PRO115SL-400	400	414-418.8	425	637.6	322.6	100, 200, 300, 400, 500	101.6, 457.2
PRO115SL-500	500	515.6-519	525	737.6	372.6	100, 200, 300, 400, 500, 600	101.6, 457.2
PRO115SL-600	600	617.2-619	625	837.6	422.6	100, 200, 300, 400, 500, 600, 700	101.6, 457.2, 660.4

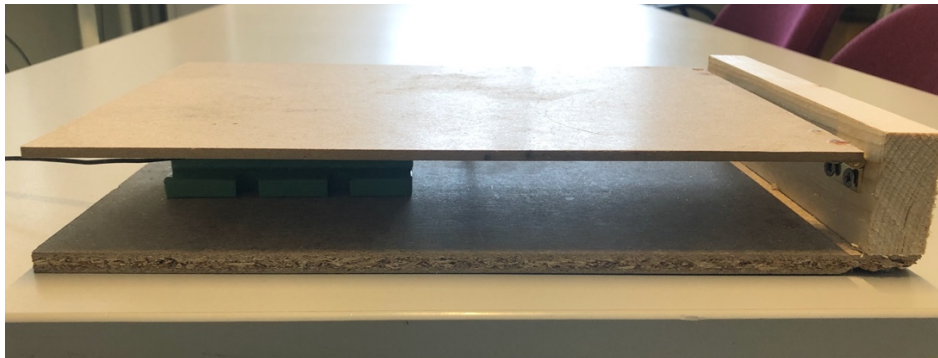
NOTES:

△ -TT1 TABLETOP OPTION REQUIRED FOR LOWER AXIS OF XY ASSEMBLIES WHEN FOLDBACK OPTION IS CHOSEN.

2. DIMENSIONS: MILLIMETERS.



## FUTEK® 25 lbs load cell setup and specifications



## FSH00096 – Capacity: 25 lbs – #4-40-Thread

LSB200 , 25 lb , JR S-Beam Load Cell , Standard , Material – 17-4 PH S.S. , #4-40-Thread , Overload Protection , 29  
Awg 4 Conductor Spiral Shielded Silicone Cable , 5 ft Long, "No Risk Life Time Warranty"

DIMENSION	VALUE
Width (in)	0.27
Height (in)	0.75
Length (in)	0.69
Weight (oz)	0.9

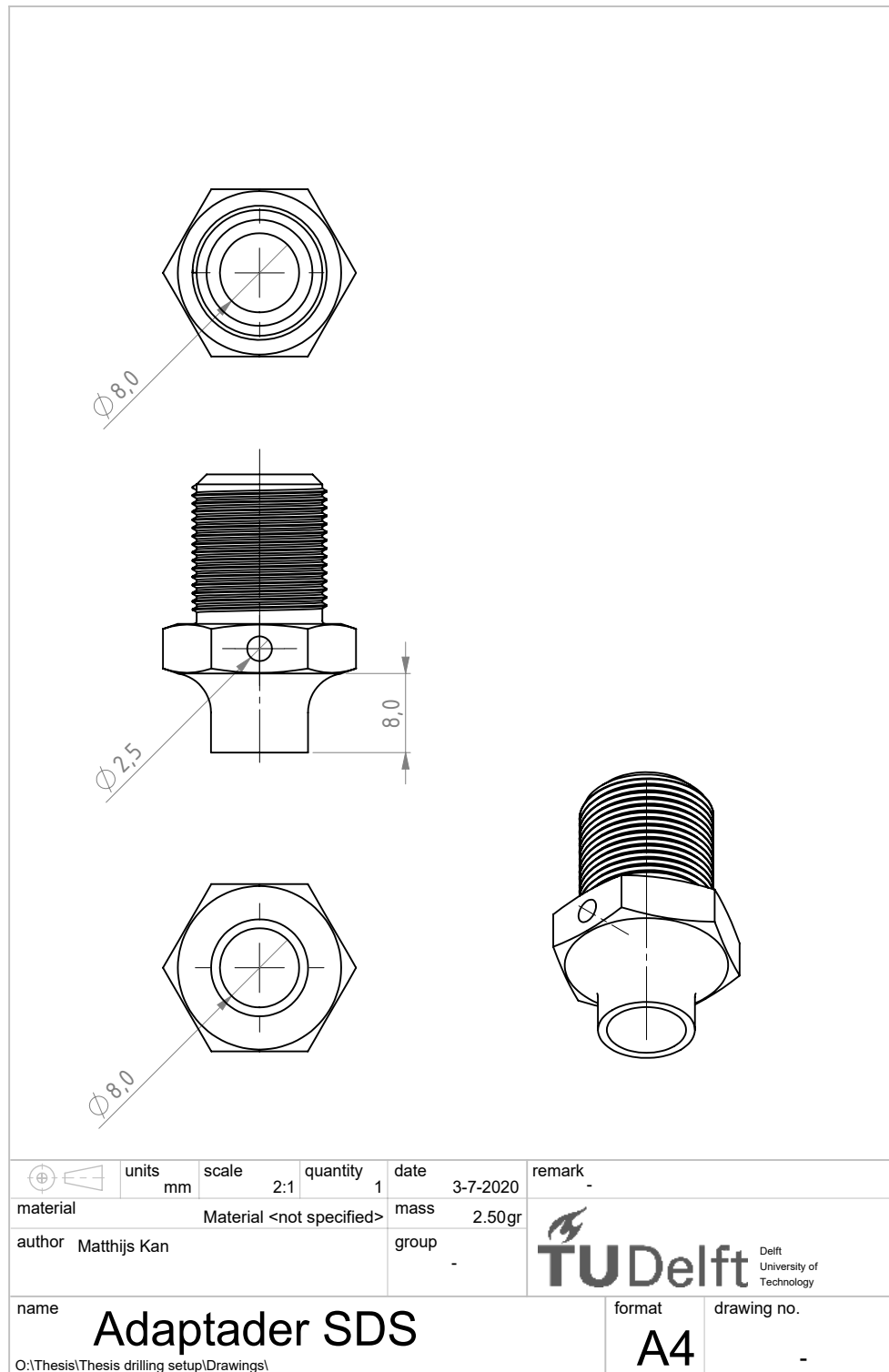
NAME	MIN	TYP	MAX	UNIT
Compensated Temperature	60		160	F
Excitation	1		10	Vdc
Hysteresis	-0.1		0.1	% of R.O.
Input Resistance		350		Ohms nom.
Insulation Resistance	500			Mohms @ 50 Vdc
Nonlinearity	-0.1		0.1	% of R.O.
Nonrepeatability	-0.05		0.05	% of R.O.
Operating Temperature	-60		160	F
Output Resistance		350		Ohms nom.
Safe Overload			1000	% of R.O.
Temperature Shift Span	-0.02		0.02	% of Load/F
Temperature Shift Zero	-0.01		0.01	% of R.O./F
Zero Balance	-3		3	% of R.O.
Capacity			25	lbs
Rated Output		2		mV/V nom.
Calibration Excitation		5		Vdc
Shunt Calibration		60.4		kOhm

This product is available with a different cable length

Model	Lenght
FSH02424	10 ft

## 7.2.2.4. Drilling parts

Technical drawing custom (SDS-)adapter

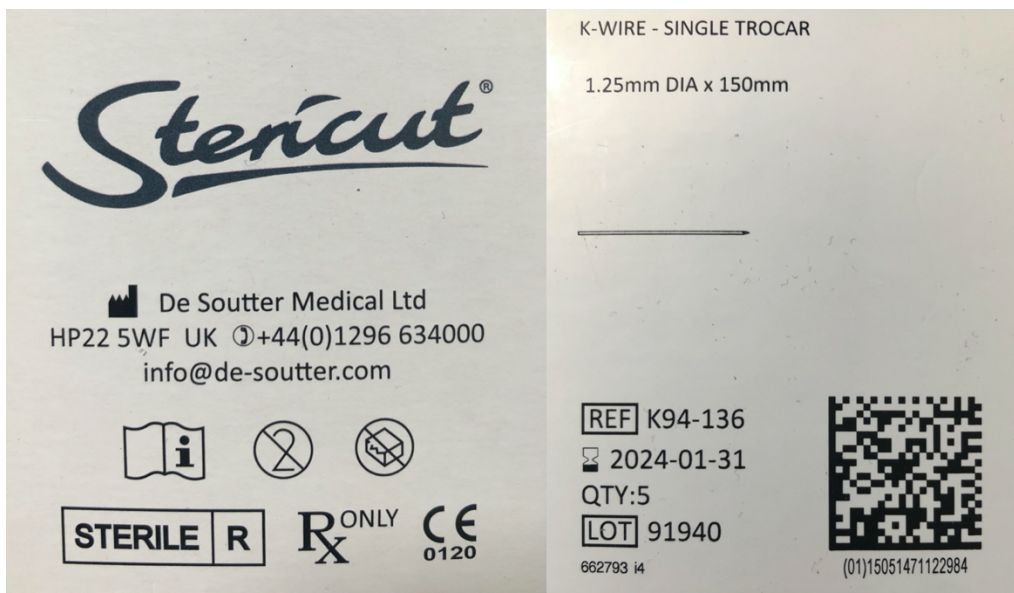


SOLIDWORKS Educational Product. For Instructional Use Only.

## Cannulated orthopaedic drills



## K-wire labels





## 7.2.3. Bone phantom tissue

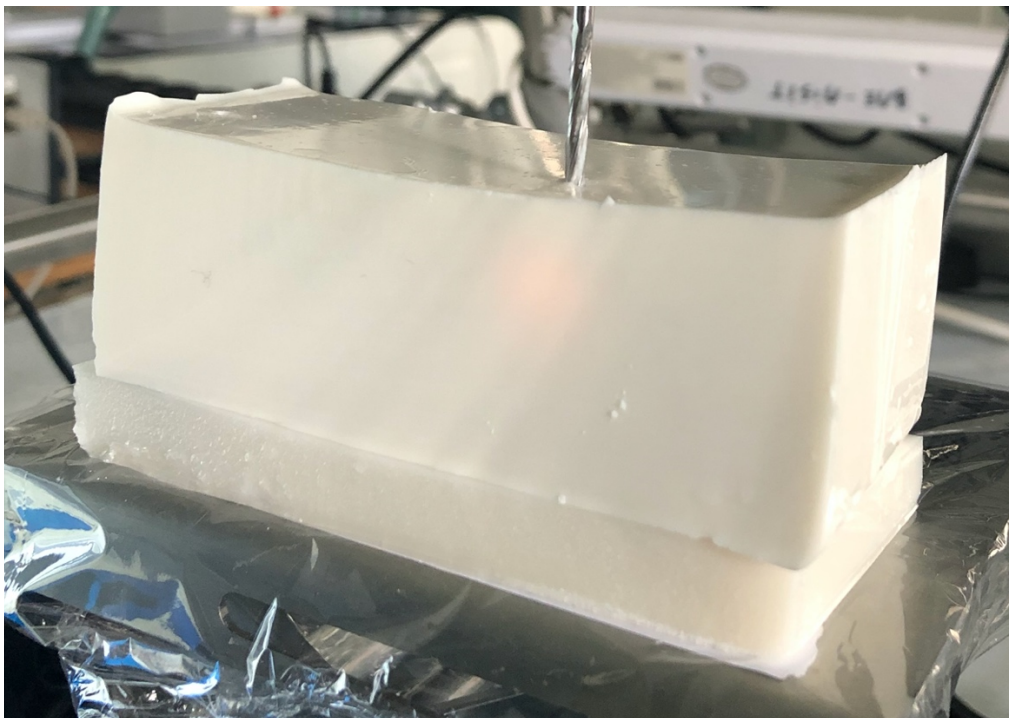
Gelatin label

Voedingswaarde per 100 gram	
Energie	1424 kJ / 340 kcal
Vetten	0 g
waarvan verzadigde vetzuren	0 g
Koolhydraten	0 g
waarvan suikers	0 g
Eiwitten	85 g
Zout	0 g
Vezels	0 g
Netto gewicht: 600 gram	
Artikelcode: HL0605	
<b>Batch: 136087</b>	
Tenminste houdbaar tot: 4-12-2021	
Opslag: koel, droog en donker	
Gebruik: Afhankelijk van toepassing:	

Intralipid label

Intralipid 20%		250 ml
emulsie voor infusie		
1000 ml bevat: gezuiverde soja-olie 200 g		
Energiegehalte per 1000 ml: 8,4 MJ (2000 kcal)		
overige bestanddelen: gezuiverde eifosfolipiden, glycerol, natriumhydroxide, water voor injectie tot 1000 ml.		
Voor gebruik de bijsluiter lezen.		
Uitsluitend voor éénmalig gebruik.		
Restanten van de emulsie dienen te worden weggegooid.		
Voor intraveneuze toediening.		
Buiten het zicht en bereik van kinderen houden.		
Bewaren beneden 25°C.		
Niet in de vriezer bewaren.		
Fresenius Kabi		
Nederland BV		
Amersfoortseweg 10E		
3705 GJ Zeist		
RVG 02608		
UR		

Optical bone phantom



Cheese label

**GOUDA HOLLAND - Kaas 48+, jong**

**Ingrediënten:** gepasteuriseerde MELK, zout, zuursel (MELK), stremsel, conserveermiddel: E251, kleurstof: carotenen. *E = door EU goedgekeurde hulpstof.* Verpakt onder beschermende atmosfeer.

**Allergenen:** melk.

**Gemiddelde voedingswaarde per 100 g:** energie kJ 1582 / kcal 381, vetten 31,0 g, waarvan verzadigde vetzuren 22,0 g, koolhydraten 0,0 g, waarvan suikers 0,0 g, vezels 0,0 g, eiwitten 24,0 g, zout 1,70 g.

**Bewaaraadvies:** gekoeld bewaren (max. 7°C). Na openen beperkt houdbaar.

**Consumentenservice**  
Jumbo Supermarkten B.V.  
Antwoordnummer 10072  
5460 VB Veghel, Nederland  
Jumbo.com

**545g e**

Deze kaas is gemaakt van weidemelk afkomstig van koeien die ten minste 120 dagen per jaar, minimaal 6 uur per dag in de Nederlandse wei lopen.

**Ten minste houdbaar tot en met:**  
**15-10-20**  
163 18:20

**VERPAKKING**  
86131000  
1  
BIJ PLASTIC AFVAL

718452 299157

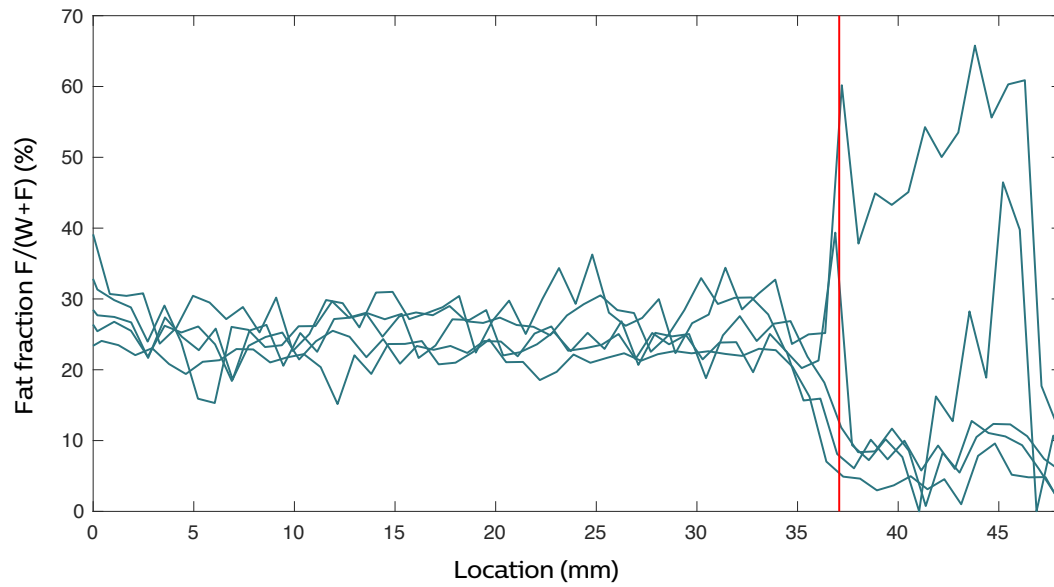
NL  
Z-0699  
EG

Sawbones® bone phantom tissue

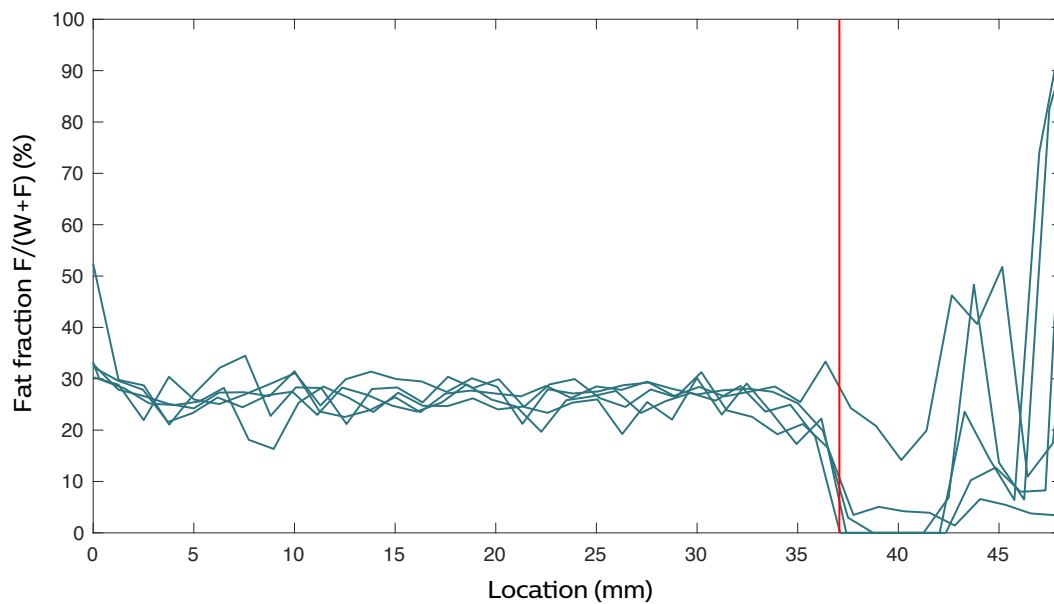


## 7.3.1. Optical measurement plots

Fat fraction versus location at a 1mm/s feed rate

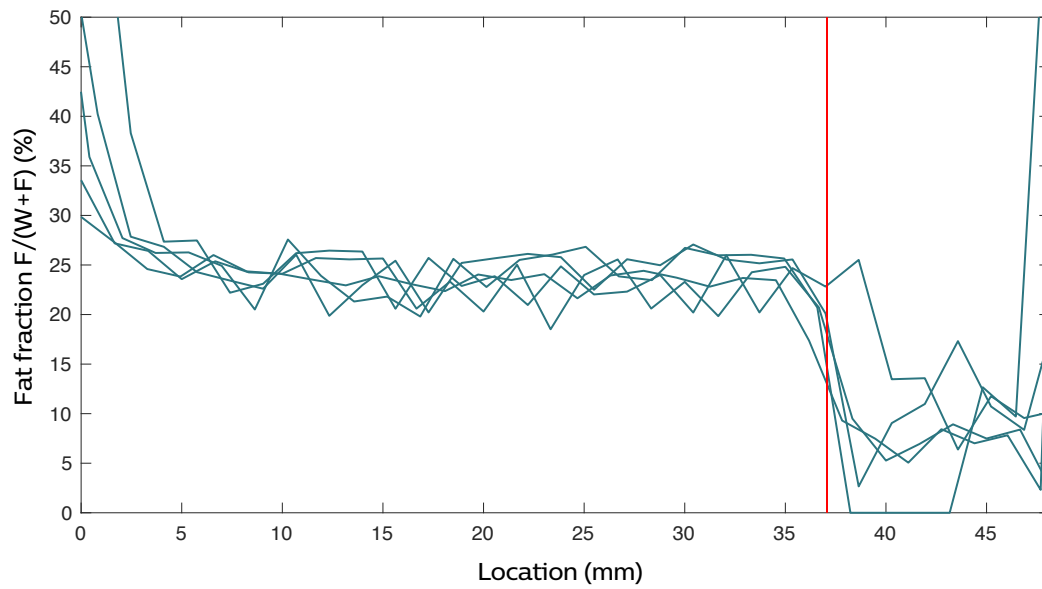


Fat fraction versus location at a 1,5mm/s feed rate

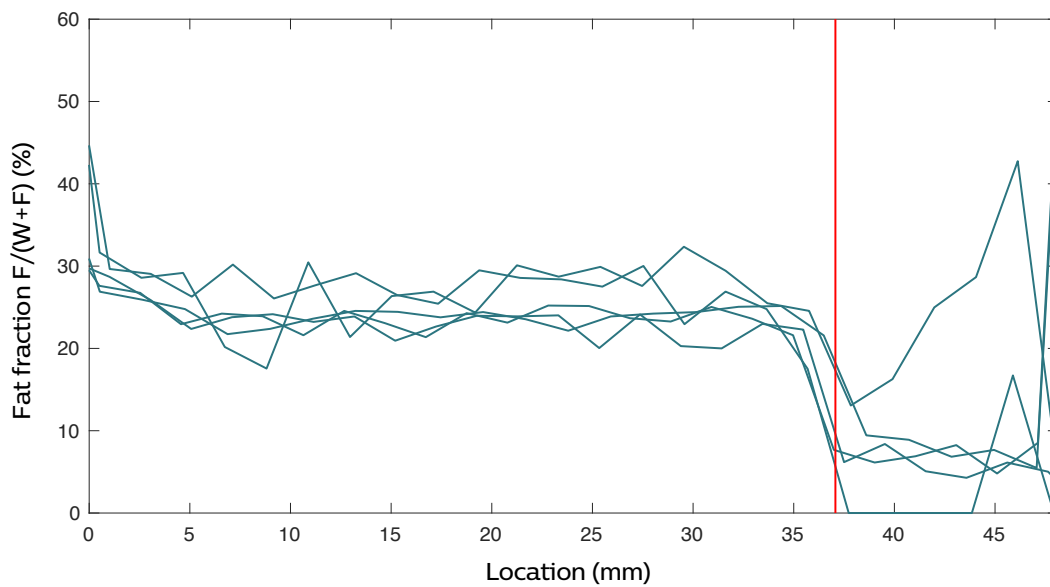




Fat fraction versus location at a 2mm/s feed rate



Fat fraction versus location at a 2,5mm/s feed rate



## 7.3.2. Mechanical measurement cheese

Force diagram of regular orthopaedic drill in cheese at a 4mm/s feed rate

